Self Sustained Thermohaline Oscillations and Their Implications for Biogeochemical Cycles

by

Rong Zhang

B. E., Tsinghua University (1995)
M. A., Boston University (1997)

Submitted to the Department of Earth, Atmospheric and Planetary Sciences
in partial fulfillment of the requirements for the degree of

Doctor of Philosophy

at the

MASSACHUSETTS INSTITUTE OF TECHNOLOGY

September 2001

[redacted]

Signature of Author ....
Department of Earth, Atmospheric and Planetary Sciences
July 2001

Certified by.................
John Marshall
Professor of Atmospheric and Oceanic Sciences
Thesis Supervisor

Accepted by...
Ronald G. Prinn
Chairman, Department of Earth, Atmospheric, and Planetary Sciences

Self Sustained Thermohaline Oscillations and Their Implications for Biogeochemical Cycles

by

Rong Zhang

Submitted to the Department of Earth, Atmospheric and Planetary Sciences
on July 2001, in partial fulfillment of the
requirements for the degree of
Doctor of Philosophy

Abstract

An ocean general circulation model (OGCM) configured with a paleo ocean bathymetry such as late Permian shows that different modes of ocean circulation might exist in warm climate: a strong 'thermal mode' induced by cooling at high latitudes and a weak 'haline mode' induced by evaporation at subtropics. The 'haline mode', obtained with enhanced freshwater flux and reduced vertical diffusivity, is inherently unstable, flushed by thermally-driven polar convection every few thousand years.

A 3-box model of the thermohaline circulation is developed to study the basic physical mechanism of thermohaline oscillations. By including convective adjustment and a parameterization of the localized nature of convection, the box model shows that haline mode is unstable over a certain freshwater forcing/vertical diffusivity range. Self-sustained oscillatory thermohaline circulations, with periods ranging from centuries to several millennia, are supported. When the amplitude of surface freshwater flux exceeds a certain threshold the haline mode stabilizes. The relationship between oscillation periods and the freshwater flux/vertical diffusivity is also studied.

Biogeochemical modeling of the late Permian ocean shows that the strong 'thermal mode' leads to well oxygenated deep ocean, the weak 'haline mode' leads to depletion of deep ocean oxygen. Biogeochemical cycles driven by the thermohaline oscillation found in the 3-box model shows that: the quasi-steady 'haline mode' is correlated with lower biological productivity, depleted deep ocean oxygen, heavier surface $\delta^{13}C$ due to weak vertical mixing, the transient 'thermal mode' is correlated with higher biological productivity, oxygenated deep ocean and lighter surface $\delta^{13}C$ due to strong vertical mixing. Those correlations are consistent with rhythmic paleo records. The $\delta^{13}C$ shift during mode switch is proportional to mean ocean nutrient level.

Thesis Supervisor: John Marshall
Title: Professor of Atmospheric and Oceanic Sciences

Acknowledgments

There are many people that I would like to thank for the completion of this thesis. First, I wish to thank my thesis advisor, John Marshall for introducing me into this new interdisciplinary field a few years ago. His enthusiasms in this research topic encouraged me to go through variant difficulties. Through numerous discussions, he continuously advised me with inspiring ideas. I also would like to thank my thesis committee members for their frequent support and carefully reading of my thesis. Mick Follows spend lots of time to discuss with me and help me develop the biogeochemical models. Alan Plumb gave me very good suggestions and help me develop the zonally averaged atmospheric model, though it is not include in this thesis. Dan schrag introduced to me many literatures on the study of paleoclimates, and always asked many critical questions which lead to the directions of future work. I would like to give special thanks to John Edmond, he is always fascinated with this research, he gave me many help and suggestions which I will never forget about.

I am grateful to Ed Boyle for chairing my thesis defense and giving valuable comments on this thesis. I would like to thank all the faculty for the excellent education experience I have in the Program of Atmospheric and Planetary Sciences for the last four years. I am sincere grateful to Joe Pedlosky for giving me very good suggestions, and Jochem Marotzke, Kerry Emanuel for helpful discussions related to this research. I thank Prof. Rowley for providing us his topographic reconstructions of the late Permian. Also I wish to thank Paola Cessi and Alistair for helpful discussion on numerical integration schemes.

I sincerely thank Chris and Alistair for the help on general circulation models, and Parv for the help on developing the carbon isotope model. I enjoy many interesting discussions with the postdocs and students of the program in the last several years, particularly, I wish to give thanks to Samar Khatiwala, Daniel Jamous, Jeff Scott, Kerim Nisancioglu, Taka Ito, Jake Gebbie, Markus Jochum, Greg Lawson, and Jubao Zhang - my former officemate who gave me many help on the research.

Finally, I am very grateful to my parents for their selfless love and support, to my

sister for enlightening me so many thing in my childhood, and most of all, to my husband Wei Hu for his love and unconditional support day by day.

This thesis work was supported by NSF grant OCE-9819488 and MIT Joint Program on Science and Policy of Global Change grant #007625-001.

Contents

List of Figures

List of Tables

Chapter 1

Introduction

In past climates the thermohaline circulation (THC) of the ocean may have been quite different from that of today. For example, paleoclimatic records (Railsback et al., 1990) suggest that in warm periods of the Earth history, such as the Ordovician, warm salty waters may have ventilated the ocean in low latitudes (haline mode circulation), and so would have been very different from today's ocean in which deep water formation in high latitudes (thermal mode circulation) brings cold water to depth. Such different ocean circulations would have very different implications for climates and biogeochemical cycles. The instability of the haline mode circulation and self sustained thermohaline oscillations have been found by several ocean general circulation model (OGCM) studies using an idealized single basin configuration (Marotzke, 1989; Wright and Stocker, 1991; Weaver and Sarachik 1991a, b; Weaver et al. 1993; Winton and Sarachik 1993; Huang 1994). The physical mechanism causing such internal thermohaline oscillation is not very clear and deserves further investigations. In our study of possible modes of the late Permian ocean circulation (Zhang et al., 2001), we found that the haline mode (HM) was inherently unstable for fixed external forcing, periodically switched in to a transient strong thermal mode (TM) in which deep water formed in polar region (the so-called flushing event (Marotzke, 1989)), and gradually returns to the HM to close the cycle. Such internal thermohaline oscillations may have significant implications for understanding the paleoclimatic records, such as the centuries to millennia oscillations during glacial periods (Johnson, 1992). Such oscillations do not appear to occur in the modern ocean, because, apparently, the surface freshwater forcing is not strong enough. Mode switching is more likely to occur, perhaps, during glacial periods in which the freshwater forcing due to ice melting at polar region is much stronger, or during warm equable paleoclimates such as late Permian, or Mid-Cretaceous in which the buoyancy forcing due to the freshwater flux may have been stronger than that due to the air-sea heatflux.

1.1 Paleoclimatic records of thermohaline circulation variability and associated biogeochemical cycle

Brass et al. (1982) proposed a hypothesis that warm saline bottom water may have been formed in ancient oceans such as Cretaceous. Railsback et al. (1990) found paleontological and isotope evidence for warm saline deep waters produced in low to mid latitude in Ordovician oceans. The oxygen isotopic evidence (Figure 1-1) indicates that the water temperature increased with depth in Ordovician oceans, until it reached a maximum at intermediate level, then decreased again. This is opposite to the modern ocean in which cold fresh deep water is formed by polar sinking.

Recently it has been suggested that a long-term deep-sea anoxic event straddled the Permo-Triassic boundary 250 million years ago (Isozaki, 1997; Kajiwara et al., 1994). P/T boundary Pelagic cherts from Japan and British Columbia, Canada indicate that anoxia might have reached the bottom of the late Permian ocean, extended laterally several thousand of kilometers in both the western and eastern superocean during that period, supporting the idea that wide spread deep-sea anoxia developed around the Permian/Triassic boundary. The event has been linked to the end-Permian mass extinctions

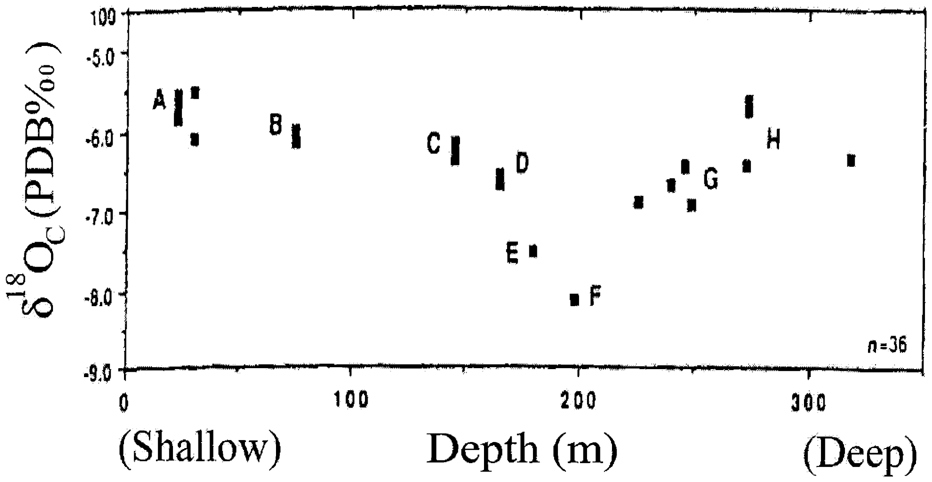

Figure 1-1: Variations in oxygen isotopic composition of shells, indicating variations in water temperature with paleodepth in Ordovician ocean (Railsback et al., 1990).

as a potential causal mechanism (Knoll et al., 1996). The deep-sea anoxic event indicates a dramatic change in ocean thermohaline circulation from that of today.

Organic-carbon-rich black sediments are often been taken as evidence for anoxic conditions in paleo oceans. Other evidence from paleo records for anoxic ocean include sediments which are fine laminated. The bioturbatioin of the sediments indicates oxygenated ocean, and the fine lamination of the black sediments indicates the absence of benthic life under anoxic conditions. Evidence for low surface primary productivity correlated with organic-carbon-rich sediments also supports anoxic conditions. There are many organic-carbon-rich black sediments in Mid-Cretaceous found from various Deep Sea Drilling Project (DSDP) sites (Arthur 1979; Arthur and Schlanger, 1979). Bralower and Thierstein (1984) claimed that the estimated Mid-Cretaceous surface primary production rates at times of those black-shale deposition are an order of magnitude lower than that in today's ocean. Wortmann et al. (1999) reported that geochemical analyses of Cretaceous sub-CCD (carbonate compensation depth) sediments from the Tethys and Atlantic oceans indicate periodic changes from a high-productivity green shale mode to a low-productivity black shale mode, suggesting changes from a well-oxygenated ocean to oxygen-deficient ocean. However, one should be careful about those results, recent research suggests that high primary production can also induce high accumulation of organic-carbon-rich sediments (Pedersen and Calvert, 1990), and the surface primary productivity at millions of years ago is hard to be estimated accurately from sediments, so the organic-carbon-rich sediments can not be taken as the sufficient evidence for anoxia.

Herbert and Fischer (1986) found that Mid-Cretaceous black shale rhythms in central Italy reflect orbital eccentricity and precessional cycles (Figure 1-2), organic-carbon-rich sediments (which might indicate anoxia) are always associated with lower concentration of biogenic components: carbonate and silica (which might indicate lower surface productivity). The high frequency cycle in deep sediments indicates a highly dynamic ocean-climate system, in which a significant mode switch occurred in the ocean circulation. Mid-Cretaceous rhythmic stratification of the Bridge Creek Limestone near Pueblo, Colorado (Arthur and Dean, 1991) shows that the organic-carbon-rich layers are associated not only with lower biogenic carbonate, but also with heavier $\delta^{13}C$ and lighter $\delta^{18}O$ in the surface ocean (Figure 1-3).

High resolution records from the Greenland ice cores (GRIP) also indicate significant climatic oscillations on millennial time scales during the last glacial period, i.e. the Dansgaard/Oeschger Event (Broecker and Denton, 1989). These events are correlated with iceberg discharges into the North Atlantic on the same time scales (Bond and Lotti, 1995, Figure 1-4), the injection of freshwater may induce the thermohaline circulation variability and thus the millennial-scale surface temperature changes in Greenland during the glacial period.

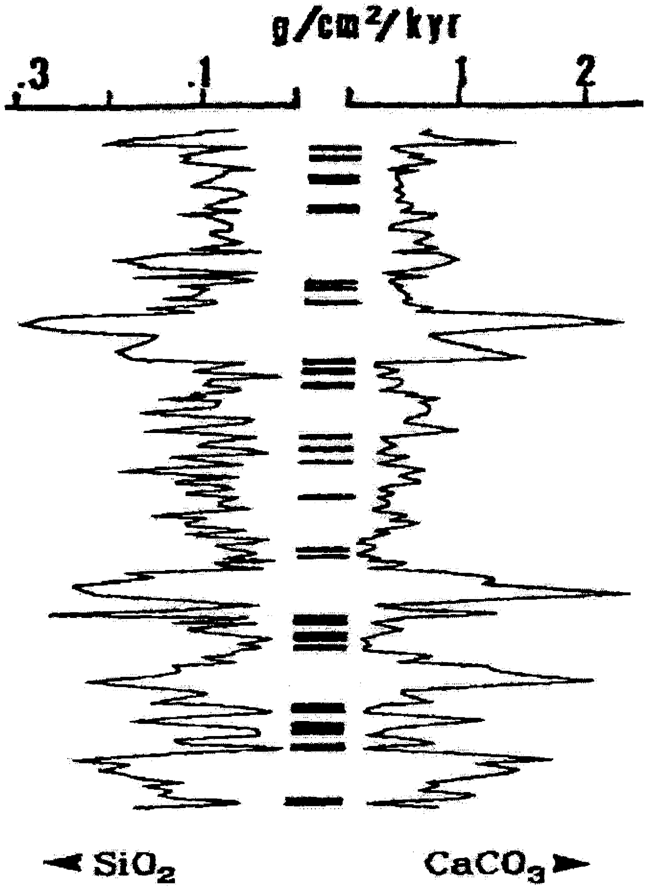

Figure 1-2: Fluxes of carbonate and biogenic silica, upper Albian of Piobbico core, in relation to occurrences of anoxic bands, shown as solid intervals (Sarmiento et al., 1988).

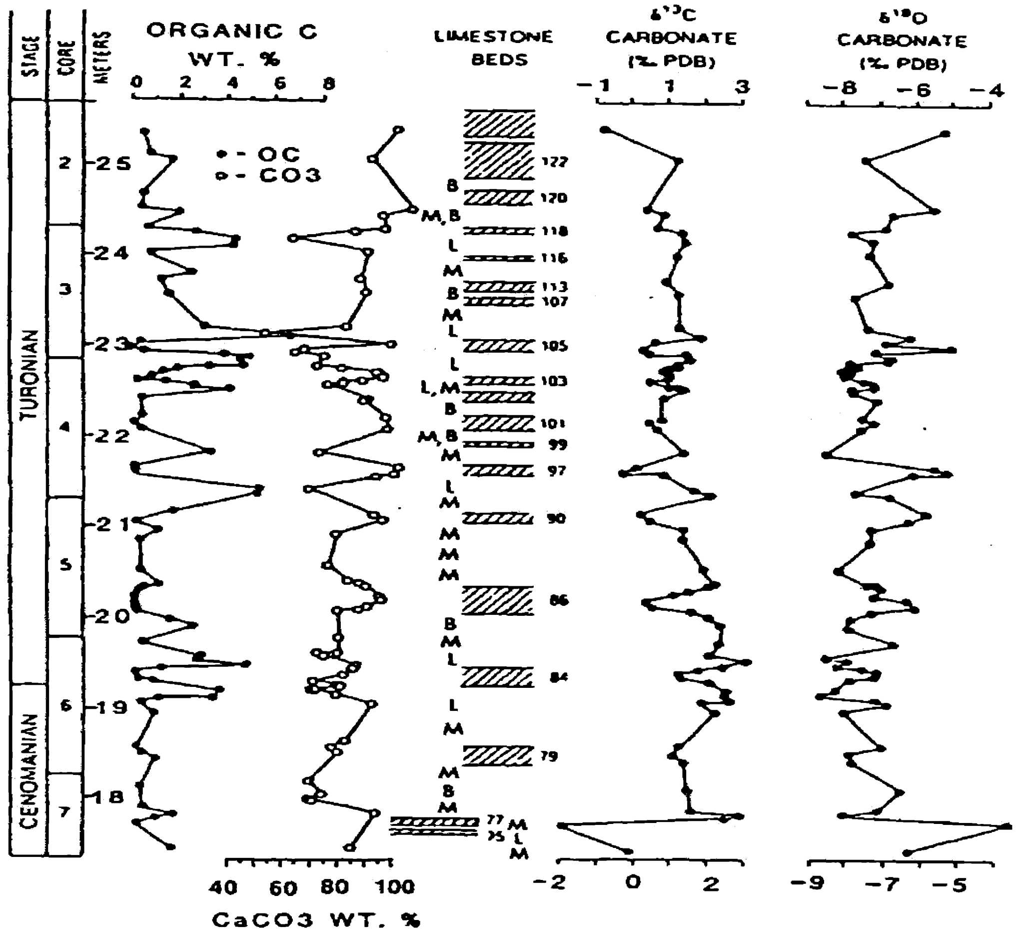

Figure 1-3: Mid-Cretaceous rhythmic stratification of the Bridge Creek Limestone near Pueblo, Colorado (Arthur and Dean, 1991).

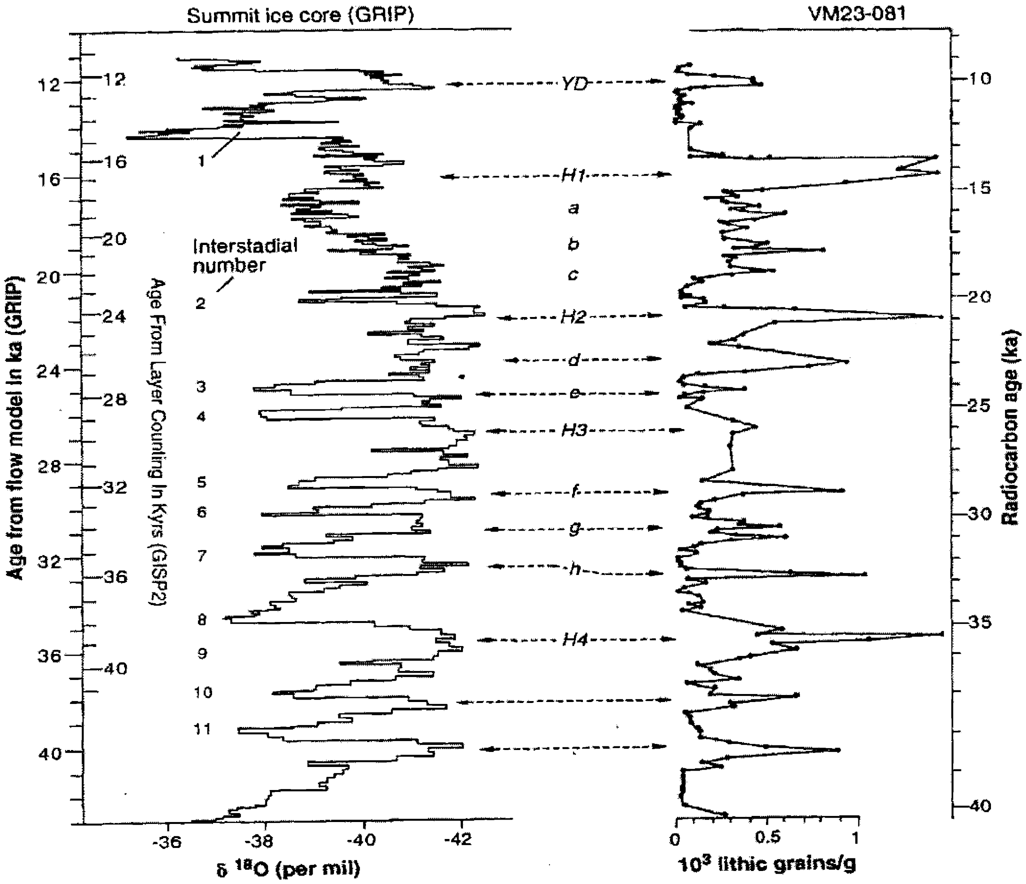

Figure 1-4: Comparison of the oxygen isotope record for the GRIP ice core - indicator of polar surface temperature, with measurements of lithic concentrations - indicator of ice-rafting events. (Bond and Lotti, 1995)

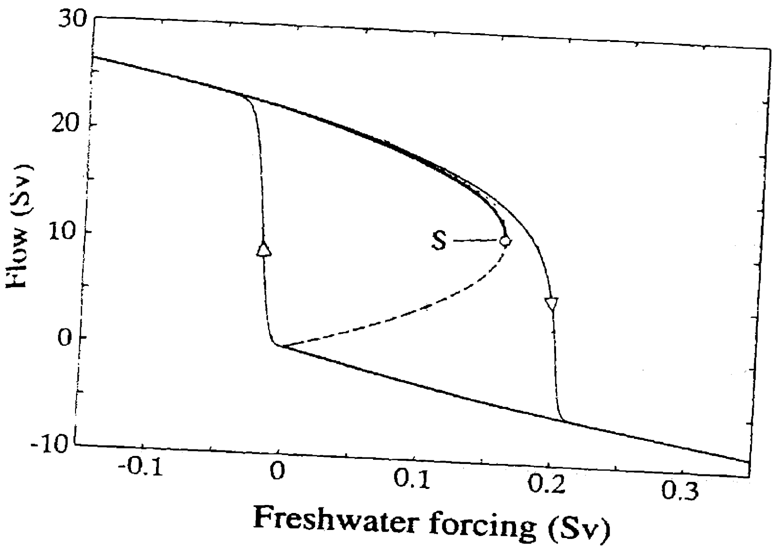

Figure 1-5: Steady state solutions of Stommol's box model, i.e. the overtuning flow as function of surface freshwater forcing. Solid line indicates stable solutions, dashed line indicates unstable solutions, S indicates the saddle-node bifurcation point (Ramstorf, 1996).

1.2 Multiple steady state solutions of the thermohaline circulation and self sustained thermohaline oscillations

The first theory to understand thermohaline variability, such as that reflected in many paleo records, is Stommel's (1961) 2-box model. Stommel (1961) showed that the THC can have multiple steady states when the freshwater forcing is strong enough: he found a strong stable TM circulation, a weak unstable TM circulation and a stable HM circulation (Figure 1-5). The internal thermohaline oscillations found in many OGCMs, however, seem inconsistent with Stommel's (1961) prediction that the HM circulation is stable. We will show that the convective adjustment process which is included in OGCMs but not in Stommel's box model is a crucial physical process at work.

Since Stommel's (1961) pioneering work, many box models have been constructed to study the multiple steady solutions of the THC (e. g. Rooth, 1982; Huang et al., 1992). Without convective adjustment, Stommel-type box models can not support self-sustained oscillations (Ruddick and Zhang 1996). Welander (1982) proposed a heat-salt oscillator using a model with convective adjustment between the surface and deep ocean whose temperature and salinity were fixed. It exhibits self-sustained oscillations only when warm salty water convects over cold fresh water. This kind of convection is likely to happen in low latitudes, but not in polar regions. Winton (1993) modified this model by fixing the surface temperature but allowing deep ocean temperature to vary. He obtained a self-sustained oscillation with polar convection when a nonlinear equation of state for seawater density was used. Pierce et al. (1995) also obtained a self-sustained oscillation by modifying Welander′s convection model to allow both surface and deep ocean temperatures and salinity to vary, again requiring nonlinear equation of state for density.

It is difficult to explore parameter space and the relationship of oscillatory period to freshwater flux forcing and vertical diffusivity by direct numerical integration of an ocean general circulation model. In this study, we construct a simple box model with convective adjustment and linear equation of state of seawater density by combining the Stommel-type box model with the Welander-type convection model. With it we are able to study the self-sustained centuries-millennial thermohaline oscillation involving polar convection as found in many OGCMs, and its relationship with those multiple steady solutions of THC found in many box models and OGCMs. Here we assume the overturning circulation is linearly proportional to the surface meridional density gradient, we allow the temperature and salinity to vary in both surface and deep ocean. We do not require a nonlinear equation of state to achieve unstable stratification, i.e. the nonlinear equation of state is not an essential requirement to obtain self-sustained thermohaline oscillation. Instead we introduce the concept of ′local convection′ in our box model to represent the convective process appearing in OGCMs. This simple box model catches the main character and essential physics of the thermohaline oscillation exhibited in OGCMs. It shows that the steady HM becomes unstable for certain freshwater forcing range and vertical diffusivity range when including convective adjustment; thus thermohaline oscillations could exist in such forcing range. It will improve our understanding of this problem, serving as an efficient tool to explore the parameter space, the relationship of oscillatory period to freshwater flux forcing and vertical diffusivity.

1.3 Interaction between thermohaline circulation and biogeochemical cycles

Different circulation modes have very different implications for the biogeochemical cycle. Understanding the interaction will help us make better interpretation of the paleo records. However, the interaction is far from clear. For example, hypotheses for deep-sea anoxia include ocean stagnation (Knoll et al., 1996), strong thermohaline ocean circulation driven by polar convection (Sarmiento et al., 1988), and low-latitude sinking of warm, saline, oxygen-depleted surface water (Railsback et al., 1990). Each of these mechanisms has different implications for late Permian ocean circulation and biogeochemistry. Figure 1-6 is a schematic diagram showing the interaction among thermohaline circulation Ψ, convective mixing, and the distribution of dissolved oxygen, $\delta^{13}C$ in the modern ocean. Within the surface euphotic zone, photosynthesis activities will produce organic matter fluxes which are then exported to the deep ocean. Below the surface euphotic zone, remineralization processes will transfer the organic matter into inorganic nutrients and meanwhile consume oxygen. Because of the biological fractionation, organic matter takes up more lighter carbon isotope, the surface water is enriched in ^{13}C, $\delta^{13}C$ of the surface ocean will always be heavier than that of the deep ocean. Ocean thermohaline circulation Ψ advects the nutrients, oxygen and carbon around, ventilates oxygen into the deep ocean from polar sinking branch and upwells the nutrients to the low latitude surface to support the photosynthetic activity. Convective mixing at high latitudes will mix higher oxygen concentration, heavier $\delta^{13}C$ at surface with lower oxygen concentra-

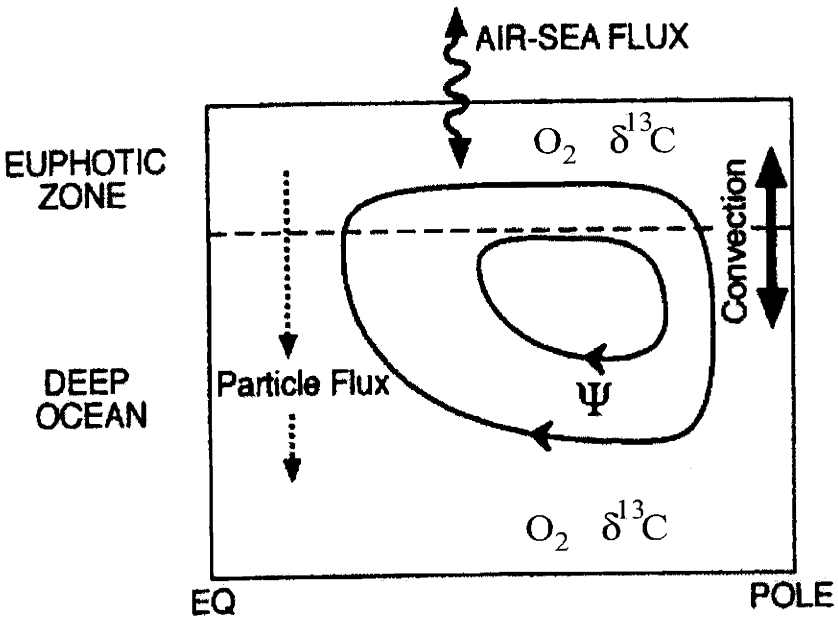

Figure 1-6: Schematic diagram of interaction between thermohaline circulation and biogeochemical cycle.

tion and lighter $\delta^{13}C$ in the deep ocean. In the surface boundary layer, air-sea flux keeps exchanging oxygen and CO_2 from the ocean to the atmosphere. Only quantitative models can be used to understand the whole system involving many competing processes. We will apply insights from box models and 3-dimensional circulation and biogeochemical models to explore conditions under which deep-sea anoxia might have developed in the late Permian ocean and the surface $\delta^{13}C$ shift caused by the mode switching.

1.4 Overview

In this thesis, we will focus on the following questions: Why is the HM circulation unstable and oscillatory in the OGCMs, but not in the Stommel-type box models? What controls the oscillation period? Which kind of ocean circulation mode would lead to deep-sea anoxia? What would be the $\delta^{13}C$ shift when the ocean circulation switches from one mode to another? To answer those questions, different kinds of numerical model are employed, from simple box models to 3-dim general circulation models. In chapter 2, we will discuss the multiple circulation modes and the property of the self-sustained thermohaline oscillation found in OGCM of the late Permian ocean. In chapter 3, we will show the results of a simple 3-box model which catches the essential physics of the self-sustained thermohaline oscillation. In chapter 4, we will discuss the biogeochemical cycle driven by the thermohaline circulation fields in the box models. In chapter 5, we will talk about the study of the biogeochemical cycle with 3-dim biogeochemical models driven by ocean circulation fields obtained from the OGCM.

Chapter 2

Self sustained thermohaline oscillations in OGCM of the late Permian ocean

2.1 Model description and surface boundary conditions

We obtained a thermohaline oscillation with a global OGCM (MITgcm, Marshall et al. 1997 a,b) configured for late Permian bathymetry. The late Permian (250 million years ago) is a period of typical warm equable climate (Taylor et al., 1992), the HM circulation is more likely to happen in such period. The late Permian land-sea distribution was quite different from that of today. The supercontinent Pangaea extended from the north pole to the south pole, the Panthalassic superocean covered nearly 70% of the Earth's surface and connected to the small, narrow Tethys sea. A paleobathymetry was obtained from D. B. Rowley and used to configure our ocean circulation model for the late Permian (Figure 2-1). Although epicontinental regions are represented by variable depths between 0 to 4000m in the reconstruction, the deep ocean is assumed to have a

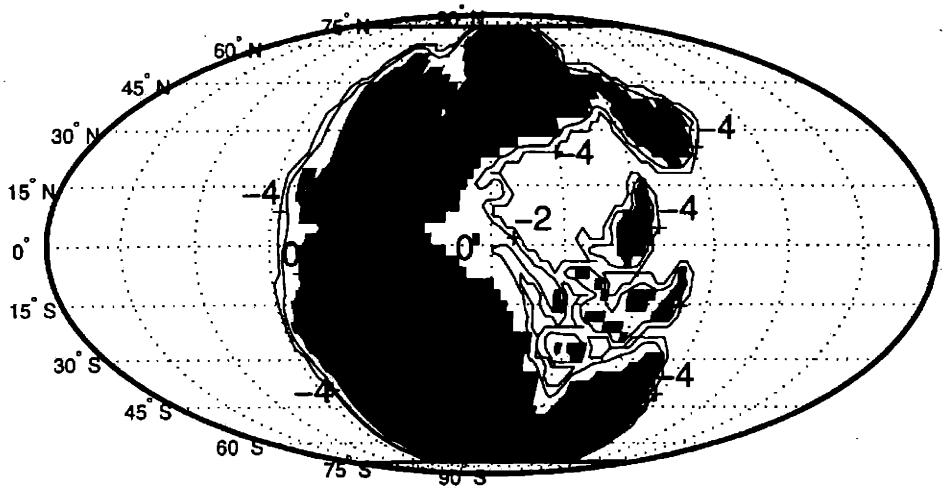

Figure 2-1: Late Permian bathymetry (ocean depth in km)

flat bottom with a uniform depth of 4000 m due to lack of other evidence. The ocean domain of the model extends from 70^oN to 70^oS. The physical model, which uses height as a vertical coordinate, is configured at a resolution of $2.8^o \times 2.8^o$ in the horizontal and 15 levels in vertical. We use 'no slip' conditions at the lateral walls and bottom and insulating thermal boundary conditions. The horizontal and vertical viscosity are $5\times10^5 m^2/s$, $10^{-3} m^2/s$ respectively, the horizontal and vertical diffusion coefficients are $10^3 m^2/s$ and $5\times10^{-5} m^2/s$ respectively in close accord with Bryan (1986). Tracers are advected with the 'transformed Eulerian mean' velocity (Gent and McWilliams, 1990) and convection is parameterized, as described in section 5 of Marshall and Schott (1999). The resulting model, when forced by observed modern-day winds and air-sea fluxes, yields a plausible representation of the coarse-grained circulation of the modern ocean, with a global overturning circulation of strength 20 Sv and a northward meridional heat transport peaking at 1.5 PW.

The prevailing meteorological conditions are even less certain and so we chose two scenarios. Scenario 1, based on an atmospheric circulation model of the late Permian

(Kutzbach et al., 1990; Kutzbach and Gallimore, 1989), corresponds to a warm climate with enhanced greenhouse effect ($5 \times CO_2$) and reduced solar luminosity (1% decrease). It gives (relative to the modern) a weak surface wind stress τ (Figure 2-2(a)), a weak pole-equator surface temperature gradient (Figure 2-2(b)) and a fresh water flux, $E - P$, which reached a maximum of 0.4 m/yr (Figure 2-2(c)), compared to a modern value of about 0.6 m/yr. Scenario 2 prescribes the modern surface wind stress, surface temperature but the same $E - P$ pattern as in Scenario 1. Scenario 2 provides a strong surface wind stress(Figure 2-2(d)) and a strong pole-equator surface temperature gradient (Figure 2-2(e)) in contrast to Scenario 1. All surface forcing patterns were zonally averaged, adjusted to be symmetric about the equator and then these zonally-averaged fields were used to drive the 3-d circulation model. Mixed surface boundary conditions were employed - the sea surface temperature (SST) is relaxed to a prescribed surface temperature (Haney, 1971), but, to avoid spurious feedbacks between the freshwater flux and local salinity, the effect of precipitation represented as a salinity flux, thus, $Q_S = S_o(E - P)$, where S_o is the mean surface salinity of the ocean. The mean salinity of the ocean assumed is 34.6 PSU.

2.2 Multiple circulation modes

2.2.1 Stable thermal mode ocean circulation

The ocean circulation resulting from Scenario 1 is highly asymmetric (Figure 2-3). Figure 2-3(a) is the vertically integrated horizontal stream function, it is the superposition of the wind-driven circulation (such as subtropical gyre, subpolar gyre) and the thermohaline circulation looping through the Tethys sea. The eastern boundary current at southern polar region is induced, not by wind, but by the strong sinking in the southern high latitudes reaching a maximum of 40 Sv (Figure 2-3(b)), considerably stronger than the modern. Large southward heat fluxes (~1.8 *PW*, Figure 2-3(d)) result in the south pole being some 6^oC warmer than the north pole (Figure 2-3(c)). Vigorous deep-reaching

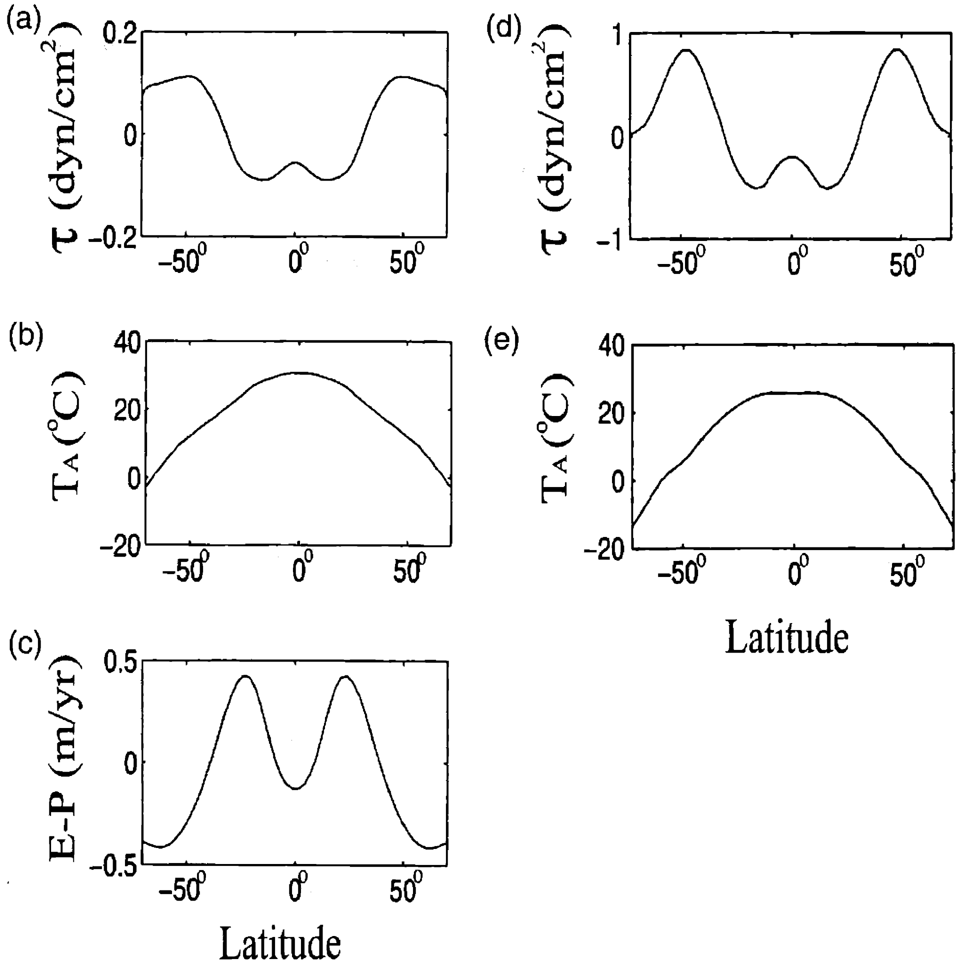

Figure 2-2: Surface forcing scenario 1 (a-c) and surface forcing scenario 2 (d-e). (a) Zonally-averaged surface wind stress (dyn/cm^2). (b) Zonally-averaged prescribed surface temperature T_A (^oC). (c) Zonally-averaged freshwater flux $(E - P)(m/yr)$. (d) Zonally-averaged surface wind stress (dyn/cm^2). (e) Zonally-averaged prescribed surface temperature T_A (^oC).

convection occurs in the southeast corner of the superocean, adjacent to Western South America and Western Antarctica, maintaining the deep water at about 5^oC there. We find that this thermally-driven circulation is rather stable. If the model is driven as in scenario 2 we still find an equilibrium solution with sinking in southern high latitudes. If the circulation is perturbed for many hundreds of years to induce northern hemispheric sinking by, for example, adding a net evaporation (0.1 m/yr) in the northern high latitude, and a net precipitation (0.1m/yr) in the southern high latitude, the solution always switches back to sinking in southern high latitude when symmetric forcing is restored (see also Marotzke and Willebrand, 1991). This polar overturning circulation is driven primarily by air-sea *heat* flux (a thermal mode).

This model result differs from the symmetric ocean circulation pattern for idealized ocean at Pangaean time obtained by Kutzbach et al.(1990), and must be a consequence of the different land-sea distribution and different surface boundary conditions. Evidently asymmetries in the late Permian land-sea distribution predisposes modeled deep-water formation in the south in our experiments and we do not restore the surface salinity to prescribed symmetric values.

It is interesting to note that a late Permian southern high latitude fossil forest deposit indicates warm polar climates (Taylor, et al., 1992), consistent with a strong southward ocean heat transport associated with sinking in southern high latitudes.

2.2.2 Unstable haline mode ocean circulation

Previous modeling studies have suggested that the thermohaline circulation is a nonlinear system, supporting multiple solutions which are highly sensitive to the surface freshwater forcing (Stommel, 1961; Bryan, 1986; Manabe and Stouffer, 1988; Marotzke and Willebrand, 1991). We find that if the amplitude of the freshwater flux is increased relative to the heat flux beyond a certain threshold, it is possible to find a prevalent HM of ocean circulation in which sinking occurs in the subtropics. This has very different implications for the oxygen cycle. As discussed in Zhang et al. (1999), the critical amplitude of fresh-

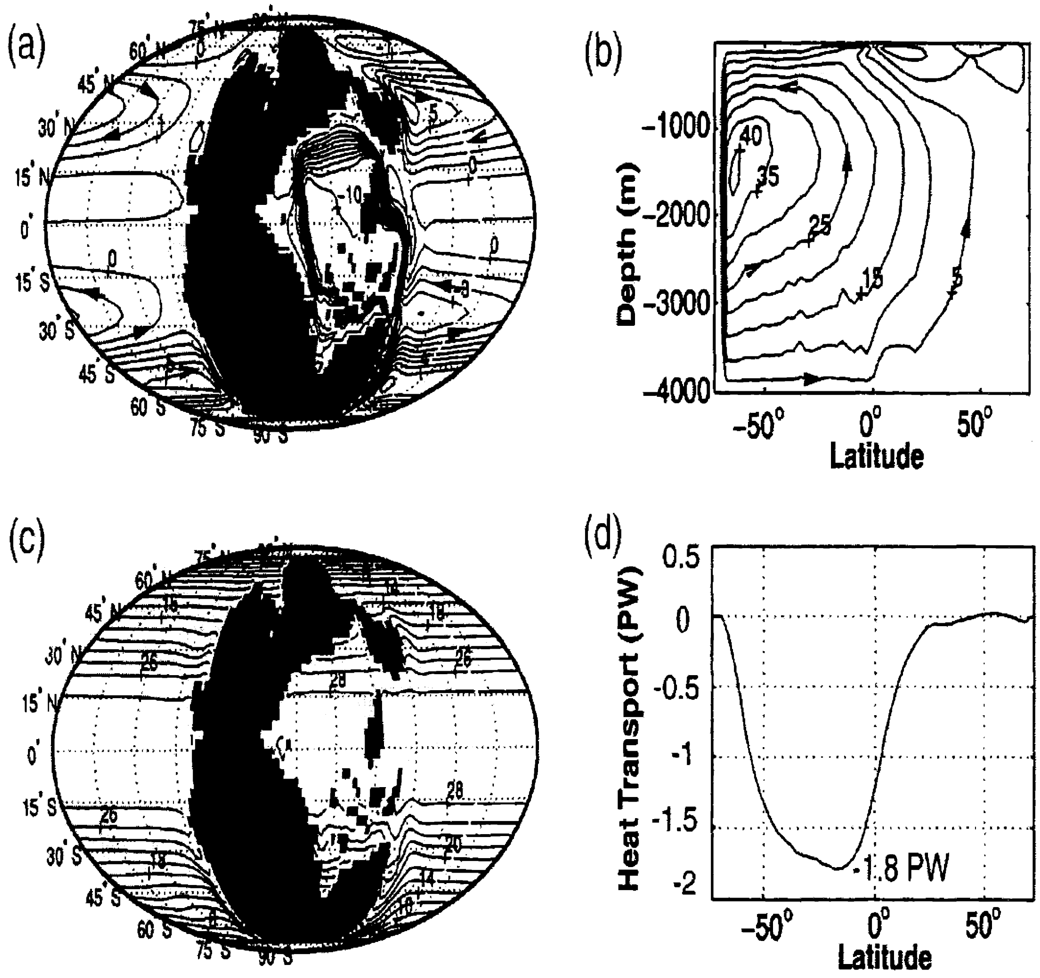

Figure 2-3: Possible late Permian TM ocean circulation. (a) Horizontal stream function (in Sv) of the late Permian TM, revealing a superposition of the wind-driven circulation (Sverdrupian gyres) and the thermohaline circulation looping through the Tethys Sea. (b) Overturning stream function (in Sv) of the late Permian TM. (c) Sea surface temperature (SST, ^oC). (d) Meridional ocean heat transport (PW).

water flux, beyond which the HM dominates, is sensitive to the diapycnal diffusivity $\widehat{M}$ in the ocean, because $\widehat{M}$ controls the strength of the overturning circulation, meridional ocean heat transport, thence SST and air-sea heat flux. For the values of vertical mixing assumed in our simulation of the modern circulation and the late Permian TM circulation (discussed above in chapter 2.2.1), $\widehat{M} = 5 \times 10^{-5} m^2/s$, we find that the threshold is close to $5 \times (E - P)$, i.e. the intensity of the hydrological cycle would have to be increased 5-fold for the HM to dominate. Because of fundamental constraints encapsulated in the Clausius-Clapeyron relationship, it is unrealistic to suppose that the late Permian climate had such an enhanced hydrological cycle. But the critical amplitude of freshwater flux decreases with $\widehat{M}$ (Zhang et al., 1999). The physics that control the level of diapycnal mixing in the ocean remain uncertain even for the modern ocean and may have been different in the past. Measurements of the vertical spread of deliberate tracer releases in the main thermocline (Ledwell et al., 1993) yield $\widehat{M} = 1.1 \times 10^{-5} m^2/s$, in the lower range of that which is assumed in large-scale ocean circulation models. $\widehat{M}$ is known to be spatially inhomogeneous becoming larger near boundaries where tidally induced mixing processes may dominate (Toole et al., 1994; Marotzke, 1997; Munk and Wunsch, 1998). If we reduce $\widehat{M}$ to $3 \times 10^{-5} m^2/s$ it is possible to obtain a HM forced with a more plausible $(E - P)$ flux.

We set up the late Permian ocean circulation model now with $\widehat{M} = 3 \times 10^{-5} m^2/s$ under forcing scenario 1, with $3.3 \times (E - P)$ (1.3 m/yr at maximum, about double the modern freshwater intensity) and found a quasi-steady solution with haline-induced sinking in the subtropics (Figure 2-4). In the HM, no eastern boundary current exists at polar regions (Figure 2-3(a)), because no deep convection occurs there. The overturning strength is much weaker than the TM ($\sim 14\ Sv$,Figure 2-3(b)), warm and salty intermediate water formed in the subtropics is induced by net evaporation there. Less heat is transported polewards (Figure 2-3(d)), the SST in both polar regions is about $0^o C$ (Figure 2-3(c)). The deep ocean becomes stagnant and well stratified. It is significant that, unlike the TM, the HM is prone to instability (Marotzke, 1989). In the quasi-steady HM the surface

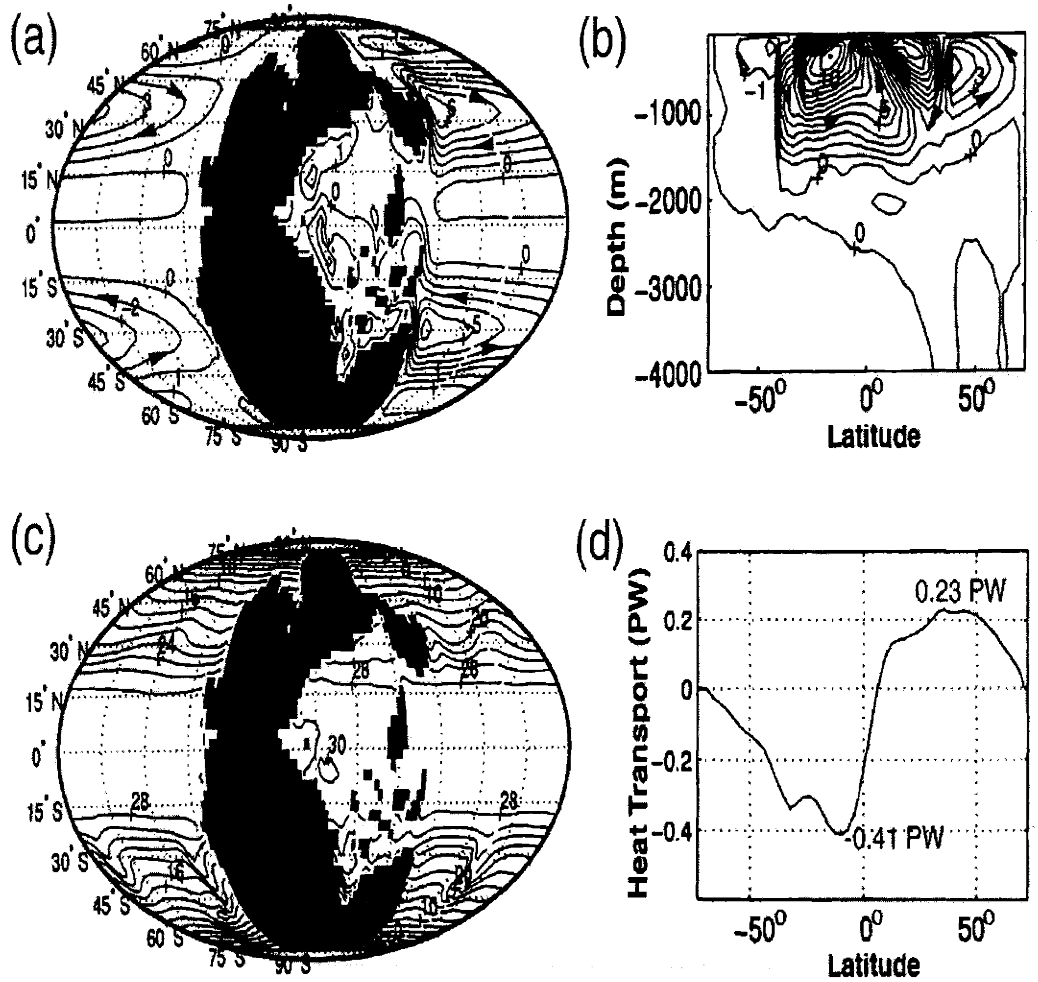

Figure 2-4: Possible late Permian HM ocean circulation. (a) Horizontal stream function (in Sv) of the late Permian HM. (b) Overturning stream function (in Sv) of the late Permian HM. (c) Sea surface temperature (SST, $°C$). (d) Meridional ocean heat transport (PW).

waters in polar regions are cold and fresh while the deep waters below are warm and salty. If a small perturbation mixes deep salty water up from below, cooling at the surface can induce polar convection switching the ocean to the transient TM. Once the energy is discharged, the ocean can gradually return to the quasi-steady HM, if $E-P$ forcing continues to dominate. An oscillation is thus possible between the transient TM and the quasi-steady HM (Huang, 1994). The time scale of the oscillation is of the order of hundreds or thousands of years and depends on the amplitude of $E-P$ and $\widehat{M}$. In this particular case, the time scale of the oscillation is about 3330 years.

Figure 2-5 shows the contrast of temperature and salinity distribution in the stable TM and the quasi-steady HM along the vertical section near the eastern boundary of the late Permian ocean (130^{o}E). In the stable TM, the temperature and salinity are well mixed at southern high latitudes (Figure 2-5(a),(b)), indicating strong deep convection there. Strong stratification occurs at northern high latitude surface, owing to the lack of deep convection there. In the quasi-steady HM, without deep convection, both polar surface waters show strong stratification in temperature and salinity (Figure 2-5(c), (d)), polar surface are cold and fresh, the deep ocean is well stratified with warm salty water formed at subtropics.

2.2.3 Surface buoyancy flux for two circulation modes

The different thermohaline circulation modes are driven by different surface buoyancy flux. The surface buoyancy flux $\mathcal{B}$ has two competing components: the heat flux and freshwater flux, they have opposite effect on the buoyancy flux in the high latitude.

$$\mathcal{B} = \frac{g}{\widehat{\rho}_0}(\frac{\alpha}{c_w}\mathcal{H} + \widehat{\rho}_0\beta S_0(E-P)) \qquad (2.1)$$

Here c_w is the heat capacity of water, $\mathcal{H}$ is the surface heat loss, $E-P$ is the surface freshwater flux, α, β are the thermal and saline expansion coefficient respectively, $\widehat{\rho}_0$ is the mean ocean density. Figure ?? shows the diagnosed zonally averaged surface buoyancy

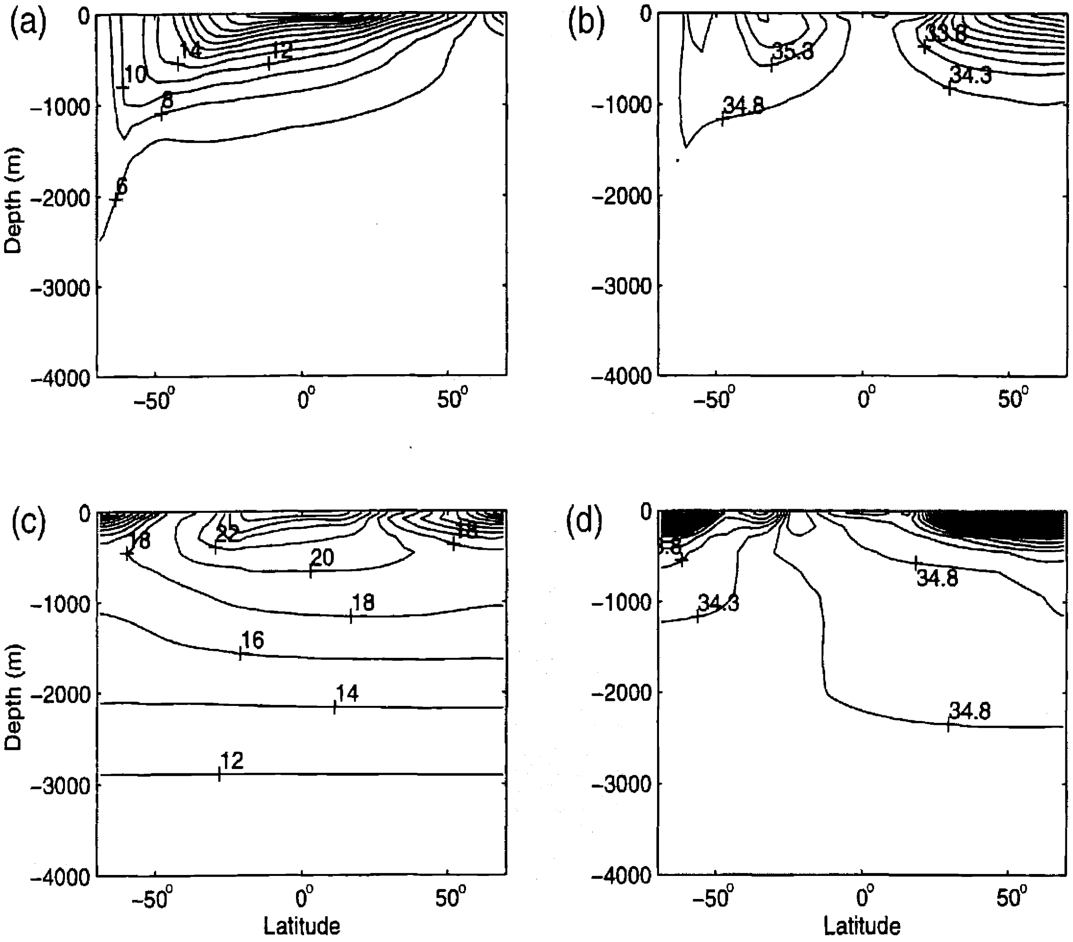

Figure 2-5: Vertical section of temperature and salinity near the eastern boundary of the late Permian ocean (130°E). (a) Temperature of the stable TM. (b) Salinity of the stable TM. (c) Temperature of the quasi-steady HM. (d) Salinity of the quasi-steady HM.

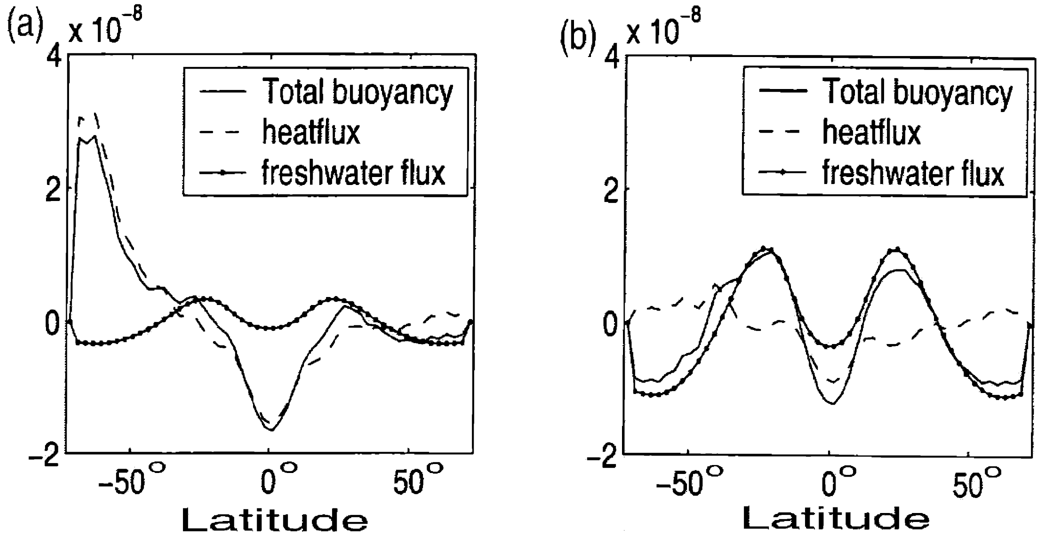

Figure 2-6: Diagnosed zonally averaged surface buoyancy flux (m^2/s^3) of (a) Late Permian TM circulation, (b) Late Permian HM circulation. (Total buoyancy flux (solid line), Heatflux component (dashed line), freshwater flux component (solid line with dot))

flux in different circulation modes. During the stable TM circulation in the late Permian ocean modeling, the peak of heatflux at southern polar region is much larger than that of the freshwater flux component (Figure ??(a)), i.e. the surface buoyancy flux is dominated by the air-sea heatflux, so deep convection occurs in the southern high latitude, dense water sinks and spreads over the bottom. This is consistent with huge amount of heat transport southwards (Figure 2-3(d)), inducing much warmer southern polar surface temperature than that of the air. During the HM, the freshwater component is strong enough to overcome the heatflux (Figure ??(b)), it peaks at the subtropical region where warm and salty intermediate water is formed there. The polar surface is less dense due to net precipitation, deep convection is shut off there. This is consistent with the weak poleward heat transport (Figure 2-4(d)), so that the polar surface temperature is very close to the air temperature. Notice that the warm and salty intermediate water is not formed at tropical regions, because the net precipitation there induces less dense surface water than that at depth.

2.3 Thermohaline oscillations

As discussed above in chapter 2.2.2, we obtained the thermohaline oscillation with enhanced freshwater flux forcing (1.3 m/yr for maximum of E-P) and weaker vertical diffusivity- $\widehat{M} = 3\times10^{-5}m^2/s$. Figure 2-7(a) shows the time series of mean ocean temperature for about 8000 years with a oscillatory period of about 3332 years, we can see two cycles of the oscillation. During the HM circulation the mean ocean temperature keeps increasing, during the transient TM, the mean ocean temperature drops very quickly. Figure 2-7(b) shows the time series of integrated global air-sea heatflux. During the transient TM, a huge amount of heat is released to the atmosphere from ocean convection region; during the long term HM, a little heat has been absorbed into the ocean from the atmosphere. Figure 2-8(a) shows the typical overturning stream function of the quasi-steady HM circulation before the switch to the transient TM. It is weak and shallow, warm and salty intermediate water is formed in subtropics, and upwells in polar region and tropics. Figure 2-8(b) shows the typical overturning stream function of the transient TM circulation, i.e. the flushing event, which is strong and deep with deep water formed in southern polar region, upwelling in tropics and northern hemisphere.

The switch from the quasi-steady HM to the transient TM is triggered by intense local convection in polar region, induced by meridional transports of warm salty surface water by a large scale eddy. Figure 2-9(a), (b) shows the sea surface temperature and salinity at year 4155, just before the switch from HM to transient TM. We can see large scale eddy which is much warmer and saltier than the mean polar surface water formed near the western boundary of the superocean at the southern polar region, this is the statically unstable region where strong local convection happens. Though the area of convection is small, once this eddy propagates eastward to the eastern boundary of the superocean at same latitude (typical convection region in the TM), the whole circulation begins to flip to the strong transient TM suddenly. When the surface convection region becomes less dense due to the precipitation there, the convection stops and the circulation returns back to the HM.

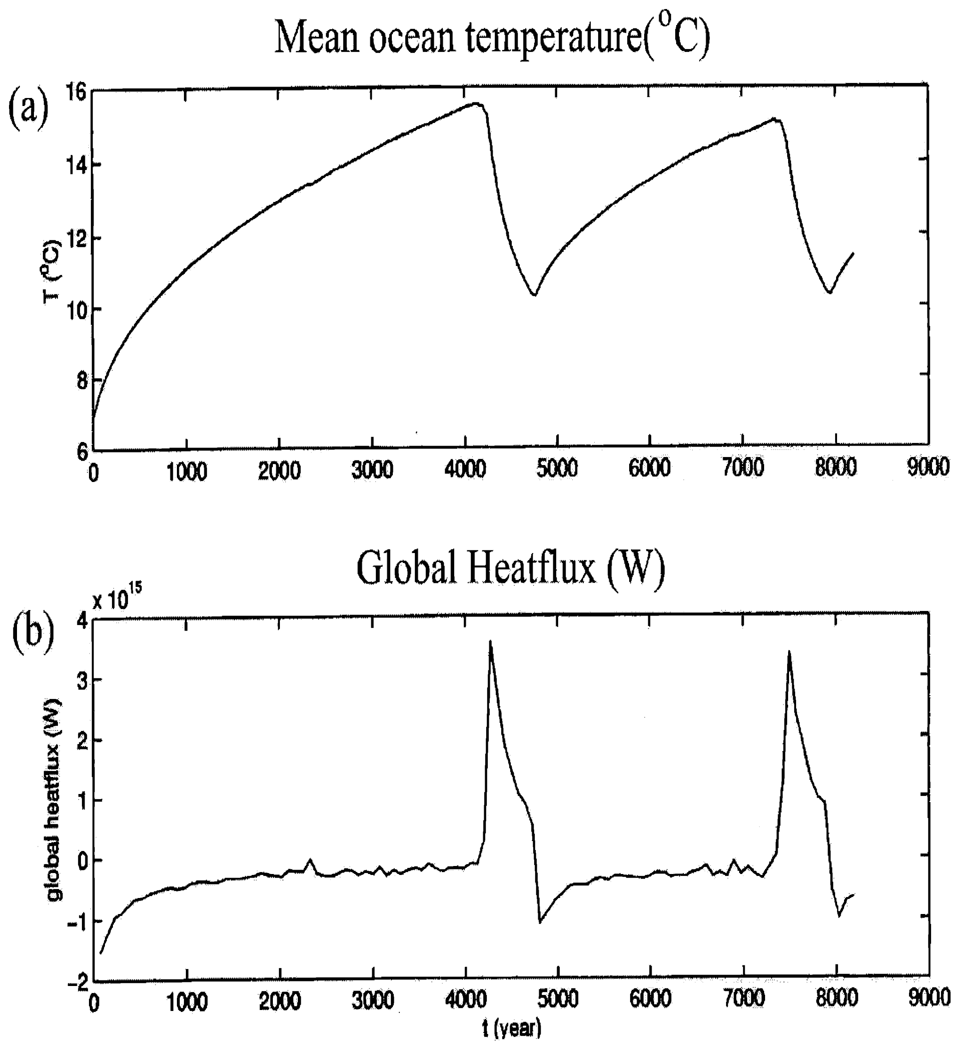

Figure 2-7: OGCM result: (a) Time series of mean ocean temperature . (b) Time series of global integrated surface air-sea heatflux.

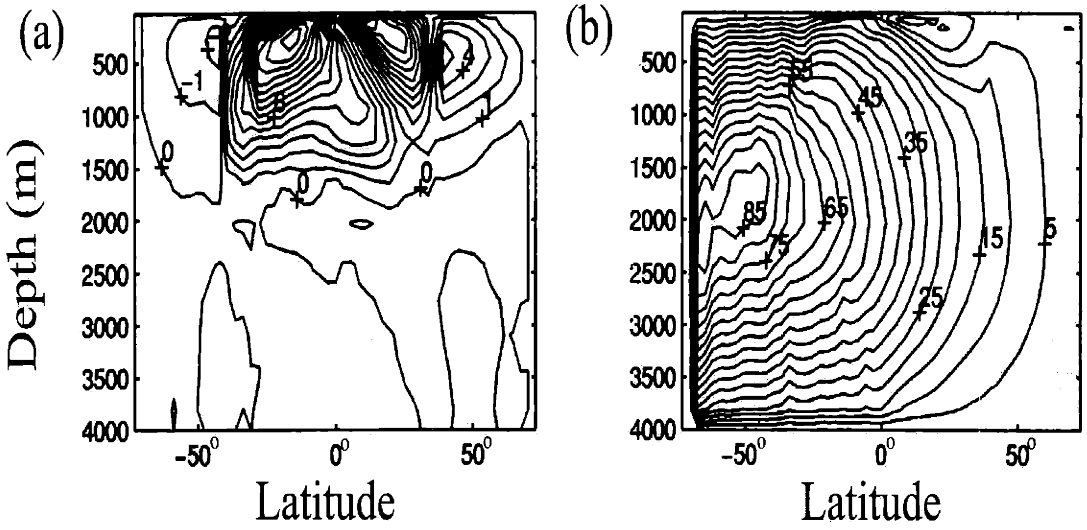

Figure 2-8: Overturning stream function. (a) Quasi-steady HM at year 3975. (b) Transient TM at year 4275.

2.4 Diagnosed properties of the OGCM results

Now let us look at the detailed properties of the thermohaline oscillations in our OGCM experiments of the late Permian ocean. Since the transient TM is asymmetric and deep convection happens at southern high latitudes, we divided the southern hemisphere ocean into three big boxes: low latitude surface box - the ocean region within latitude circle from 14.06°S to $36.56^{o}S$ and the surface level in the OGCM (50m), high latitude surface box - the ocean region within latitude circle from 36.56°S to $70.31^{o}S$ and the surface level in the OGCM (50m), deep ocean box - the ocean region within latitude circle from 14.06°S to $70.31^{o}S$ and all the levels below the surface level in the OGCM (3950m). In chapter 3 we will describe a simple 3-box model based on the diagnosis of the above three big boxes in the OGCM.

In this chapter and chapter 3, we use the symbols with a hat, ^, to represent the dimensional temperature, salinity, density and diffusivity; the symbols without a hat to

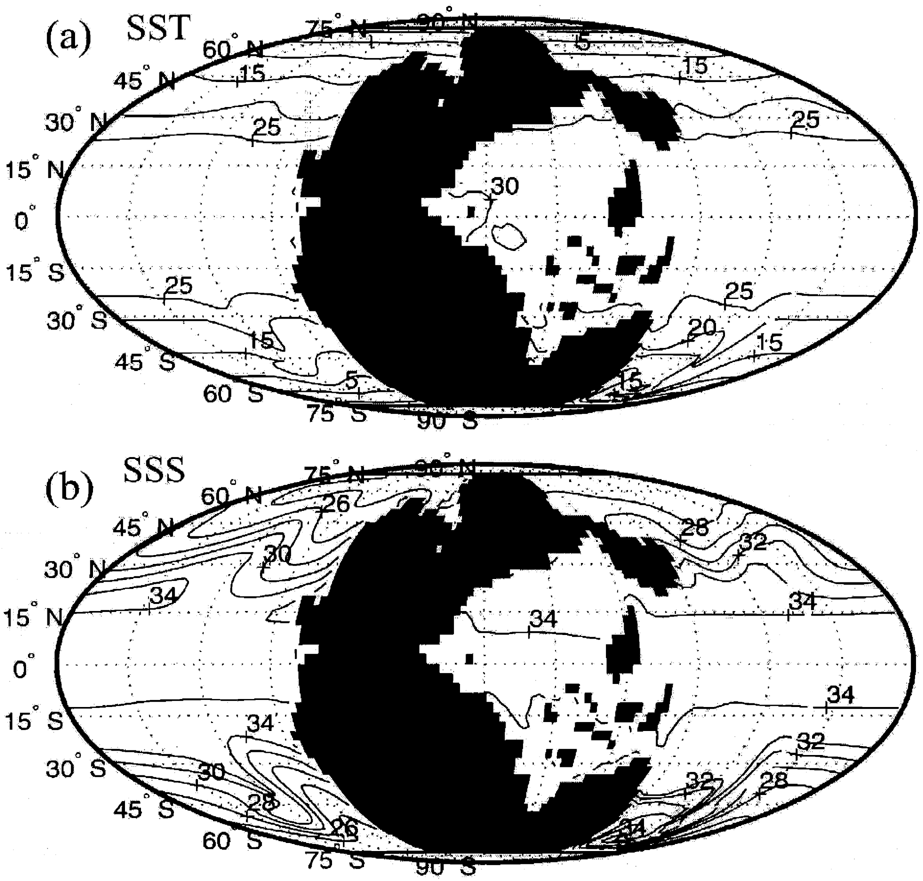

Figure 2-9: OGCM result: Sea surface temperature and salinity during the switch from the HM to the TM. (a) Sea surface temperature (SST) at year 4155. (b) Sea surface salinity (SSS) at year 4155.

represent the non-dimensional temperature, salinity, density and diffusivity. Figure 2-10 shows the time series of mean temperature $\widehat{T}_i$, salinity $\widehat{S}_i$ (i=l,h,d; l-low latitude surface, h-high latitude surface, d-deep ocean) in each box of the OGCM. The total salinity of the chosen regions is not conserved; during the transient TM, saltflux goes in from equator and northern hemisphere, then goes out when the TM terminates. To compare with the 3-box model (described in chapter 3) where the total salinity is conserved, the mean salinity anomaly of total three regions is subtracted from the salinity of each region, then the total salinity of the three regions showed here (Figure 2-10) are conserved. When $\widehat{T}_d$ keeps increasing, it corresponds to the long term HM; when $\widehat{T}_d$ begins to drop, it corresponds to the beginning of convection and strong transient TM; when $\widehat{T}_d$ starts to increase again, it corresponds to the end of convection and termination of the TM. We can see that the cycle is asymmetric here, the HM is much longer than the TM. Figure 2-11 shows the time series of the non-dimensional vertical density difference between surface boxes and deep ocean box respectively :

$$\Delta\rho_{ld} = \frac{\widehat{\rho}_l - \widehat{\rho}_d}{\widehat{\rho}_0 \alpha \Delta\widehat{T}_A}, \ \Delta\rho_{hd} = \frac{\widehat{\rho}_h - \widehat{\rho}_d}{\widehat{\rho}_0 \alpha \Delta\widehat{T}_A} \tag{2.2}$$

based on a linear equation of state for density. Here $\widehat{\rho}_i$ $(i = l, h, d)$ is the density of each box, $\Delta\widehat{T}_A = \widehat{T}_{Al} - \widehat{T}_{Ah}$ is the polar-equator surface air temperature difference, α is the thermal expansion coefficient. We also did the calculation based on nonlinear equation of state as used in our OGCM and obtained very similar results as showed here.

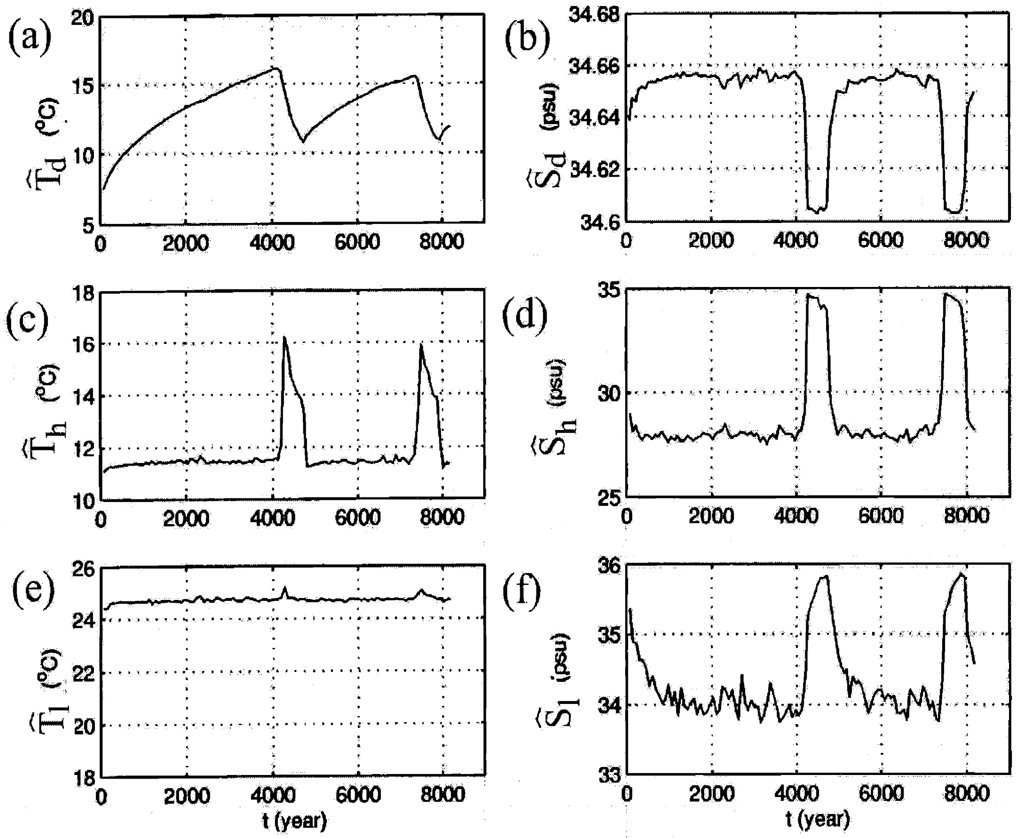

Figure 2-10: Time series of mean temperature and salinity in each diagnosed region of the OGCM. (a) $\widehat{T_d}$,(b) $\widehat{S_d}$, (c) $\widehat{T_h}$,(d) $\widehat{S_h}$, (e) $\widehat{T_l}$, (f) $\widehat{S_l}$.

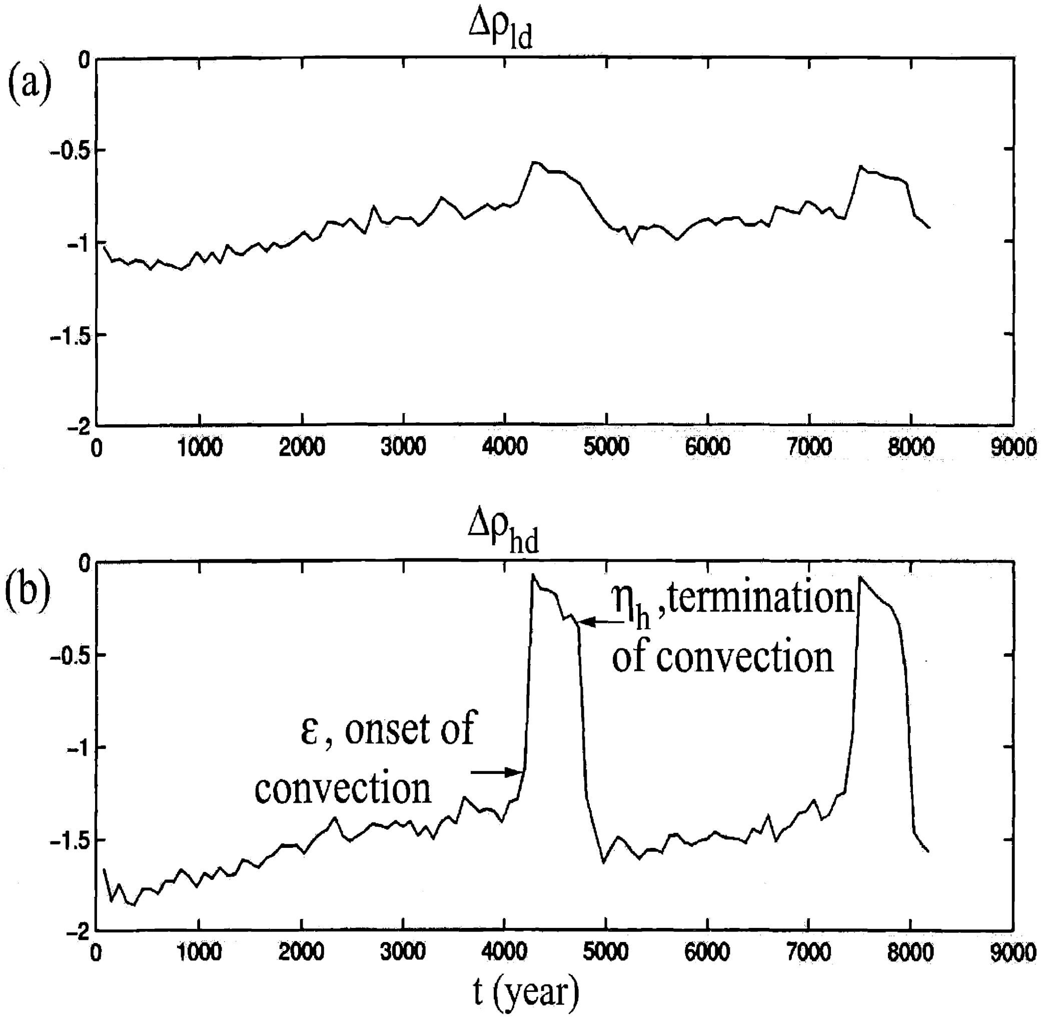

Figure 2-11: Time series of mean surface and deep ocean non-dimensional density difference of the OGCM. (a) $\Delta\rho_{ld}$, (b) $\Delta\rho_{hd}$.

From Figure 2-11(b), we can see that during the unsteady HM, the mean trend of $\Delta\rho_{hd}$ keeps increasing gradually, i.e. $d(\Delta\rho_{hd})/dt > 0$, until it reaches a certain threshold, i.e. $\Delta\rho_{hd} = \varepsilon \approx -1.1$, then suddenly strong polar convection starts, $\Delta\rho_{hd}$ jumps to a very high value and the circulation switches to the transient TM. The polar convection starts while the mean density structure is still statically stable, i.e. $\Delta\rho_{hd} = \varepsilon < 0$, consistent with that the convection only happens in a local statically unstable region at the high latitude surface (Figure 2-9), not in the whole polar region. The large warm salty surface eddy (Figure 2-9) is cooled quickly, thus the density within the eddy is much larger than other regions at the high latitude surface. As the abyssal temperature keeps increasing, the deep ocean density $\widehat{\rho}_d$ keeps decreasing until it becomes almost same as the density of the large scale eddy $\widehat{\rho}_{eddy}$ in the high latitude surface box, then suddenly strong deep convection happens there, thus

$$\Delta\rho_{hd} = \varepsilon \approx (\widehat{\rho}_h - \widehat{\rho}_{eddy})/(\widehat{\rho}_0\alpha\Delta\widehat{T}_A) < 0. \tag{2.3}$$

In the 3-box model which we will describe in chapter 3, we represent this local convection effect by introducing a threshold ε for the onset of polar convection.

During the switch from HM to TM, the mean polar surface temperature and salinity (Figure 2-10(c),(d)) increase significantly due to strong mixing and horizontal advection from low latitude to high latitude. During the transient TM, the mean trend of $\Delta\rho_{hd}$ (Figure 2-11(b)) keeps decreasing gradually , i.e. $d\left(\Delta\rho_{hd}\right)/dt < 0$ since the mean deep ocean density keeps increasing due to polar convection. Finally when the freshwater forcing becomes dominant, the surface density of the convective region becomes less than the deep ocean density, i.e. $\Delta\rho_{hd}$ reaches the threshold for the termination of polar convection: $\Delta\rho_{hd} = \eta_h \approx -0.3$ (Figure 2-11(b)), the convection stops and $\Delta\rho_{hd}$ drops suddenly to a very low value. In the 3-box model in chapter 3 , we will use $\Delta\rho_{hd} < \eta_h$ ($\eta_h > \varepsilon$) as the criterion for the termination of convection during the transient TM ($d(\Delta\rho_{hd})/dt < 0$) with $\Delta\rho_{hd} \geq \varepsilon$, here η_h is the threshold for the termination of convection in high latitude during the transient TM.

2.5 Summary

In summary, we have found that, depending on the vigor of the hydrological cycle and the level of diapycnal mixing in the ocean, the late Permian ocean circulation could have been in a TM or a HM. The TM, driven by large air-sea heatflux at southern high latitude, is stable to small perturbations; while the HM, driven by subtropical evaporation and polar precipitation, is inherently unstable. Periodical flushing events interrupt it every several thousand years, releasing a huge amount of energy, which is stored in the ocean for several thousand years during the quasi-steady HM, into the atmosphere in a very short period.

During the quasi-steady HM, the front separating warm salty subtropical surface and cold fresh polar surface is unstable, large scale eddies are developed to transport warm and salty water polewards. The physical mechanism for the development of large scale eddies is still unclear and worth further investigation. As the deep ocean density is kept decreasing with the continuous warming by subtropical sinking water, the density structure within a large scale eddy at polar region finally becomes statically unstable, and strong localized convection happens there. The diagnosis of the OGCM by dividing the southern ocean into three big boxes confirms the localized deep convection effect, i.e. during the flushing event, the polar convection starts with negative zonal mean density difference between polar surface and deep ocean (Figure 2-11(b)). This helps us understand the physical mechanism of the thermohaline oscillation and how to study it with a much simpler model, such as the box model described in chapter 3.

The thermohaline oscillation we obtained with the global OGCM configured with the late Permian bathymetry has similar properties to many other OGCMs configured with idealized single basin (Marotzke, 1989; Wright and Stocker, 1991; Weaver and Sarachik 1991a, b; Weaver et al. 1993; Winton and Sarachik 1993; Huang 1994). The enhanced hydrological cycle and the reduced diapycnal mixing required to obtain such oscillations remain unconstrained for the late Permian. The hydrological cycle is likely to be stronger than today's during warm equable climates, such as the late Permian or the Mid-Cretaceous. During the glacial period, huge runoff caused by ice-melting events may also enhance the total freshwater forcing. The diapycnal mixing we employed in the HM is within the lower range of what is often assumed in large-scale ocean circulation models.

Notice that, the weak shallow overturning stream function of the quasi-steady HM (Figure 2-8(b)) has two cells in each hemisphere: the direct thermal cell which sinks from subtropics and upwells to the tropical surface, and the indirect haline cell which sinks from subtropics but upwells to the polar surface. Since the deep convection during the flushing event happens in polar region, the indirect haline cell which advects warm and salty water to the region below polar surface is more important for the mode switch mechanism, it is the focus of our development of the simple box model for thermohaline oscillations in chapter 3.

Chapter 3

Self sustained thermohaline oscillations in a simple box model

3.1 Model description

To better understand the mechanism of thermohaline oscillation, we developed a simple 3-box model based on the OGCM results discussed in chapter 2. For simplicity, the 3-box model only represents a single hemisphere, it combines the Stommel-type box model (Figure 3-1(a)) with the Welander-type convection model (Figure 3-1(b)). It includes a low latitude surface box (from latitude 12^o to 35^o), high latitude surface box (from latitude 35^o to 70^o), and a deep ocean box (Figure 3-1(c)) . $\widehat{K}$ is the horizontal diffusivity between surface boxes, representing lateral eddy mixing. $\widehat{M_l}$, $\widehat{M_h}$ are the vertical diffusivities between surface and deep ocean in low and high latitudes respectively, they depend on the vertical density difference. Let $\widehat{T_l}$, $\widehat{T_h}$, $\widehat{T_d}$ be the mean temperature of the low latitude surface box, high latitude surface box and deep ocean box respectively, $\widehat{S_l}$, $\widehat{S_h}$, $\widehat{S_d}$ be the mean salinity of the low latitude surface box, high latitude surface box and deep ocean box respectively. At the air-sea surface, net mean freshwater flux F goes into the high latitude box, with same amount going out of the low latitude box. Sea surface temperature, $\widehat{T_l}$, $\widehat{T_h}$ are restored to the surface air temperature $\widehat{T}_{Al}, \widehat{T}_{Ah}$ with restoration rate λ, this is similar to the mixed boundary condition used in the OGCM. Let h be the surface box depth, H be the deep ocean box depth, V_l, V_h and V_d be the volume of each box, (here for the given latitude range of surface boxes, we have $V_l = V_h = V$), L be the horizontal distance between the center of surface boxes. The overturning stream function q (unit is Sv $=10^6\ m^3/s$) is assumed to be linearly proportional to the surface density gradient, similar to Stommel's box model :

$$q = \mu_q\ (\widehat{\rho}_h - \widehat{\rho}_l) \tag{3.1}$$

where $q > 0$ indicates a TM circulation (polar sinking, upwelling to low latitude surface), $q < 0$ indicates a HM circulation (subtropical sinking, upwelling to polar surface), μ_q is the constant of proportionality.

We use linear equation of state for seawater density :

$$\widehat{\rho}_i = \widehat{\rho}_0(1 - \alpha(\widehat{T}_i - \widehat{T}_r) + \beta(\widehat{S}_i - \widehat{S}_r)) \tag{3.2}$$

where $\widehat{\rho}_0, \widehat{T}_r, \widehat{S}_r$ are the referenced density, temperature and salinity respectively. α, β are the thermal and saline expansion coefficient respectively.

The dimensional dynamic equations for $\widehat{T}$, $\widehat{S}$ in each box are based on the upstream scheme. For example, the high latitude surface temperature $\widehat{T}_h$ evolves with the air-sea heat-flux, advection by the overturning circulation, mixing by the horizontal diffusion and vertical diffusion.

For the TM ($q > 0$), we have

$$\frac{d\widehat{T}_h}{dt} = \lambda(\widehat{T}_{Ah} - \widehat{T}_h) + \frac{q}{V_h}(\widehat{T}_l - \widehat{T}_h) + \frac{\widehat{K}}{L^2}(\widehat{T}_l - \widehat{T}_h) + \frac{\widehat{M}_h}{\frac{h+H}{2}h}(\widehat{T}_d - \widehat{T}_h) \tag{3.3}$$

For the HM ($q < 0$), we have

$$\frac{d\widehat{T}_h}{dt} = \lambda(\widehat{T}_{Ah} - \widehat{T}_h) - \frac{q}{V_h}(\widehat{T}_d - \widehat{T}_h) + \frac{\widehat{K}}{L^2}(\widehat{T}_l - \widehat{T}_h) + \frac{\widehat{M}_h}{\frac{h+H}{2}h}(\widehat{T}_d - \widehat{T}_h) \tag{3.4}$$

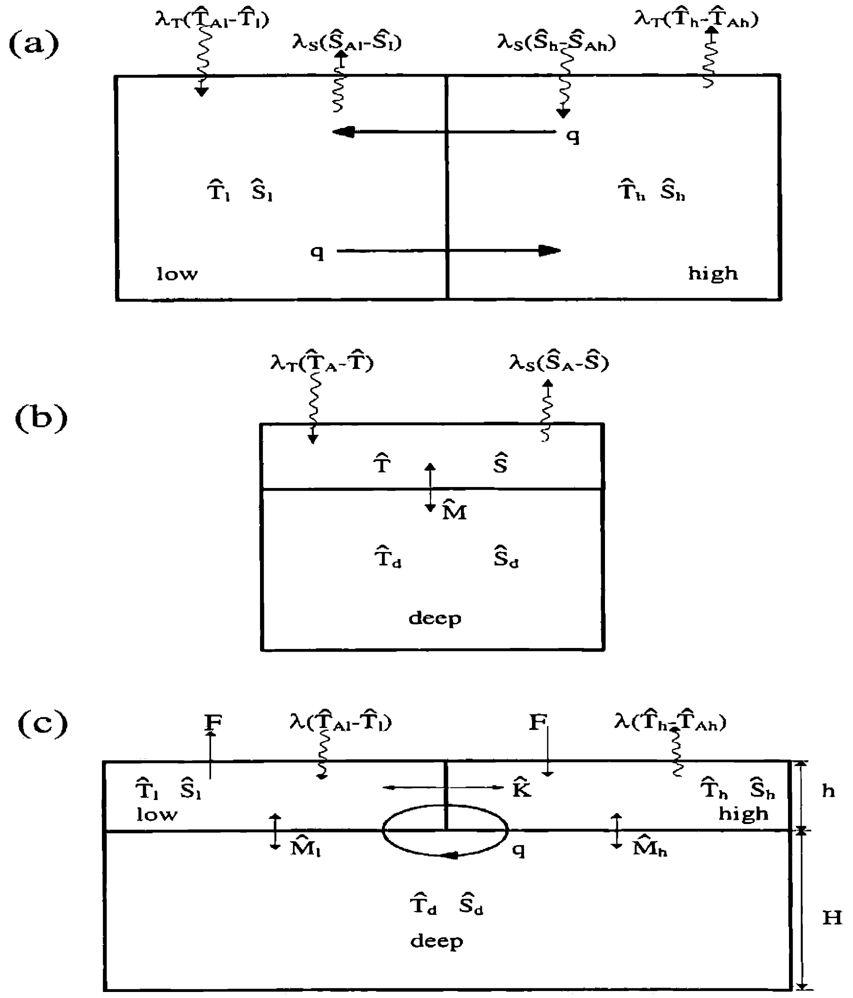

Figure 3-1: (a) Schematic diagram of the Stommel-type box model. (b) Schematic diagram of the Welander-type convection model. (c) Schematic diagram of the 3-box model. K is the horizontal diffusivity between surface boxes, M_l, M$_h$ is the vertical diffusivity at low and high latitude respectively. F is net mean freshwater flux, the sea surface temperature $\widehat{T_l}$, $\widehat{T_h}$ are restored to the air temperature $\widehat{T}_{Al}, \widehat{T}_{Ah}$ with restoration rate λ. q is the overturning strength. h is surface box depth, H is deep box depth.

We can write the above two equations into one suitable for both the TM ($q > 0$) and HM ($q < 0$) :

$$\frac{d\widehat{T}_h}{dt} = \lambda(\widehat{T}_{Ah}-\widehat{T}_h)+\frac{q}{2V_h}(\widehat{T}_l-\widehat{T}_d)+\frac{|q|}{2V_h}(\widehat{T}_l+\widehat{T}_d-2\widehat{T}_h)+\frac{\widehat{K}}{L^2}(\widehat{T}_l-\widehat{T}_h)+\frac{\widehat{M}_h}{\frac{h+H}{2}h}(\widehat{T}_d-\widehat{T}_h) \quad (3.5)$$

So the dimensional equations for all $\widehat{T}$, $\widehat{S}$ are :

$$\frac{d\widehat{T}_l}{dt} = \lambda(\widehat{T}_{Al}-\widehat{T}_l)+\frac{q}{2V_l}(\widehat{T}_d-\widehat{T}_h)+\frac{|q|}{2V_l}(\widehat{T}_d+\widehat{T}_h-2\widehat{T}_l)+\frac{\widehat{K}}{L^2}(\widehat{T}_h-\widehat{T}_l)+\frac{\widehat{M}_l}{\frac{h+H}{2}h}(\widehat{T}_d-\widehat{T}_l) \quad (3.6)$$

$$\frac{d\widehat{T}_h}{dt} = \lambda(\widehat{T}_{Ah}-\widehat{T}_h)+\frac{q}{2V_h}(\widehat{T}_l-\widehat{T}_d)+\frac{|q|}{2V_h}(\widehat{T}_l+\widehat{T}_d-2\widehat{T}_h)+\frac{\widehat{K}}{L^2}(\widehat{T}_l-\widehat{T}_h)+\frac{\widehat{M}_h}{\frac{h+H}{2}h}(\widehat{T}_d-\widehat{T}_h) \quad (3.7)$$

$$\frac{d\widehat{T}_d}{dt} = \frac{q}{2V_d}(\widehat{T}_h-\widehat{T}_l)+\frac{|q|}{2V_d}(\widehat{T}_h+\widehat{T}_l-2\widehat{T}_d)+\frac{\widehat{M}_l}{\frac{h+H}{2}2H}(\widehat{T}_l-\widehat{T}_d)+\frac{\widehat{M}_h}{\frac{h+H}{2}2H}(\widehat{T}_h-\widehat{T}_d) \quad (3.8)$$

$$\frac{d\widehat{S}_l}{dt} = \frac{F\widehat{S}_0}{h}+\frac{q}{2V_l}(\widehat{S}_d-\widehat{S}_h)+\frac{|q|}{2V_l}(\widehat{S}_d+\widehat{S}_h-2\widehat{S}_l)+\frac{\widehat{K}}{L^2}(\widehat{S}_h-\widehat{S}_l)+\frac{\widehat{M}_l}{\frac{h+H}{2}h}(\widehat{S}_d-\widehat{S}_l) \quad (3.9)$$

$$\frac{d\widehat{S}_h}{dt} = -\frac{F\widehat{S}_0}{h}+\frac{q}{2V_h}(\widehat{S}_l-\widehat{S}_d)+\frac{|q|}{2V_h}(\widehat{S}_l+\widehat{S}_d-2\widehat{S}_h)+\frac{\widehat{K}}{L^2}(\widehat{S}_l-\widehat{S}_h)+\frac{\widehat{M}_h}{\frac{h+H}{2}h}(\widehat{S}_d-\widehat{S}_h) \quad (3.10)$$

$$\frac{d\widehat{S}_d}{dt} = \frac{q}{2V_d}(\widehat{S}_h-\widehat{S}_l)+\frac{|q|}{2V_d}(\widehat{S}_h+\widehat{S}_l-2\widehat{S}_d)+\frac{\widehat{M}_l}{\frac{h+H}{2}2H}(\widehat{S}_l-\widehat{S}_d)+\frac{\widehat{M}_h}{\frac{h+H}{2}2H}(\widehat{S}_h-\widehat{S}_d) \quad (3.11)$$

Here $\widehat{S}_0$ is ocean mean salinity. At the air-sea surface there is no net salt flux into the atmosphere, the total salinity of the 3-boxes is conserved, hence there are only 5 independent dynamic variables.

3.1.1 Non-dimensional equations

To make non-dimensional analysis, let $\Delta\widehat{T}_A = \widehat{T}_{Al} - \widehat{T}_{Ah}$(polar-equator surface air temperature difference), $\overline{\widehat{T}_A} = (\widehat{T}_{Al} + \widehat{T}_{Ah})/2$ (mean surface air temperature), the correspondent non-dimensional parameters are:

$$\gamma = \frac{\Delta\widehat{T}_A}{\overline{\widehat{T}_A}}\text{(polar-equator air temperature difference)}$$

$$c = \frac{2F}{\lambda h}\text{(freshwater flux)}$$

$$K = \frac{2\widehat{K}}{L^2\lambda}\text{(horizontal diffusivity)}$$

$$M_l = \frac{\widehat{M}_l}{\frac{h+H}{2}h\lambda}\text{(vertical diffusivity in low latitudes)}$$

$$M_h = \frac{\widehat{M}_h}{\frac{h+H}{2}h\lambda}\text{(vertical diffusivity in high latitudes)}$$

$$\mu_f = \frac{\mu_q\widehat{\rho}_0\alpha\overline{\widehat{T}_A}}{\lambda V}, \quad \delta = \frac{h}{H}, \quad R = \frac{\beta\widehat{S}_0}{\alpha\Delta\widehat{T}_A}$$

The new non-dimensional dynamical variables are:

$$\Delta T = \frac{\widehat{T}_l - \widehat{T}_h}{\Delta \widehat{T}_A}, \overline{T} = \frac{\widehat{T}_l + \widehat{T}_h}{2\widehat{T}_A}, T_d = \frac{\widehat{T}_d}{\widehat{T}_A}, \Delta S = \frac{\widehat{S}_l - \widehat{S}_h}{\widehat{S}_0}, \overline{S} = \frac{\widehat{S}_l + \widehat{S}_h}{2\widehat{S}_0}, S_d = \frac{\widehat{S}_d}{\widehat{S}_0}$$

and the non-dimensional overturning stream function is $f = q/(\gamma \lambda V)$, the non-dimensional form of equation (3.1) becomes :

$$f = \mu_f \left(\Delta T - R \Delta S \right) \tag{3.12}$$

Let $t' = \lambda t$ be the non-dimensional time, now based on the dimensional dynamic equations (3.6 to 3.11), we can write down the non-dimensional dynamic equations of the new non-dimensional dynamics variables ΔT, $\overline{T}$, T_d, ΔS, $\overline{S}$, S_d for both TM ($f > 0$) and HM ($f < 0$) circulation :

$$\frac{d\Delta T}{dt'} = 1 - \Delta T + f\ (T_d - \overline{T}) - \frac{3}{2}\ |f|\,\gamma \Delta T - K\Delta T + M_l\left(\frac{T_d - \overline{T}}{\gamma} - \frac{\Delta T}{2}\right) - M_h\left(\frac{T_d - \overline{T}}{\gamma} + \frac{\Delta T}{2}\right) \tag{3.13}$$

$$\frac{d\overline{T}}{dt'} = 1 - \overline{T} + \frac{\gamma}{2}|f|\ (T_d - \overline{T}) + \frac{\gamma^2}{4}\ f\ \Delta T + \frac{M_l}{2}(T_d - \overline{T} - \frac{\gamma \Delta T}{2}) + \frac{M_h}{2}(T_d - \overline{T} + \frac{\gamma \Delta T}{2}) \tag{3.14}$$

$$\frac{dT_d}{dt'} = -\delta(\frac{\gamma}{2}|f|\ (T_d - \overline{T}) + \frac{\gamma^2}{4}\ f\ \Delta T + \frac{M_l}{2}(T_d - \overline{T} - \frac{\gamma \Delta T}{2}) + \frac{M_h}{2}(T_d - \overline{T} + \frac{\gamma \Delta T}{2})) \tag{3.15}$$

$$\frac{d\Delta S}{dt'} = c + f\ \gamma(S_d - \overline{S}) - \frac{3}{2}\ |f|\,\gamma \Delta S - K\Delta S + M_l(S_d - \overline{S} - \frac{\Delta S}{2}) - M_h(S_d - \overline{S} + \frac{\Delta S}{2}) \tag{3.16}$$

$$\frac{d\overline{S}}{dt'} = \frac{\gamma}{2}|f| \ (S_d - \overline{S}) + \frac{\gamma}{4} \ f \ \Delta S + \frac{M_l}{2}(S_d - \overline{S} - \frac{\Delta S}{2}) + \frac{M_h}{2}(S_d - \overline{S} + \frac{\Delta S}{2}) \qquad (3.17)$$

$$\frac{dS_d}{dt'} = -\delta \frac{d\overline{S}}{dt'} \qquad (3.18)$$

We can solve for the steady solutions and the time-dependent solutions of the above equations respectively.

3.1.2 Representation of convection

The non-dimensional vertical diffusivity M_l, M_h in the above equations are not invariant due to convection. To include the effect of convection, we calculate the non-dimensional mean vertical density difference between the surface boxes and deep ocean box $\Delta\rho_i$ $(i = ld, hd)$ as defined in Eq. (2.2) in chapter 2. If no convection happens in low or high latitude, then $M_l = M$ or $M_h = M$, here $M = 2\widehat{M} \ / \ ((h + H)h\lambda)$ is the background non-dimensional vertical diffusivity, $\widehat{M}$ is the dimensional background vertical diffusivity. Whenever the density difference allows convection to happen in low(high) latitude, M_l (M_h) also changes with it, and it becomes much larger than M.

Based on the diagnosis of the OGCM in chapter 2, we represent the effect of local polar convection in this 3-box model by introducing a threshold , ε, for the onset of polar convection. Here the physical meaning of ε is the same as that found in the OGCM (see chapter 2 and Figure 2-11(b)): during the unsteady HM $(d\left(\Delta\rho_{hd}\right)/dt > 0)$, when the mean non-dimensional density difference between the polar surface and deep ocean reaches this threshold, i.e. $\Delta\rho_{hd} = \varepsilon$, polar convection starts; whether we are in HM or TM, when $\Delta\rho_{hd} < \varepsilon$, no polar convection occur. Here $\varepsilon < 0$ represents the effect of localized polar convection discussed in chapter 2. Similarly, when the system is in polar convection phase, we introduce a threshold, η_h, for the termination of polar convection (see chapter 2 and Figure 2-11(b)): when $\Delta\rho_{hd} < \eta_h$ during the transient TM

$(d(\Delta\rho_{hd})/dt < 0)$, the polar convection terminates. During the polar convective phase, the high latitude surface density is more homogeneous than that in the non-convective phase, so $\eta_h > \varepsilon$ and η_h is set to be close to zero in the box model.

In summary, we can write down the simplified rules for convective adjustment which include the effect of localized convection in the 3-box model :

At high latitudes,

if $\Delta\rho_{hd} < \varepsilon$, then $M_h = M$ (no convection)

if $\Delta\rho_{hd} \geq \varepsilon$,and $d\left(\Delta\rho_{hd}\right)/dt > 0$,then $M_h = M_{sc}$ (strong convection)

if $\Delta\rho_{hd} \geq \varepsilon$,and $d\left(\Delta\rho_{hd}\right)/dt \leq 0$, then

  if $\Delta\rho_{hd} < \eta_h$, then $M_h = M$ (no convection)

  if $\Delta\rho_{hd} \geq \eta_h$, then $M_h = M_{sc}$ (strong convection)

Here $M_{sc} \gg M$, indicating the sinking of cold fresh water in high latitude is strong and deep.

At low latitudes,

if $\Delta\rho_{ld} < \eta_l$, then $M_l = M$ (no convection)

if $\Delta\rho_{ld} \geq \eta_l$, then $M_l = M_{wc}$ (weak convection)

Here $M_{sc} > M_{wc} \gg M$, indicating the sinking of warm salty water in low latitude is weak and shallow compared to the strong and deep convection in high latitude. As the density distribution in low latitude is more homogeneous, we use same threshold, η_l, for the onset and termination of convection in low latitude, and it is close to zero. The reason that η_l is slightly less than zero is to avoid numerical decay oscillations caused by the discontinuity in M_l (Welander, 1982). Similarly, the reason that η_h is slightly above zero is to avoid numerical false oscillations caused by the discontinuity in M_l.

3.2 Steady solutions of the 3-box model

Let us first look at the steady solutions of the 3-box model. The steady state solutions of Eq. (3.13-3.18) can be solved by making the RHS of the equations equal to zero, then writing $\Delta T, \overline{T}, T_d, \Delta S, \overline{S}, S_d$ in terms of f . Substituting the expression of $\Delta T, \Delta S$ into Eq. (3.12) gives a fifth order equation for f:

$$f = \frac{2\mu_f \,(M_l + M_h + |f|\ \gamma)}{(M_l + M_h + 2\,|f|\ \gamma)^2 - (M_h - M_l)^2 + 2(K+1)(M_l + M_h + |f|\ \gamma)}$$

$$-\frac{2\mu_f \,(M_l + M_h + |f|\ \gamma) Rc}{(M_l + M_h + 2\,|f|\ \gamma)^2 - (M_h - M_l)^2 + 2K(M_l + M_h + |f|\ \gamma)} \tag{3.19}$$

Only the real roots of this equation are physically possible solutions. Substituting the appropriate vertical diffusivities M_l, M_h for the corresponding convective/non-convective states into Eq. (3.19), we can obtain the steady TM ($f > 0$) and HM ($f < 0$) for given parameters.

For a steady TM ($f > 0$), the non-dimensional mean density difference between surface and deep ocean boxes can be obtained from Eq. (3.13-3.18 and 3.12) as:

$$\Delta\rho_{ld} = -\frac{f}{\mu_f}\frac{M_h + \gamma f}{M_l + M_h + \gamma f} \tag{3.20}$$

$$\Delta\rho_{hd} = \frac{f}{\mu_f}\frac{M_l}{M_l + M_h + \gamma f} \tag{3.21}$$

From the above relations, we know that $\Delta\rho_{ld} < 0$ and $\Delta\rho_{hd} > 0$ because $f > 0$, i.e. for steady TM ($f > 0$) the low latitude surface is always less dense than the deep ocean, the high surface is always denser than the deep ocean. Combining with the rules of convective adjustment, we can see that, for physically possible steady TM ($f > 0$), no convection happens in low latitude ($M_l = M$) while strong convection happens in polar region ($M_h = M_{sc}$). Substitute $M_l = M, M_h = M_{sc}$ into Eq. (3.19), we can obtain the steady TM solutions for given parameters.

For steady HM ($f < 0$), the non-dimensional mean density difference between surface and deep ocean boxes can be obtained from Eq. (3.13-3.18 and 3.12) as:

$$\Delta\rho_{ld} = -\frac{f}{\mu_f}\frac{M_h}{M_l + M_h - \gamma f} \tag{3.22}$$

$$\Delta\rho_{hd} = \frac{f}{\mu_f}\frac{M_l - \gamma f}{M_l + M_h - \gamma f} \tag{3.23}$$

From the above relations, we know that $\Delta\rho_{ld} > 0$ and $\Delta\rho_{hd} < 0$ because $f < 0$, i.e. for steady HM ($f < 0$) the low latitude surface is always denser than the deep ocean, the high surface is always less dense than the deep ocean. For physically possible steady HM ($f < 0$), weak convection happens in low latitude ($M_l = M_{wc}$), no convection happens in polar region ($M_h = M$). Substituting $M_l = M_{wc}, M_h = M$ into Eq. (3.19), we can obtain the steady HM solution for given parameters.

3.2.1 Regions on the bifurcation diagram

Figure 3-2 shows the steady TM and HM non-dimensional overturning stream function f as a function of the non-dimensional freshwater forcing c by solving the real roots of Eq. (3.19) for fixed other parameters, i.e. the bifurcation diagram on the f-c plane. The constants of the 3-box model are summarized in Table 3.1. Other fixed parameters in Figure (3-2) are $\Delta\widehat{T_A} = 14K$, $\overline{\widehat{T_A}} = 291K$, thus $\gamma = 0.0481$, $R = 8.75$. $K = 0.015$ ($\widehat{K} = 1 \times 10^4\ m^2/s$), $M = 0.0025$ ($\widehat{M} = 3.33 \times 10^{-5}\ m^2/s$), $M_{wc} = 0.1$, $M_{sc} = 0.2$, $\mu_f = 1.5$ (according to modern ocean overturning strength and surface density gradient). $f = \widehat{q}/(\gamma\lambda V)$, so when $\widehat{q} = 21Sv$, $f = 1$.

Similar to Stommel's box model (1961), there are three branches of steady solutions on the f-c plane (Figure 3-2). The upper one (thin solid line) is the stronger stable steady TM ($f > 0$), the middle one (dashed line) is the weaker unstable steady TM ($f > 0$), both obtained with $M_l = M, M_h = M_{sc}$ (polar convection). The lower one is the steady HM ($f < 0$) obtained with $M_l = M_{wc}, M_h = M$ (subtropical convection).

Even with convective adjustment, if $\varepsilon = 0$, the steady HM will always be stable as in Stommel's box model (1961); but if $\varepsilon < 0$ (localized polar convection), the steady HM

Table 3.1: Constants of the 3-Box model of thermohaline circulation.

constant	value
α (Thermal expansion coefficient)	2×10^{-4} (K^{-1})
β (Saline expansion coefficient)	7×10^{-4} (PSU^{-1})
L (Horizontal distance between surface boxes)	3190 (km)
V (Surface box volume)	3.265×10^{15} (m^3)
λ (Temperature restoration rate)	1/90 (day^{-1})
$\widehat{S}_0$ (Mean ocean salinity)	35 (PSU)
h (Surface box depth)	50 (m)
H (Deep ocean box depth)	4000 (m)

could be unstable and there could be four different regions on the bifurcation diagram (Figure 3-2), separated by three critical value of freshwater flux ($c_{r1} < c_{r2} < c_{r3}$):

Region I ($c \leq c_{r1}$) : only the globally stable steady TM exists.

Region II ($c_{r1} < c < c_{r2}$) : both the locally stable steady TM and the locally stable limit cycle can exist, depending on initial conditions.

Region III ($c_{r2} \leq c \leq c_{r3}$) : only the globally stable limit cycle exists.

Region IV ($c_{r3} < c$) : only the globally stable steady HM exists.

The stability of the steady solution is studied with linear analysis, see Appendix A. The stability of the limit cycle is detected numerically.

We now discuss the regions in details. On the $f - c$ plane in Figure 3-2, c_{r0}, c_{r2} are the two bifurcation points, i.e. when $c_{r0} < c < c_{r2}$, all three steady solutions (two TM, one HM) exist; when $c < c_{r0}$ only one steady TM exists; when $c > c_{r2}$ only one steady HM exists. Here $c_{r2} \approx 0.0047$ for the given parameters.

For steady HM ($f < 0$), the non-dimensional mean density difference between high latitude surface and deep ocean boxes $\Delta\rho_{hd}$ can be obtained from Eq. (3.13-3.18 and 3.12) as:

$$\Delta\rho_{hd} = \frac{f}{\mu_f} \frac{M_l - \gamma f}{M_l + M_h - \gamma f} \tag{3.24}$$

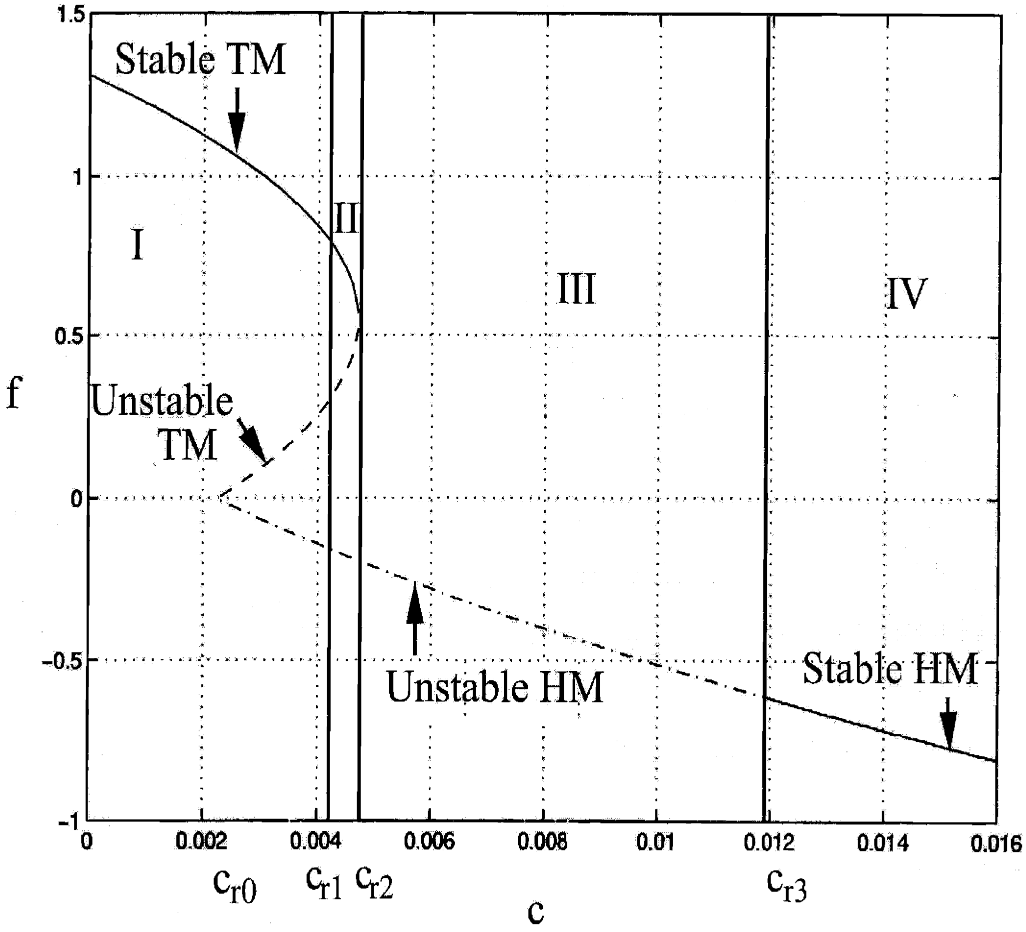

Figure 3-2: Bifurcation diagram on the f-c plane of the 3-box model. Stable TM (thin solid line), unstable TM (dashed line), unstable HM (dot dashed line), stable HM (thin solid line). Region I ($c \leq c_{r1}$) : only the globally stable steady TM exists. Region II ($c_{r1} < c < c_{r2}$) : both the locally stable steady TM and the locally stable limit cycle exist, depends on initial conditions. Region III ($c_{r2} \leq c \leq c_{r3}$) : only the globally stable limit cycle exists. Region IV ($c_{r3} < c$) : only the globally stable HM exists.

There is a critical value c_{r3} determined by substituting $\Delta\rho_{hd} = \varepsilon$ and $M_l = M_{wc}$, $M_h = M$ into Eq.(3.24):

$$\Delta\rho_{hd} = \frac{f(c_{r3})}{\mu_f} \frac{M_{wc} - \gamma\ f(c_{r3})}{M_{wc} + M - \gamma\ f(c_{r3})} = \varepsilon \tag{3.25}$$

when $c > c_{r3}$, we have $\Delta\rho_{hd} < \varepsilon$, the steady HM is stable (thin solid line); when $c \leq c_{r3}$, we have $\Delta\rho_{hd} \geq \varepsilon$, the steady HM is unstable (dot dashed line) according to the convective adjustment, i.e. a small perturbation which leads to $d\left(\Delta\rho_{hd}\right)/dt > 0$ would trigger polar convection ($M_h = M_{sc}$), making the system jump away from the steady HM instantaneously to a transient TM and it will never return to the steady HM.

In region III ($c_{r2} \leq c \leq c_{r3}$), no stable steady solution exists, the system has to oscillate: As the steady HM is the only stable solution without convective adjustment, the system will evolve towards it, i.e. $d\left(\Delta\rho_{hd}\right)/dt > 0$ when no polar convection happens and $\Delta\rho_{hd} < \varepsilon$ initially. When the condition $\Delta\rho_{hd} = \varepsilon$ is satisfied, polar convection suddenly starts, the system jumps away before it reaches the steady HM, the strong convection increases the polar surface density significantly, makes the circulation switch to the transient non-steady TM ($d\left(\Delta\rho_{hd}\right)/dt < 0$, $f > 0$). Since no steady TM exists, the freshwater flux gradually becomes dominant, $\Delta\rho_{hd}$ keeps decreasing until it becomes less than η_h, then the polar convection terminates, the system switches back to the quasi-steady HM ($f < 0$) and once again evolves towards the steady HM, completing the limit cycle. This is a globally stable limit cycle, small perturbations will not destroy it and it can be reached from any initial conditions.

In region IV ($c_{r3} < c$), the steady HM always satisfies $\Delta\rho_{hd} < \varepsilon$, thus it is stable globally, no limit cycle exists.

In region I ($c \leq c_{r1}$), when $c < c_{r0}$, only one globally stable steady TM exists; when $c_{r0} \leq c \leq c_{r1}$, the basin of attraction of the stable steady TM in the phase space is big enough that when the unstable HM switches to the transient TM due to polar convection, it will be attracted by the globally stable steady TM finally and stay there forever, thus no limit cycle exists, only one globally stable steady TM exists no matter what initial conditions.

In region II ($c_{r1} < c < c_{r2}$), the basin of attraction of the stable steady TM in the phase space is small enough so that the whole limit cycle is outside this basin of attraction, the oscillation could still exist depending on the initial condition: in the phase space, if the initial state is close to the stable steady TM, then it will evolve until reaching the locally stable steady TM; if the initial state is close to the steady HM, then it will evolve until reaching the locally stable limit cycle and keep oscillating. Since the system's phase space is 5-dim, it is very difficult to find the value of c_{r1} analytically, we can only get its value by numerical method (discussed in chapter 3.3), $c_{r1} \approx 0.0043$ for the given parameters.

The thermohaline oscillations are possible only in the window of the freshwater forcing in region II and III. This is consistent with the 2-d OGCM results found by Winton and Sarachik (1993). They found that such oscillations exist for certain range of freshwater forcing, when the freshwater forcing is very large, a stable steady HM exists.

Similarly we can plot the bifurcation diagram on $f - M$ plane (Figure 3-3) with other fixed parameters as in Figure 3-2 and $c = 0.0065$ ($F = 0.65m/yr$). In Figure 3-3, there are two critical values $M_{r1} \approx 0.0199$ (bifurcation point), $M_{r2} \approx 0.0209$ and three regions for the physically probable solutions on the f-M plane:

Region I ($M_{r2} \leq M$) : only the globally stable steady TM exists.

Region II ($M_{r1} < M < M_{r2}$) : both the locally stable steady TM and the locally stable limit cycle exist, depending on initial conditions.

Region III ($M \leq M_{r1}$) : only the globally stable limit cycle exists.

The thermohaline oscillations are possible only in the window of the vertical diffusivity in region II and III; here we do not have region IV in which only the stable steady HM exists. For much larger value of c, region IV on the f-M plane is also possible.

In our modern climate, $c < c_{r2}$, we have the stable steady TM circulation; it is hard to reach region III. But the bifurcation point, c_{r2}, (beyond which no TM exists) is also sensitive to parameter γ. In Figure 3-4, we show the non-dimensional TM overturning

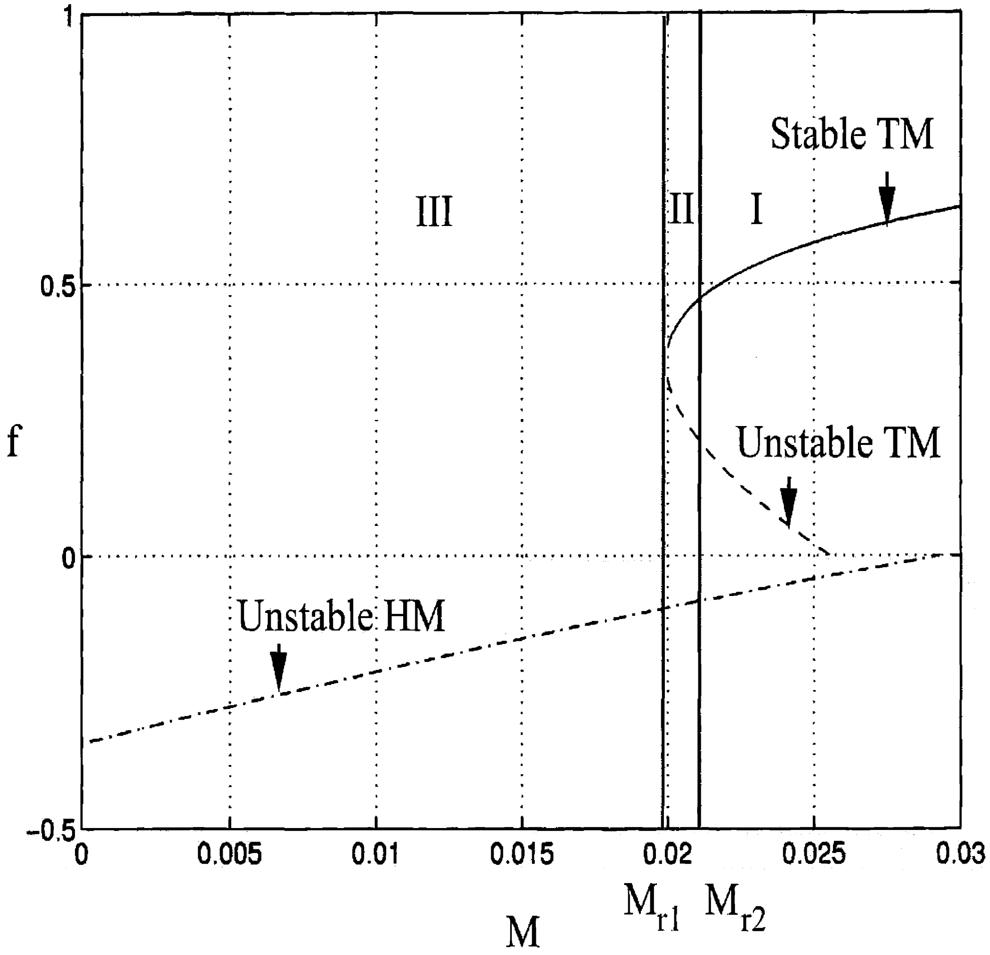

Figure 3-3: Bifurcation diagram on the f-M plane of the 3-box model. Stable TM (thin solid line), unstable TM (dashed line), unstable HM (dot dashed line). Region I ($M_{r2} \leq M$) : only the globally stable steady TM exists. Region II ($M_{r1} < M < M_{r2}$) : both the locally stable steady TM and the locally stable limit cycle exist, depends on initial conditions. Region III ($M \leq M_{r1}$) : only the globally stable limit cycle exists.

stream function f vs. freshwater flux c, with three different γ corresponding to $\Delta\widehat{T}_A = 10K$, $15K$, $20K$ respectively for fixed $\overline{\widehat{T}_A} = 291K$. We can see that c_{r2} decreases with γ. For warm equable climates, γ is smaller due to smaller $\Delta\widehat{T}_A$ or bigger $\overline{\widehat{T}_A}$, we will have smaller c_{r2}, so it will be easier to reach the oscillatory solutions in region III during warm equable climates.

3.2.2 What sets ε and the freshwater boundary separating stable / unstable steady HM?

In our OGCM, $\varepsilon \approx -1.1$ (Figure 2-11(b)). Given the bathymetry we used for late Permian ocean, salt is transported from the narrow Tethys sea into the deep ocean, making the mean deep ocean salinity much higher than normal. To conserve the total salinity, the mean surface polar salinity $\widehat{S}_{h\_gcm}$ has to be very low, around 28 PSU during the quasi-steady HM. In our 3-box model the typical value for $\widehat{S}_{h\_box}$ during the quasi-steady HM with similar parameters to the OGCM (i.e. $F = 0.65m/yr$, $\widehat{M} = 3.33 \times 10^{-5}\ m^2/s$) is much higher, about 30.8 PSU. As we discussed in chapter 2, $\varepsilon \approx (\widehat{\rho}_h - \widehat{\rho}_{eddy})/(\widehat{\rho}_0\alpha\Delta\widehat{T}_A)$, assuming $\widehat{\rho}_{eddy}$ and $\widehat{T}_h$ in the quasi-steady HM for both the OGCM and the 3-box model are similar, then

$$(\widehat{\rho}_{h\_gcm} - \widehat{\rho}_{h\_box})/(\widehat{\rho}_0\alpha\Delta\widehat{T}_A) \approx \beta(\widehat{S}_{h\_gcm} - \widehat{S}_{h\_box})/(\alpha\Delta\widehat{T}_A) \approx -0.7 \tag{3.26}$$

This gives us a rough estimation of the difference between ε in the OGCM and in the box model, thus we choose $\varepsilon = -0.4$ as a constant in our 3-box model for the first order approximation, in reality it might change with c, M_l, M_h etc. Substitute $\varepsilon = -0.4$ and other parameters into the relation $\Delta\rho_{hd} = \varepsilon$, i.e. Eq. (3.25), we can get the freshwater boundary separating stable and unstable steady HM. Figure 3-5 is the plot of $\Delta\rho_{hd}$ of the steady HM vs. the non-dimensional freshwater forcing c with other fixed parameters same as in Figure 3-2, we can see that $\Delta\rho_{hd} = -0.4$ corresponds to $c_{r3} \approx 0.0119$, i.e. a mean freshwater forcing $F \approx 1.19m/yr$, this is the freshwater boundary separating

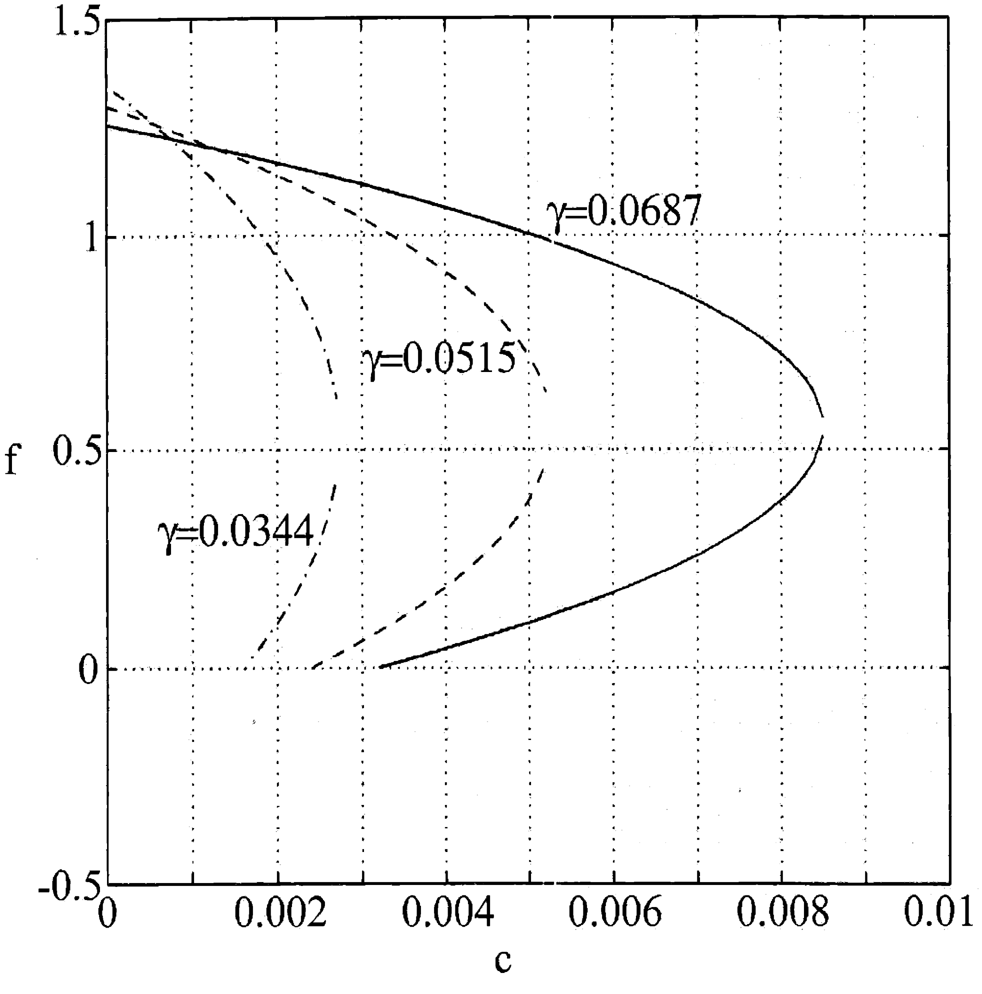

Figure 3-4: Bifurcation diagram on the f-c plane for different γ ($\gamma = \Delta\widehat{T}_A/\overline{\widehat{T}_A}$, $\overline{\widehat{T}_A} = 291K$), other parameters are same as in Figure 3-2.

region III and IV on the $f - c$ bifurcation diagram. When $c < c_{r3}$, we have $\Delta\rho_{hd} > \varepsilon$, thus the steady HM becomes unstable.

Similarly, we plot $\Delta\rho_{hd}$ of the steady HM vs. the non-dimensional background vertical diffusivity M (Figure 3-6) with other fixed parameters same as in Figure 3-3. We can see that $\Delta\rho_{hd} > -0.4$ for all M in this case, thus the steady HM is unstable for all M, there is no region IV on the $f - M$ bifurcation diagram for this case (Figure 3-3).

3.3 Time dependent solutions

Now we will discuss the time dependent solutions of the 3-box model solved numerically. The Eq. (3.13-3.18) are integrated numerically by Runge-Kutta method, convective adjustment are employed for each time step. By choosing $c = 0.0065$ ($F = 0.65m/yr$), $M = 0.0025$ ($\widehat{M} = 3.3 \times 10^{-5} m^2/s$), similar to what we used in the OGCM and other fixed parameters same as in Figure 3-2, the system is within the window on the f-c plane where the oscillation is possible. We obtained the oscillatory solution with a period of about 3000 years. The initial condition is $\Delta T = 0$, $\overline{T} = 1$, $T_d = 1$, $\Delta S = 0$, $\overline{S} = 1$, $S_d = 1$.

Figure 3-7, 3-8 shows the time series of temperature $\widehat{T}_i$, salinity $\widehat{S}_i$ (i=l,h,d) in each box of this oscillatory solution, and non-dimensional vertical density difference between the surface box and deep ocean box $\Delta\rho_i$ ($i = ld, hd$) respectively. Comparing the 3-box model result (Figure 3-7, 3-8) with the OGCM result (Figure 2-10, 2-11), we can see that they are very similar. Figure 3-9(a) shows the time series of the non-dimensional overturning circulation f of the 3-box model, the system stays for a long time in the quasi-steady HM ($f \approx -0.35$, i.e. $q \approx -7.35Sv$), then it suddenly jumps to the transient TM ($f \approx 0.75$, i.e. $q \approx 15.75Sv$) and quickly returns to the HM again. In the 3-box model, the strength of the transient TM is much smaller than that in the OGCM, that is because the simple assumption (Eq. 3.1) we used here. A more sophisticated parameterization of the overturning strength might improve this. Figure 3-9(b) shows

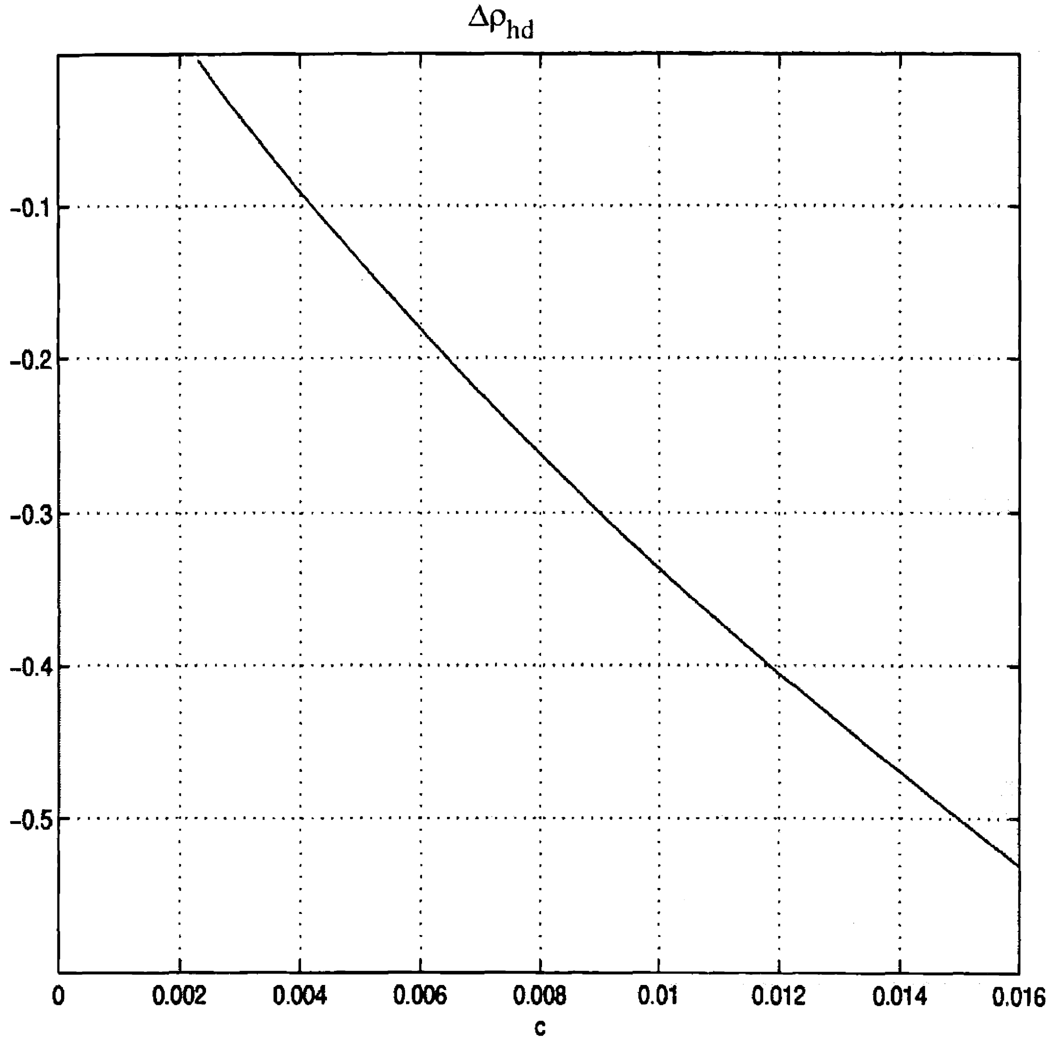

Figure 3-5: Non-dimensional density difference $\Delta\rho_{hd}$ vs. freshwater flux.

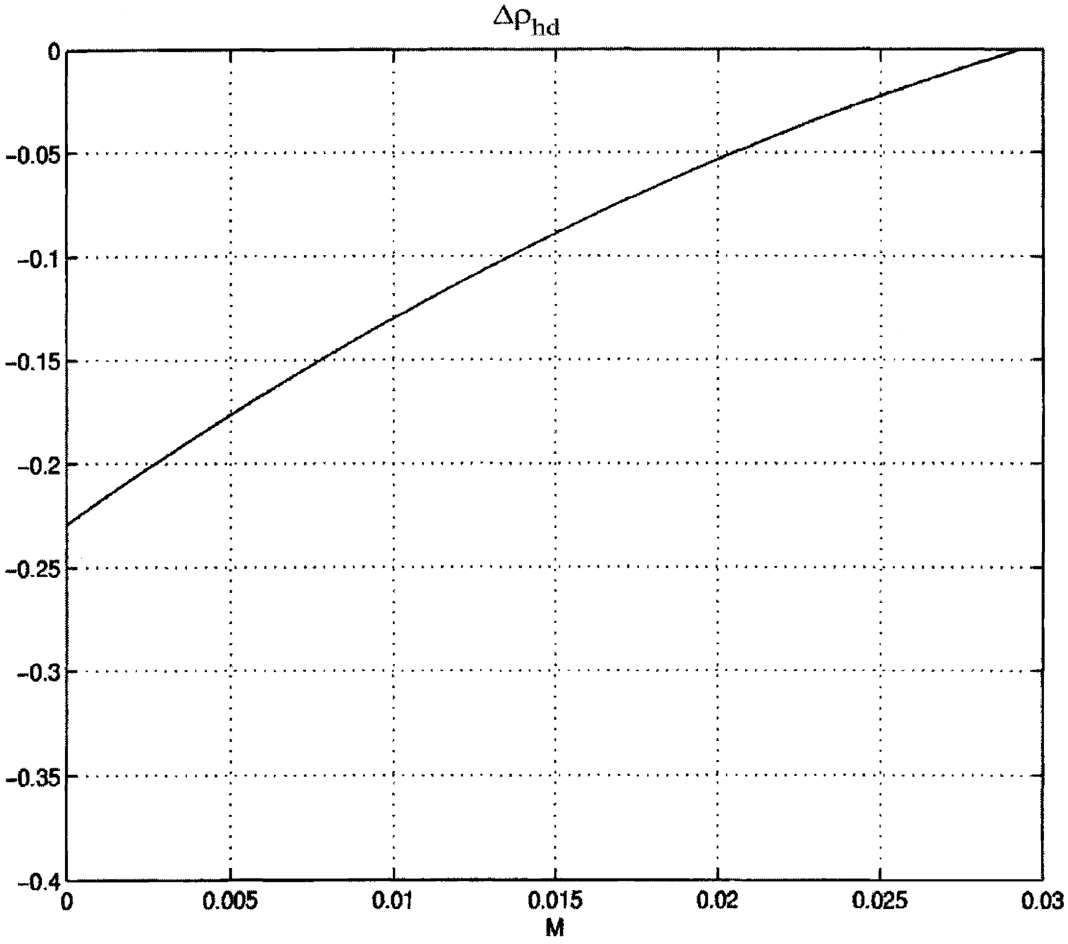

Figure 3-6: Non-dimensional density difference $\Delta\rho_{hd}$ vs. background vertical diffusivity.

the time series of the total surface air-sea heatflux of the 3-box model, which is very similar what has been found in the OGCM (Figure 2-7(b)). Figure 3-10 is the projection of the phase portrait of the limit cycle onto the $\widehat{T}_d - \widehat{S}_d$ plane for the OGCM result and the 3-box model result respectively, both of them exhibit a loop with two fast branches (the onset and the termination of polar convection) and two slow branches.

In the 3-box model, there are small noisy oscillations during the transient TM before the termination of polar convection (Figure 3-7 to 3-9), this is due to convection in low latitude: when $\Delta\rho_{ld} \geq \eta_l$, convection happens in low latitude, the convective mixing $M_l = M_{wc}$ gradually makes $\Delta\rho_{ld} < \eta_l$, then the convection stops there ($M_l = M$). The surface freshwater forcing will soon make $\Delta\rho_{ld} \geq \eta_l$ again, convection ($M_l = M_{wc}$) resumes there. These short, weak oscillations are similar to the heat-salt oscillator in Welander's convection model (Welander, 1982), but does not affect the existence of the longer period large amplitude oscillations induced by the polar convection. In the 3-box model, $\eta_l = -0.05, \eta_h = 0.02$, they are not zero exactly to avoid small numerical false oscillations when M_l is discontinuous during the transient TM. In our OGCM (Figure 2-11(a)), we always have $\Delta\rho_{ld} < \eta_l$ due to higher deep ocean salinity, we will not see such kind of short small oscillations.

By decreasing c from $c_{r2} = 0.0047$ and test different initial conditions, we found that when $c \leq 0.0043$, the final solution will always stay in the stable steady TM no matter what the initial conditions. When $c > 0.0043$, both stable steady TM and oscillatory solutions are possible depending on initial conditions, so $c_{r1} \approx 0.0043$. Similarly we can get $M_{r2} \approx 0.0209$ by testing different initial conditions numerically.

3.4 Relationship of oscillation periods with freshwater flux / vertical diffusivities

If we vary c in region II, III on the f-c plane and choose right initial conditions when in region II, we can study the relation of oscillation periods with the amplitude of freshwater

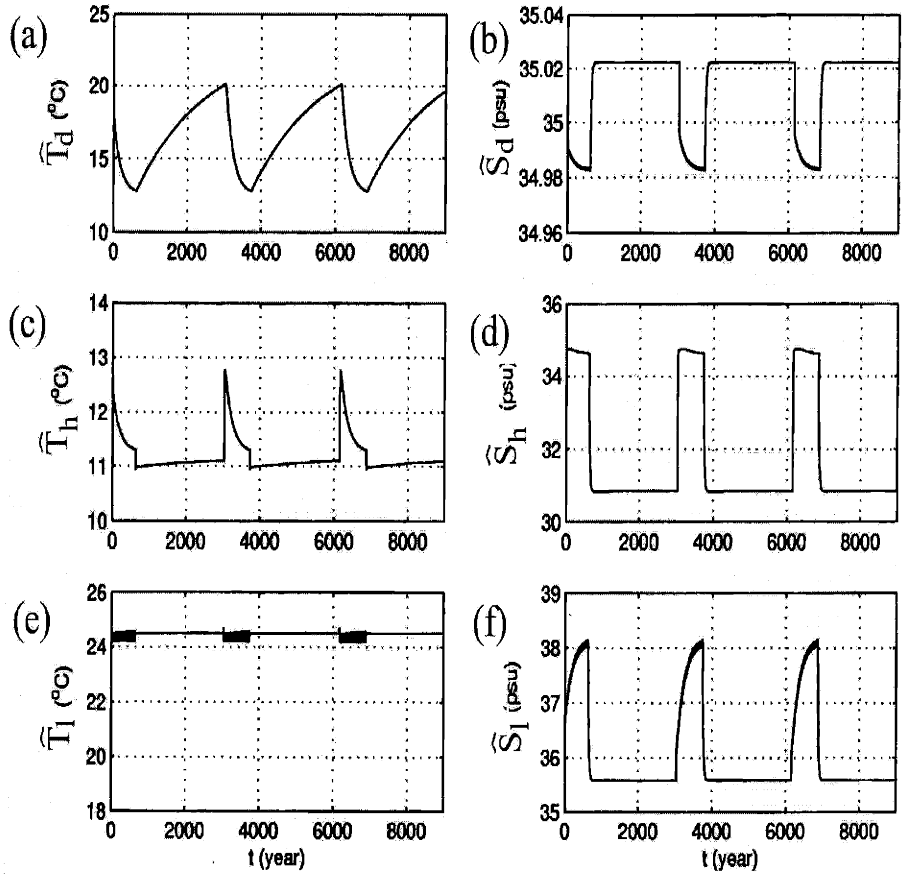

Figure 3-7: Time series of temperature and salinity in each box of the 3-box model. (a) $\widehat{T}_d$,(b) $\widehat{S}_d$, (c) $\widehat{T}_h$,(d) $\widehat{S}_h$, (e) $\widehat{T}_l$, (f) $\widehat{S}_l$.

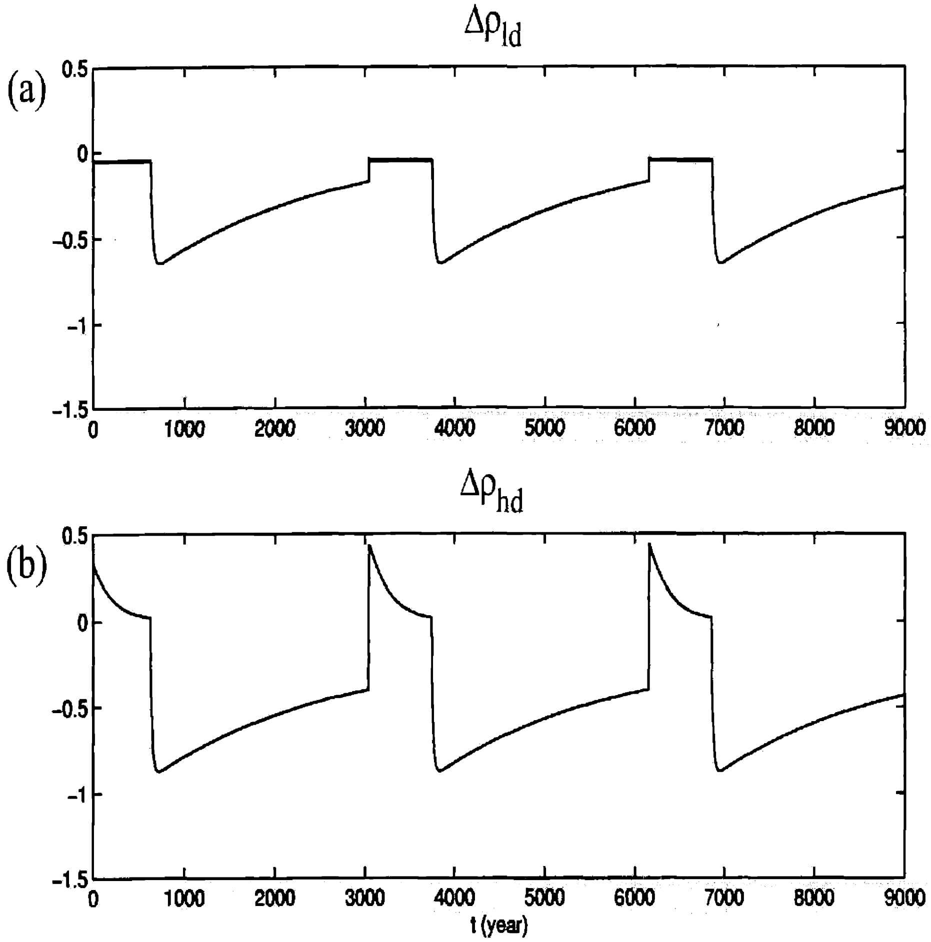

Figure 3-8: Time series of surface and deep ocean non-dimensional density difference of the 3-box model. (a) $\Delta\rho_{ld}$, (b) $\Delta\rho_{hd}$.

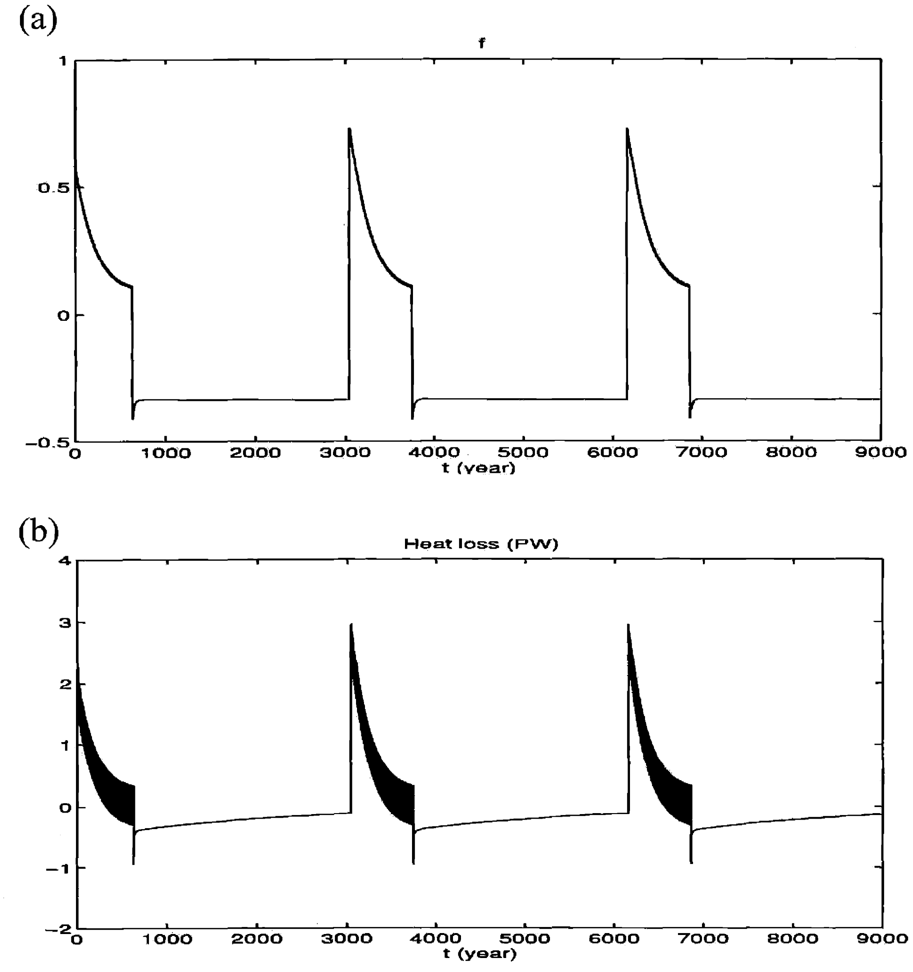

Figure 3-9: (a)Time series of the non-dimensional overturning circulation of the 3-box model. (b)Time series of the total surface air-sea heatflux of the 3-box model.

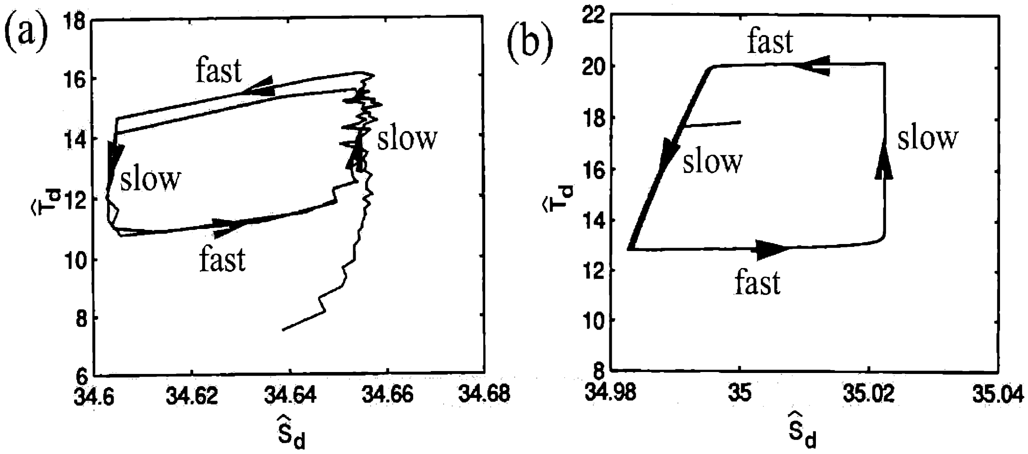

Figure 3-10: Projection of the phase portrait of the limit cycle on $\widehat{T_d}$-$\widehat{S_d}$ plane. (a) OGCM, (b) 3-box model.

flux. Figure 3-11 shows the total oscillation period - T_{os} (line with circles), period of the quasi-steady HM - T_{HM} (line with dot) and period of the transient TM - T_{TM} (line with star) during one cycle of the oscillation as a function of c in the oscillatory window of the f-c plane, other parameters are same as in Figure 3-2. We can see that the mean trend of T_{TM} increases slightly as c increases, T_{os} is dominated by T_{HM} and changes with it. When c is small, T_{HM} decreases as c increases, because in such case the overturning strength $|f|$ is small, T_{HM} is dominated by the advection time scales which is inversely proportional to $|f|$, as $|f|$ increases with c, T_{HM} decreases. When c is large, T_{HM} increases as c increases, although the overturning strength $|f|$ still increases with c, $\widehat{T_l} - \widehat{T_d}$ decreases when c increases, then the effect of advection on the deep ocean temperature is weaker. It takes much longer time for the deep ocean to reach higher temperature just before polar convection starts, so T_{HM} increases with c.

If we vary M in region II, III on the f-M plane and choose the appropriate initial conditions when in region II, we can also study the relation of oscillation periods with the background vertical diffusivity. Figure 3-12 shows T_{os} (line with circles), T_{HM} (line with dot) and T_{TM} (line with star) as a function of M in the oscillatory window of the f-M plane, other parameters are same as in Figure 3-3. T_{TM} decreases slightly with M and T_{os} changes with T_{HM}. We can see that T_{HM} always decreases as M increases, because the larger M is, the faster the deep ocean temperature increases due to vertical diffusion during the HM, the earlier the polar convection starts.

3.5 Summary

The 3-box model with convective adjustment and parameterization of localized convection effect, catches the essential physical mechanism of the thermohaline oscillations found in many OGCMs. It also explains why the HM circulation is unstable for certain range of freshwater forcing / vertical mixing. With the $f - c$, $f - M$ bifurcation diagrams, we can understand how the oscillatory solutions are related to other steady state solutions. The polar convection during the flushing event can occur with negative $\Delta\rho_{hd}$ due to localized static instability, thus the nonlinear equation of state for seawater density is not necessary to obtain oscillatory solutions.

The HM in the 3-box model corresponds to the indirect haline cell in the OGCM result, we ignore the tropical region which is not very important to the oscillation mechanism. The representation of the deep ocean with a single box is based on the assumption that during the TM, cold and fresh water sinking from polar surface will spread into lower latitude horizontally; during the HM, warm and salty water sinking from subtropical surface will spread horizontally to the region below polar surface.

The numerically integrated oscillatory solutions of the 3-box model show very similar properties of what has been found in the OGCM (chapter 2), confirm the bifurcation diagram obtained from analysis of the steady state solutions. The box model serves as an efficient tool to explore the whole parameter space, such as the relationship between oscillation periods and the freshwater forcing/vertical diffusivity, though simple analytical expression for the oscillation period as a function of the freshwater forcing/vertical

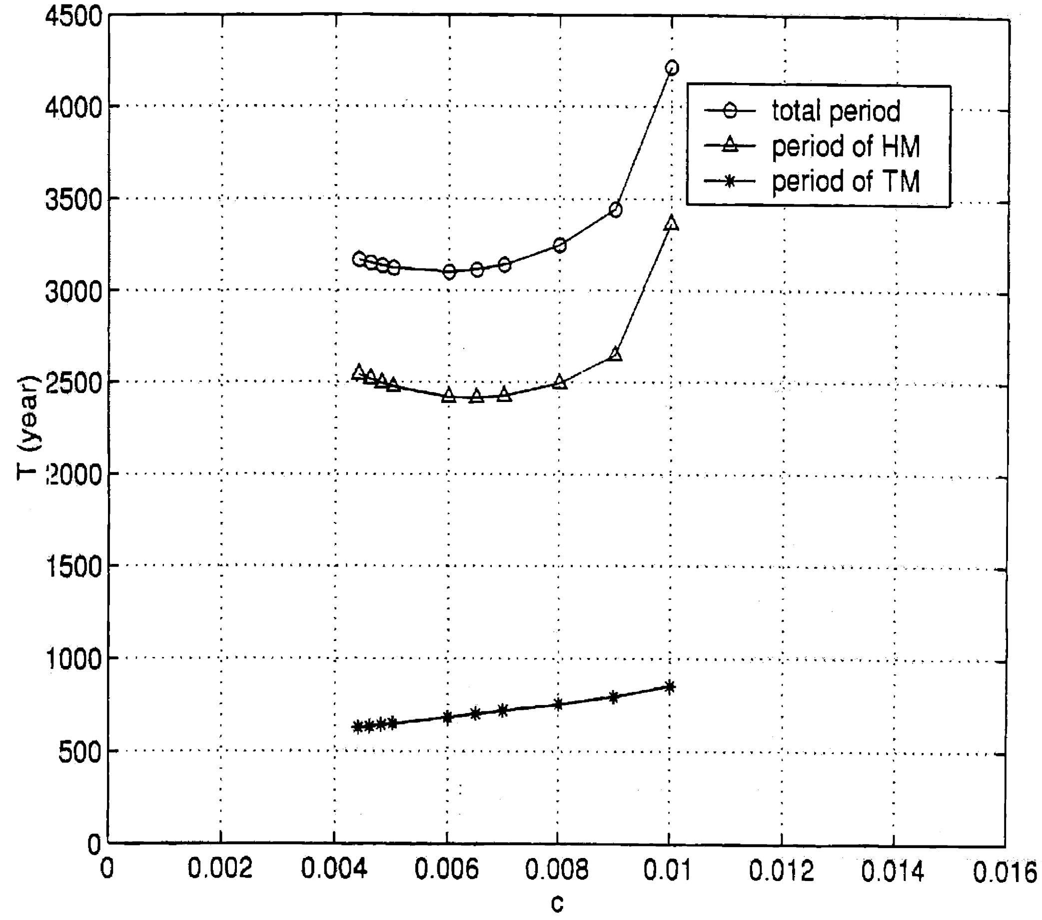

Figure 3-11: Oscillation periods as a function of freshwater forcing c. The total oscillation period (line with circles), the period of HM during one cycle of the oscillation (line with dot) and the period of TM during one cycle of the oscillation (line with star).

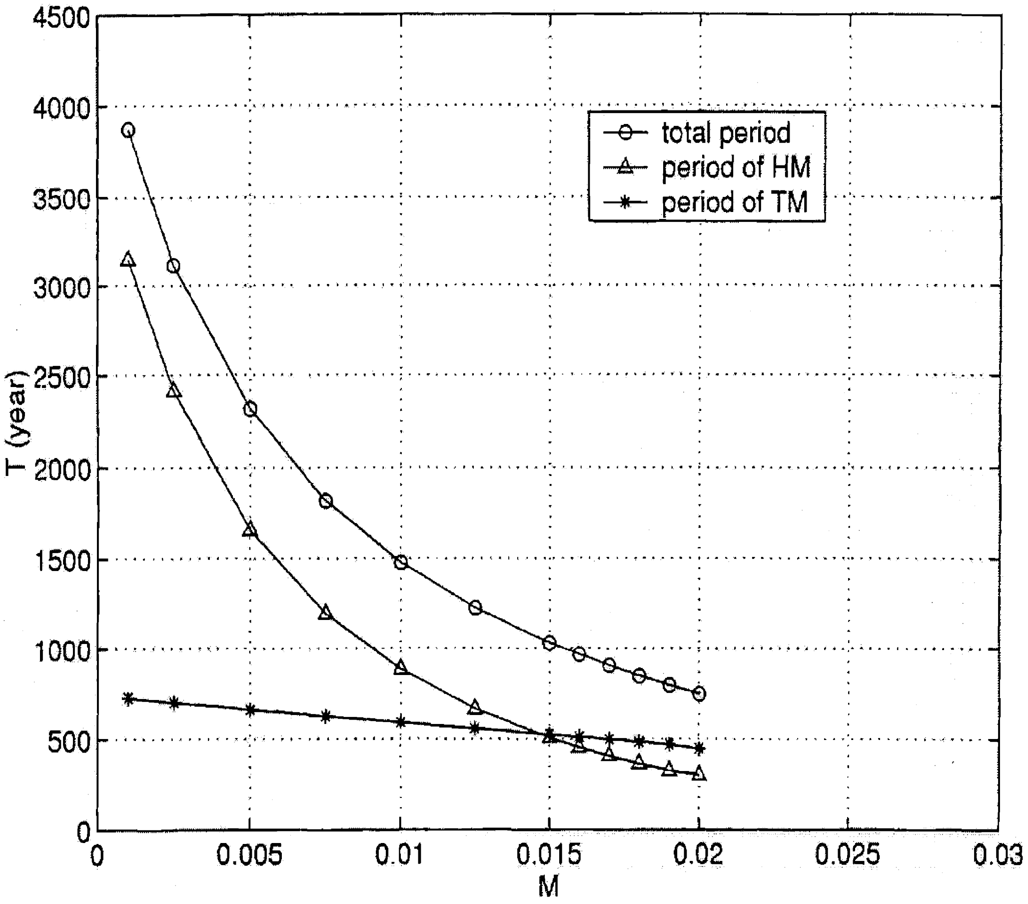

Figure 3-12: Oscillation periods as a function of background vertical diffusivity M. The total oscillation period (line with circles), the period of HM during one cycle of the oscillation (line with dot) and the period of TM during one cycle of the oscillation (line with star).

diffusivity deserves further investigation.

Today's ocean circulation is in a stable TM, but we do not know how far away we are from the bifurcation point. The critical freshwater forcing c_{r2}, corresponding to the bifurcation point on the $f - c$ plane, decreases with the pole-equator surface air temperature gradient. Thus in warm and equable climates, it is easier to reach c_{r2}, beyond which no TM exists, the thermohaline oscillation is more likely to happen.

Unfortunately the resolution of most geological records for the warm paleoclimates can not resolve centuries-millennial timescales, so even such thermohaline oscillations might have existed in paleo oceans, it would be very hard to find the right oscillation frequency from paleo records. For example, we obtained the time series of the same thermohaline oscillation solution as showed in Figure 3-7 for 1.6 Million years, then sampled it every 4 Kyrs (high resolution in paleo sediments sampling). Since the actual oscillation probably has a period of less than 4 Kyrs, the time series is undersampled (Figure 3-13(a)). We calculated the power spectrum of the undersampled time series of deep ocean temperature (Figure 3-13(b)), now the largest peak on the power spectrum corresponds to a cycle with a period of about 14 Kyrs, the actual oscillation frequency has been aliased to a lower frequency significantly due to undersampling.

The thermohaline oscillations on centuries-millennial timescales will have significant impact on the biogeochemical cycle, we will study the interaction between the thermohaline circulation and the biogeochemical cycle with the box model in chapter 4.

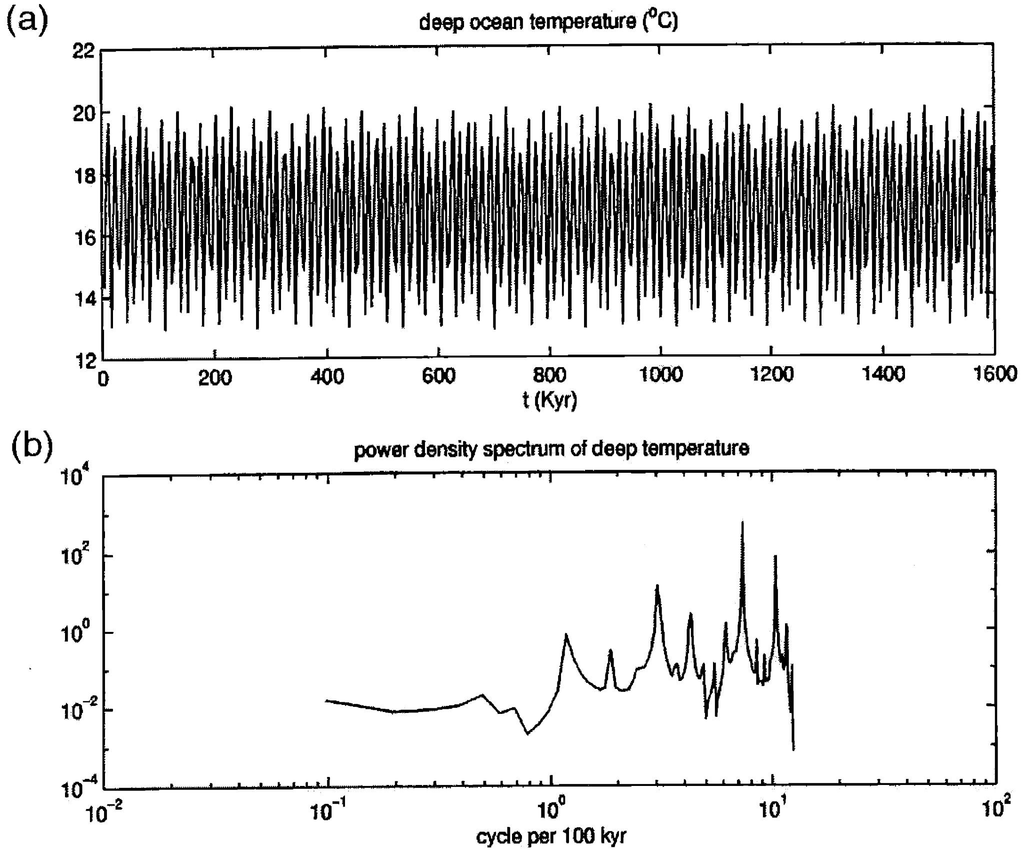

Figure 3-13: Undersampled deep ocean temperature and its power spectral. (a) Time series of deep ocean temperature of the oscillating solution with 4kyr sample interval. (b) power spectral with loglog plot.

Chapter 4

Biogeochemical cycle studied with the 3-box model

4.1 Steady solutions of biogeochemical cycle and its implication for deep-sea anoxia

4.1.1 Model description

We employ a simple 3-box model of ocean phosphorous and oxygen cycling to examine the interplay of circulation and biogeochemistry and seek to understand the criteria under which deep oceanic anoxia may be possible.

The model is depicted schematically in Figure 4-1, with boxes representing the low and high latitude euphotic zone, and a third box representing the deep ocean. P_l, P_h and P_d are the phosphorous concentrations in each box. O_l^*, O_h^* are the surface equilibrium oxygen concentration with respect to local atmospheric partial pressure of oxygen and the temperature and salinity dependent solubility (Weiss, 1970). O_d is the oxygen concentration of the abyss. B_l, B_h are the organic matter export rates from boxes of the euphotic zone respectively. Tracers are advected by the meridional overturning circulation, ψ, and experience deep, convective mixing at high latitudes, parameterized by

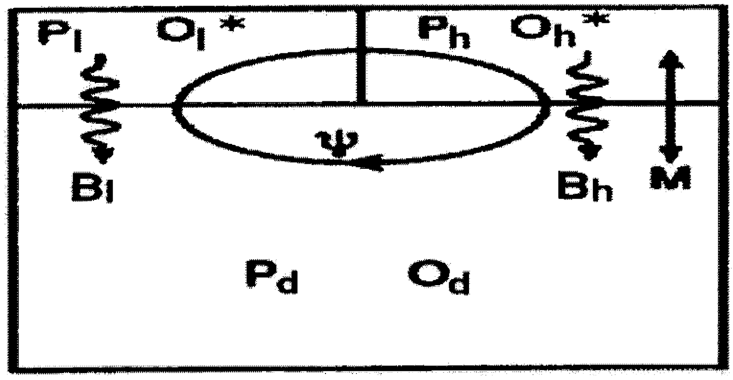

Figure 4-1: Schematic diagram of the 3-box model. P_l, P_h and P_d are the phosphorous concentrations in each box. O_l^*, O_h^* are the surface equilibrium oxygen concentration. O_d is the oxygen concentration of the abyss. B_l, B_h are the organic matter export rates from boxes of the euphotic zone respectively. ψ is the thermohaline transport rate, M is the convective mixing rate.

mixing coefficient, M. The model somewhat resembles previous studies (e.g. Sarmiento et al., 1988) but with some significant differences. One important aspect of the box model is that the particulate export of phosphorous is parameterized with the same nutrient and light limiting function as used in the three-dimensional experiments discussed later.

We assume that the global ocean phosphorus burden is constant and, assuming volume and nutrient conservation for each box, derive governing equations for phosphorus in the surface boxes, determined by advection, convective mixing and the particulate export of organic matter:

$$V_l \frac{dP_l}{dt} = \psi P_d - \psi P_l - V_l B_l \tag{4.1}$$

$$V_h \frac{dP_h}{dt} = \psi P_l - \psi P_h + \frac{A_h M}{h}(P_d - P_h) - V_h B_h \tag{4.2}$$

Here V_l, V_h, V_d are the volumes of the boxes of the low latitude euphotic zone, high latitude euphotic zone and deep ocean respectively, A_h is the surface area of the high latitude surface box, and h is the convective mixing depth in the high latitude region.

The sinking particulate export of nutrients, B, is limited by light and nutrients thus:

$$B = \frac{\Phi\varepsilon_o}{h_e}\frac{P}{P+P_c}. \tag{4.3}$$

Here P is the total phosphorous concentration of the surface euphotic zone. $\frac{\Phi\varepsilon_o}{h_e}$ is the vertical divergence of the flux of short wave solar radiation, Φ, in the euphotic layer with thickness h_e, scaled by the 'light utilization efficiency', ε_o(Parsons, 1988). Light limitation is enforced by assuming the flux divergence of short wave solar radiation provides an extreme *upper bound* on the rate of new and export production (i.e. the rate of new and export production may not exceed that of primary production). Nutrient limitation of export is enforced by $\frac{P}{P+P_c}$. Here P_c is the nutrient concentration at which *particulate export* becomes light limited (not to be confused with a half-saturation coefficient for primary production). Hence

$$P_c = \frac{\Phi\varepsilon_o}{h_e\lambda_p} \tag{4.4}$$

where λ_p is a global rate constant which characterizes the ocean wide efficiency of biological flushing of nutrients from the euphotic zone. $1/\lambda_p$ represents the typical residence time of a phosphorus atom in the euphotic zone with respect to export on a biogenic particle. When $P \ll P_c$, particulate export is proportional to the local phosphorous concentration, ensuring nutrient limitation at low phosphorous concentrations. When $P \gg P_c$, export is proportional to the incident flux of short wave solar radiation, $\Phi(y,t)$, a function of latitude and season. We use this parameterization of particulate export of nutrients both in the box model and in the three-dimensional model experiments discussed later. For the box model, in the high latitude surface box, $B_h = \lambda_{ph}\frac{P_hP_c}{(P_h+P_c)}$. For the low latitude surface box we assume that light is never limiting and hence $B_l = \lambda_{pl}P_l$,.

A statement of conservation of total ocean phosphorus, in conjunction with (4.1) and (4.2), completes the description of the box model phosphorus cycle.

In general, surface oxygen concentrations are observed to be close to local equilibrium with respect to the atmosphere, due to the rapid air-sea equilibration timescales for the mixed-layer (Wanninkhof, 1992). Hence, in this box model, we make the simplifying assumption that the surface oxygen concentrations are set to the equilibrium values; $O_l = O_l^*$ and $O_h = O_h^*$, as determined from local temperature, salinity and atmospheric partial pressure of O_2 (Weiss, 1970). Oxygen concentration in the deep ocean box O_d is determined by advection, high latitude mixing and remineralization of particles below the euphotic zone:

$$V_d \frac{dO_d}{dt} = \psi O_h^* - \psi O_d - \frac{A_h M}{h}(O_d - O_h^*) + R_{op}(V_l B_l + V_h B_h) \tag{4.5}$$

Oxygen is consumed during remineralization below the euphotic zone according to the Redfield stoichiometry, where R_{op} is Redfield ratio of $O : P$ (Takahashi *et al.*, 1985).

4.1.2 Steady state solutions and discussion

Solving (4.1)–(4.5) for steady state ($\frac{d}{dt} = 0$) with the assumption $P_d \approx P_0$ reveals

$$P_l = \frac{\psi P_0}{\psi + \lambda_{pl} V_l} \tag{4.6}$$

$$P_h = \frac{1}{2(\frac{A_h M}{h} + \psi)}(S + (S^2 + 4P_c P_0(\frac{A_h M}{h} + \frac{\psi^2}{\psi + \lambda_{pl} V_l})(\frac{A_h M}{h} + \psi))^{\frac{1}{2}}) \tag{4.7}$$

and

$$S = P_0(\frac{A_h M}{h} + \frac{\psi^2}{\psi + \lambda_{pl} V_l}) - (1 + \lambda_{ph} V_h + \frac{A_h M}{h})P_c \tag{4.8}$$

$$O_d = O_h^* + R_{op} P_0 f^*(\psi, M, P_0) = O_h^* + R_{op}(P_0 - P_h) \tag{4.9}$$

$f^*(\psi, M, P_0)$ is a function of the ocean transport characteristics (ψ, M) and the global mean concentration of phosphorus in the ocean, P_0. The deep ocean oxygen is set through ventilation by oxygen rich waters from the high-latitude surface (first term on right of

Table 4.1: Steady state biogeochemical box model parameters of modern ocean.

Variable	Value
A_h (High latitude surface area)	$8.75 \times 10^{13} m^2$
h_e (Euphotic layer depth)	100 m
h (Convective mixing depth)	2000 m
V_l (Low latitude euphotic zone volume)	$8.75 \times 10^{15} m^3$
V_h (High latitude euphotic zone volume)	$8.75 \times 10^{15} m^3$
λ_{pl} (Low latitude organic matter export rate)	$\frac{1}{30 months}$
λ_{ph} (High latitude organic matter export rate)	$\frac{1}{30 months}$
P_0 (Mean ocean phosphorus concentration)	2.07 $\mu mol/kg$
P_c (Light-limited phosphorus concentration)	0.9 $\mu mol/kg$
R (Redfield ratio of O:P)	-175
O_h^* (High latitude surface equilibrium oxygen concentration)	7.5 ml/l

Eq. (4.9)) and reduced by remineralisation of the flux of biogenic particles (second term on right of Eq. (4.9)).

The dependence of deep ocean oxygen concentration and high latitude surface phosphorous concentration on ocean transport parameters, for this model, is shown in Figure 4-2. Several notable inferences can be drawn from the model: (i) increasing thermohaline overturning rate *increases* oxygenation of the deep waters in most parameter ranges (Figure 4-2(a), variable values for the modern ocean are listed in Table -1), (ii) increased phosphorous loading of the ocean *reduces* deep ocean oxygen concentrations; and (iii), decreased equilibrium oxygen concentration of sinking surface waters leads to *decreased* deep ocean oxygen concentrations. The high latitude surface phosphorous distribution, P_h (Figure 4-2(b)), has similar pattern to the oxygen, except that they are inversely proportional to each other as indicated by Eq. (4.9).

Here a criterion of 1 ml/l is chosen below which we assert that the deep ocean oxygen is significantly depleted in dissolved oxygen (not necessarily anoxic) relative to the modern deep ocean, which typically has about $4ml/l$ of dissolved oxygen.

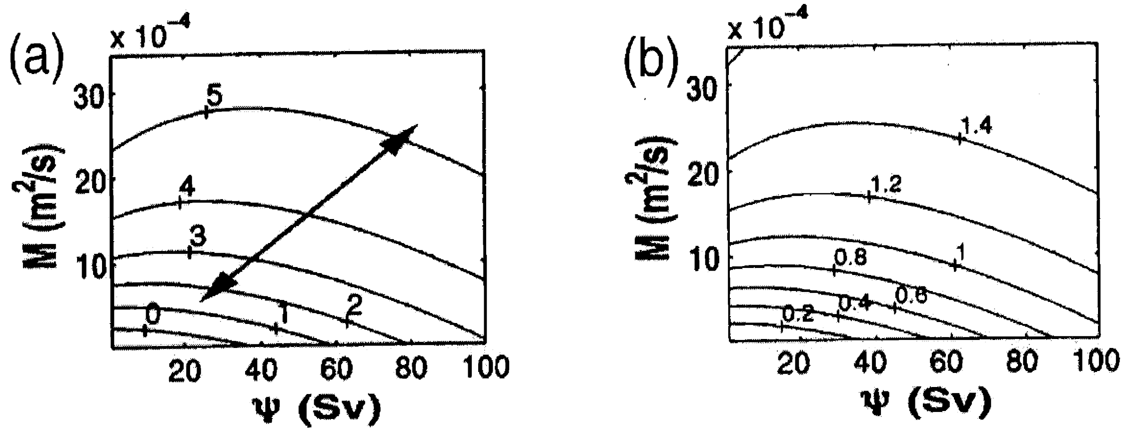

Figure 4-2: (a) O_d (ml/l), (b) P_h (μmol/kg) in the (M/ψ) plane for parameter ranges encompassing those of the modern ocean. The oxygen concentration generally decreases if thermohaline circulation rate and/or convective mixing rate decreases. Mixing and overturning rates are not independent, indicated here by the sloping, schematic trajectory.

4.1.3 Limit case

The box model result is qualitatively different from that of Sarmiento et al. (1988), who found that increasing thermohaline overturning rate *decreased* oxygenation of the deep ocean in a somewhat similar box model. The value of M in our model can be directly compared with the value of F$_{hd}$ in Sarmiento et al. (1988) using the linear relation: $F_{hd} = \frac{A_h M}{h}$. How can we reconcile the different result? Sarmiento *et al.* (1988) chose to specify the organic particle flux in the downwelling branch and assumed that surface nutrients in the upwelling branch are completely utilized and instantly exported as particles. This turns out to be a limit case of the model described above, where $\lambda_{pl} \to \infty$ and $P_h \gg P_{c}$,. In this limit, the solution of our model for P_h is:

$$P_h = \frac{P_0 \frac{A_h M}{h} - \lambda_{ph} V_h P_c}{\frac{A_h M}{h} + \psi}. \tag{4.10}$$

This is indeed consistent with equation (8) of Sarmiento et al. (1988), where $\lambda_{ph} V_h P_c$ is analogous to their prescribed particle flux at high latitudes. For comparison, we

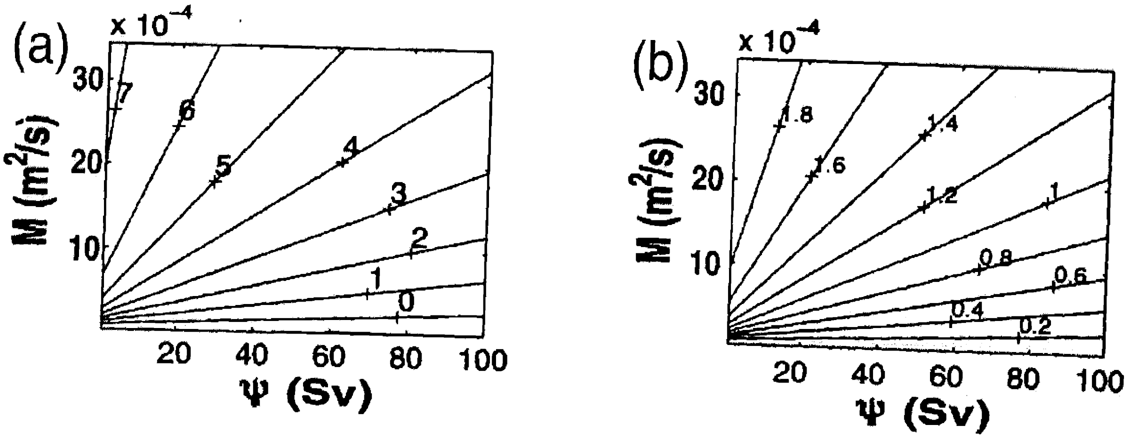

Figure 4-3: (a) O_d (ml/l), (b) P_h (μmol/kg) in the (M/ψ) plane for the limit case $\lambda_l \to \infty$, and $P_h \gg P_c$.

illustrate this case in Figure 4-3(a) which shows similar trends to Figure 4 in Sarmiento et al. (1988), where $\frac{\partial O3}{\partial \psi} < 0$, over all of M, ψ space. Stronger thermohaline overturning supplies more nutrient to the surface in the upwelling branch, stronger particle export, so leading to deep-sea oxygen depletion. The high latitude surface phosphorous distribution (Figure 4-3(b)) also gives $\frac{\partial P_h}{\partial \psi} > 0$ over all of M, ψ space, since it is inversely proportional to oxygen distribution as indicated by Eq. (4.9). However, this limit represents a very special case. More generally, we find $\frac{\partial O3}{\partial \psi} > 0$, over much of M, ψ space.

We have chosen to use the same nutrient and light limited parameterization of export production in this box model as is used in the three-dimensional experiments reported later. The three-dimensional experiments demand such a representation to allow the biogeochemistry to respond appropriately when the ocean bathymetry and climate are significantly modified and we cannot usefully impose particle flux distributions in the three-dimensional experiments. We recognize, however, the simplicity of our parameterization which omits other, possibly important, limiting nutrients. We will demonstrate that our export parameterization reproduces the broad features of the modern ocean oxygen distribution in a three dimensional model (chapter 5) and that the box model using this scheme successfully predicts the sensitivity of deep ocean oxygen in the 3-d model to changes in thermohaline overturning discussed in chapter 2.

4.2 Time dependent solutions of biogeochemical cycle (phosphorous, oxygen, P_{CO_2}, δ^{13}C) driven by oscillatory thermohaline circulation

4.2.1 Model description

To study the change in biogeochemical cycles, such as shift of $\delta^{13}C$, during the mode switch of thermohaline circulation, we add biogeochemical cycle into the 3-box model of thermohaline circulation. By numerical integration, we solve the time dependent solutions, driven by the thermohaline oscillations, for phosphorous (P), alkalinity (AIK), oxygen (O), DIC^{12}, and DIC^{13} in each box (l, h, d). We use C^{13}, C^{12} to represent dissolved inorganic carbon (DIC^{12}, DIC^{13}) :

$$DIC = [CO_2] + [HCO_3{}^{-}] + [CO_3{}^{2-}].$$

The $\delta^{13}C$ is defined as

$$\delta^{13}C = (\frac{\gamma}{\gamma_{STD}} - 1) \times 1000 \ \ per\ mil, \tag{4.11}$$

where γ is the ratio of carbon isotopes in the model, γ_{STD} is the standard ratio of carbon isotopes. For example,

$$\gamma_{DIC} = \frac{C^{13}}{C^{12}}$$

is the ratio of carbon isotopes of DIC. Figure 4-4 is a schematic diagram of the model. Here we assume that the total carbon in the ocean and atmosphere is conserved (i.e. closed system), the atmospheric CO_2 partial pressure $P_{CO_2}^{atm}$ is calculated by subtracting

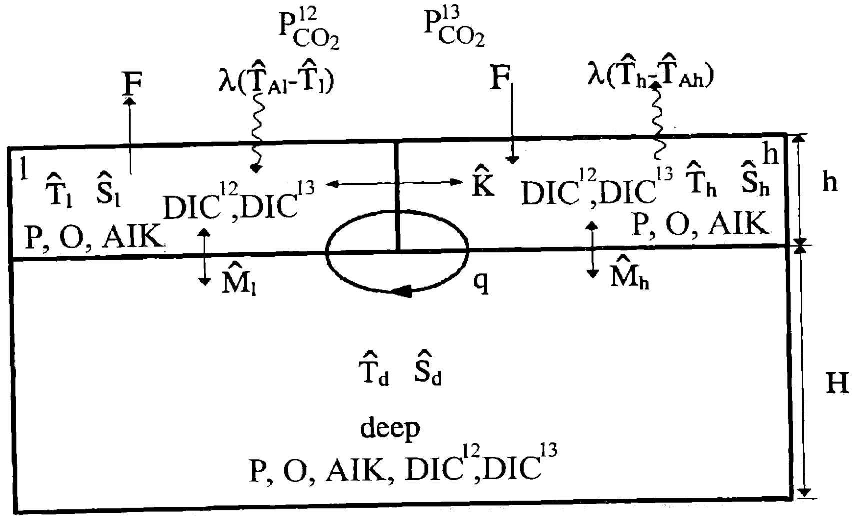

Figure 4-4: Schematic diagram of the biogeochemical cycle driven by oscillatory thermohaline circulation in the 3-box model.

the carbon in the ocean from the total carbon in the ocean and atmosphere.

We can write down the dynamic equations for the biogeochemical cycle driven by either TM ($f > 0$) or HM ($f < 0$) ocean circulation. Although all biogeochemical variables in the equations are dimensional, the thermohaline circulation fields are non-dimensional as discussed in chapter 3.

For example, the dynamic equations for DIC^{12} are:

$$\begin{aligned}\frac{dC_l^{12}}{dt'} &= \overbrace{\frac{f\gamma}{2}(C_d^{12}-C_h^{12})+\frac{|f|\ \gamma}{2}(C_d^{12}+C_h^{12}-2C_l^{12})}^{\text{advection}}+\overbrace{\frac{c}{4}(C_l^{12}+C_h^{12})}^{\text{freshwater forcing}} \\ &\quad -\underbrace{R_{cp}B_l}_{\text{bio pump}}+\underbrace{\frac{V_PK_{0l}}{\lambda h}(P^{atm}_{CO_2}-P^{ol}_{CO_2})}_{\text{air-sea flux}}+\underbrace{\frac{1}{2}K(C_h^{12}-C_l^{12})+M_l(C_d^{12}-C_l^{12})}_{\text{diffusion}} \qquad (4.12)\end{aligned}$$

$$\begin{aligned}\frac{dC_h^{12}}{dt'} &= \overbrace{\frac{f\gamma}{2}(C_l^{12}-C_d^{12})+\frac{|f|\ \gamma}{2}(C_d^{12}+C_l^{12}-2C_h^{12})}^{\text{advection}}-\overbrace{\frac{c}{4}(C_l^{12}+C_h^{12})}^{\text{freshwater forcing}} \\ &\quad -\underbrace{R_{cp}B_h}_{\text{bio pump}}+\underbrace{\frac{V_PK_{0h}}{\lambda h}(P_{CO_2}^{atm}-P_{CO_2}^{oh})}_{\text{air-sea flux}}+\underbrace{\frac{1}{2}K(C_l^{12}-C_h^{12})+M_h(C_d^{12}-C_h^{12})}_{\text{diffusion}}\end{aligned} \tag{4.13}$$

$$\begin{aligned}\frac{dC_d^{12}}{dt'} &= \frac{\delta}{2}(\overbrace{\frac{f\gamma}{2}(C_h^{12}-C_l^{12})+\frac{|f|\ \gamma}{2}(C_h^{12}+C_l^{12}-2C_d^{12})}^{\text{advection}} \\ &\quad +\underbrace{R_{cp}(B_l+B_h))}_{\text{bio pump}}+\underbrace{M_l(C_l^{12}-C_d^{12})+M_h(C_h^{12}-C_d^{12})}_{\text{diffusion}}\end{aligned} \tag{4.14}$$

The equations include terms such as advection, diffusion, biological pump, air-sea flux and freshwater forcing (dilute effect). Here R_{cp} is the redfield ratio of carbon to phosphorous, B_l, B_h represent the surface productivity at low and high latitudes:

$$B_l = \frac{\lambda_P}{\lambda}\frac{P_l}{1+P_l/P_{cl}}, \quad B_h = \frac{\lambda_P}{\lambda}\frac{P_h}{1+P_h/P_{ch}}, \tag{4.15}$$

λ_P is the organic matter export rate, P_{cl}, P_{ch} are the light-limited nutrient concentration in low and high latitude, as discussed in section 4.1. V_P is the piston velocity for surface CO_2 exchange, K_{0l}, K_{0h} is the solubility of CO_2 in surface ocean at low- and high-latitude, determined by the sea surface temperature (SST) and salinity (SSS) (Weiss, 1974). $P_{CO_2}^{ol}, P_{CO_2}^{oh}$ are the dissolved CO_2 partial pressure in the surface ocean at low and high latitude, they are calculated by the following relation with surface DIC (Stumm and Morgan, 1996):

$$P^o_{CO_2} = \frac{C^{12}}{(1 + \frac{K_1}{[H^+]} + \frac{K_1 K_2}{[H^+]^2})K_0}, \tag{4.16}$$

Here $K_1 = \frac{[H^+][HCO_3^-]}{[CO_2]}, K_2 = \frac{[H^+][CO_3^{2-}]}{[HCO_3^-]}$ are the equilibrium constants for inorganic carbon determined by SST and SSS (Diskson and Millero, 1987). The hydrogen ion concentration, $[H^+]$, is solved numerically by the fifth order polynomial in $[H^+]$ (Follows et al., 1996), given alkalinity, DIC, ΣB (dissolved inorganic boron concentration), K_1, K_2, K_w (equilibrium constants for water) and K_b (equilibrium constants for boron). The alkalinity (AIK) is discussed later, ΣB and K_w are set to be constants in Table 4.2, K_b is determined by SST and SSS (Takahashi et al., 1981).

The dynamic equations for DIC^{13} have similar advection, diffusion and freshwater forcing term, but the biological pump and air-sea exchange term are more complicated:

$$\begin{aligned}\frac{dC_l^{13}}{dt'} &= \frac{f\gamma(C_d^{13} - C_h^{13}) + |f|\ \gamma(C_d^{13} + C_h^{13} - 2C_l^{13})}{2} \\ &+ \frac{K(C_h^{13} - C_l^{13})}{2} + M_l(C_d^{13} - C_l^{13}) - \alpha_{org}\ \gamma_{DIC_l}\ R_{cp}B_l \\ &+ \frac{\alpha_{KF}V_P(\gamma_{atm}\ \alpha_{sl}P_{CO_2}^{atm} - \gamma_{DIC_l}\ \alpha_{cl}P_{CO_2}^{ol})}{\lambda h} + \frac{c(C_l^{13} + C_h^{13})}{4}\end{aligned} \tag{4.17}$$

$$\begin{aligned}\frac{dC_h^{13}}{dt'} &= \frac{f\gamma(C_l^{13} - C_d^{13}) + |f|\ \gamma(C_d^{13} + C_l^{13} - 2C_h^{13})}{2} \\ &+ \frac{K(C_l^{13} - C_h^{13})}{2} + M_h(C_d^{13} - C_h^{13}) - \alpha_{org}\gamma_{DIC_h}R_{cp}B_h \\ &+ \frac{\alpha_{KF}V_P(\gamma_{atm}\alpha_{sh}P_{CO_2}^{atm} - \gamma_{DIC_h}\alpha_{ch}P_{CO_2}^{oh})}{\lambda h} - \frac{c(C_l^{13} + C_h^{13})}{4}\end{aligned} \tag{4.18}$$

$$\begin{aligned}\frac{dC_d^{13}}{dt'} &= \frac{\delta}{2}(\frac{f\gamma(C_h^{13} - C_l^{13})}{2} + \frac{|f|\ \gamma(C_h^{13} + C_l^{13} - 2C_d^{13})}{2} + M_l(C_l^{13} - C_d^{13}) \\ &+ M_h(C_h^{13} - C_d^{13}) + \alpha_{org}\ R_{cp}(\gamma_{DIC_l}B_l + \gamma_{DIC_h}B_h))\end{aligned} \tag{4.19}$$

Here α_{org} is the biological fractionation factor for ^{13}C, α_{KF} is the kinetic fractionation factor. α_{sl}, α_{sh} are the temperature dependent equilibrium solubility fractionation factors in low and high latitude respectively, determined by SST (Mook, 1986):

$$\alpha_{si} = -\frac{0.373}{\widehat{T}_i} + 1.00019, \ i = l, h \tag{4.20}$$

α_{cl}, α_{ch} are the temperature dependent equilibrium fractionation factors for $CO_2(aq)$ to HCO_3^- in low and high latitude respectively, determined by SST (Mook, 1986):

$$\alpha_{ci} = -\frac{9.866}{\widehat{T}_i} + 1.02412, \ i = l, h \tag{4.21}$$

So the equilibrium fractionation factors will always increase with surface temperature. In Eq. (4.17-4.18), γ_{atm} is the ratio of carbon isotopes in the atmosphere.

The dynamic equations for alkalinity (AIK) are:

$$\begin{aligned}\frac{dAIK_l}{dt'} &= \frac{f\gamma}{2}(AIK_d - AIK_h) + \frac{|f|\ \gamma}{2}(AIK_d + AIK_h - 2AIK_l) \\ &+\frac{1}{2}K(AIK_h - AIK_l) + M_l(AIK_d - AIK_l) - \frac{1}{3}R_{cp}B_l + \frac{c}{4}(AIK_l + AIK_h)\end{aligned} \tag{4.22}$$

$$\begin{aligned}\frac{dAIK_h}{dt'} &= \frac{f\gamma}{2}(AIK_l - AIK_d) + \frac{|f|\ \gamma}{2}(AIK_d + AIK_l - 2AIK_h) \\ &+\frac{1}{2}K(AIK_l - AIK_h) + M_h(AIK_d - AIK_h) - \frac{1}{3}R_{cp}B_h - \frac{c}{4}(AIK_l + AIK_h)\end{aligned} \tag{4.23}$$

$$\begin{aligned}\frac{dAIK_d}{dt'} &= \frac{\delta}{2}(\frac{f\gamma}{2}(AIK_h - AIK_l) + \frac{|f|\ \gamma}{2}(AIK_h + AIK_l - 2AIK_d) \\ &+M_l(AIK_l - AIK_d) + M_h(AIK_h - AIK_d) + \frac{1}{3}R_{cp}(B_l + B_h))\end{aligned} \tag{4.24}$$

The factor $\frac{1}{3}$ in front of the biological pump term is because we assume that the ratio of the formation of skeletal $CaCO_3$ to organic carbon export is $\frac{1}{6}$ (Anderson and Sarmiento, 1994); the skeletal $CaCO_3$ is dissolved completely; and the rate of change for alkalinity is twice of that for dissolved $CaCO_3$ (Broecker and Peng, 1993). Alkalinity is used to solve for pH, i.e. $[H^+]$, with the fifth order polynomial in $[H^+]$ (Follows et al., 1996).

The dynamic equations for phosphorous (P) are:

$$\begin{aligned} \frac{dP_l}{dt'} &= \frac{f\gamma}{2}(P_d - P_h) + \frac{|f|\ \gamma}{2}(P_d + P_h - 2P_l) + \frac{1}{2}K(P_h - P_l) \\ &\quad + M_l(P_d - P_l) - B_l + \frac{c}{4}(P_l + P_h) \end{aligned} \tag{4.25}$$

$$\begin{aligned} \frac{dP_h}{dt'} &= \frac{f\gamma}{2}(P_l - P_d) + \frac{|f|\ \gamma}{2}(P_d + P_l - 2P_h) + \frac{1}{2}K(P_l - P_h) \\ &\quad + M_h(P_d - P_h) - B_h - \frac{c}{4}(P_l + P_h) \end{aligned} \tag{4.26}$$

$$\begin{aligned} \frac{dP_d}{dt'} &= \frac{\delta}{2}(\frac{f\gamma}{2}(P_h - P_l) + \frac{|f|\ \gamma}{2}(P_h + P_l - 2P_d) + M_l(P_l - P_d) \\ &\quad + M_h(P_h - P_d) + (B_l + B_h)) \end{aligned} \tag{4.27}$$

The dynamic equation for deep ocean oxygen (O) is:

$$\begin{aligned} \frac{dO_d}{dt'} &= \frac{\delta}{2}(\frac{f\gamma}{2}(O_h^* - O_l^*) + \frac{|f|\ \gamma}{2}(O_h^* + O_l^* - 2O_d) + M_l(O_l^* - O_d) \\ &\quad + M_h(O_h^* - O_d) + R_{op}(B_l + B_h)) \end{aligned} \tag{4.28}$$

Here O_l^*, O_h^* are the low and high latitude surface equilibrium oxygen concentrations

Table 4.2: Constants for the time-dependent biogeochemical box model.

Constant	Value
γ_{STD} (Standard ratio of carbon isotopes)	0.0112373
P_{cl} (Low latitude light-limited nutrient)	2.7668 9 ($\mu mol/kg$)
P_{ch} (High latitude light-limited nutrient)	1.543 ($\mu mol/kg$)
R_{cp} (Redfield ratio of $C : P$)	106
R_{op} (Redfield ratio of $O : P$)	-175
V_p (Piston velocity of CO_2 exchange)	3 (m/day)
α_{org} (Biological fractionation factor)	0.977
α_{KF} (Kinetic fractionation factor)	0.997
ΣB (Dissolved inorganic boron)	409 $\mu mol/kg$
K_w (Equilibrium constants for water)	6.463×10^{-15}

respectively, determined by SST, SSS and atmospheric partial pressure of O_2 (Weiss, 1970). At surface, the air-sea oxygen exchange is very strong, the oxygen concentration is always close to the equilibrium value, so we assume the surface oxygen concentration in each box equals O_h^*, O_l^* respectively.

The fixed constants of the biogeochemical model are listed in Table 4.2. We integrated the model numerically with the initial conditions listed in Table 4.3. The initial P_{CO_2} is set as modern value in 1973 (Toggerweiler and Sarmiento, 1985), then 1.1×10^{16} mol carbon^{12} is subtracted from the total carbon^{12} in the atmosphere to account for fossil fuel emissions (Broecker and Peng, 1982). The initial carbon^{13} in the ocean and atmosphere is calculated based on $\delta^{13}C$, and the fossil fuel emissions is subtracted from the atmospheric carbon^{13} with -26 per mil fossil fuel $\delta^{13}C$. The initial condition for temperature, salinity is same as that in Chapter 3.

4.2.2 Solutions and discussion

Figure (4-5 to 4-10) shows the time dependent solutions of phosphorous, oxygen, DIC^{12}, $DIC^{13}, \delta^{13}C$ and alkalinity in each box. During the quasi-steady HM, the surface phosphorous is very low, giving lower mean surface biological productivity $\overline{B} = (B_l + B_h)/2$

Table 4.3: Initial conditions for the time-dependent biogeochemical box model.

Variable	Value
C_l^{12}	1932 ($\mu mol/kg$)
C_h^{12}	2139 ($\mu mol/kg$)
C_d^{12}	2230 ($\mu mol/kg$)
$\delta^{13}C_l$	2.64 (per mil)
$\delta^{13}C_h$	1.72 (per mil)
$\delta^{13}C_d$	0.66 (per mil)
$\delta^{13}C_{atm}$	-6.18 (per mil)
AIK_l	2376.32 (ueq/kg)
AIK_h	2376.32 (ueq/kg)
AIK_d	2376.32 (ueq/kg)
P_l	2.07 ($\mu mol/kg$)
P_h	2.07 ($\mu mol/kg$)
P_d	2.07 ($\mu mol/kg$)
O_d	200 ($\mu mol/kg$)
$P_{CO_2}^{atm}$	320 (ppm)

(Figure 4-11 (b)). The deep ocean oxygen keeps decreasing until it reaches the anoxic condition, the surface $\delta^{13}C$ becomes heavier ($\sim$ 3 per mil), $\delta^{13}C_{atm}$ also becomes heavier (-6 per mil, Figure 4-11(a)). $P_{CO_2}^{atm}$ decreases gradually for $\sim$ 50 ppm (Figure 4-12(a)), corresponding to the slight increase in C_d^{12} (Figure 4-7(c)).

During the transient TM, the surface phosphorous is much higher, gives higher mean surface biological productivity $\overline{B}$ (Figure 4-11 (b)). The deep ocean oxygen increases quickly, the surface $\delta^{13}C$ becomes lighter ($\sim$ 1.9 per mil in low latitude, $\sim$ 1.4 per mil in high latitude), $\delta^{13}C_{atm}$ also becomes lighter (-7.2 per mil, Figure 4-11(a)). $P_{CO_2}^{atm}$ increases quickly for $\sim$ 50 ppm (Figure4-12(a)), corresponds to the decrease in C_d^{12} (Figure 4-7(c)).

Figure 4-12(b) shows the outgassing of CO_2 from low latitude surface, i.e. $P_{CO_2}^{ol} - P_{CO_2}^{atm}$. Figure 4-12(c) shows the ingassing of CO_2 from high latitude surface, i.e. $P_{CO_2}^{atm} - P_{CO_2}^{oh}$. No matter which circulation mode, CO_2 is always released from low latitude surface ocean into the atmosphere, the outgassing is strongest during the switch from the quasi-steady HM into the transient TM. CO_2 is uptaken by the high latitude surface ocean from the atmosphere for most of the time, the ingassing is strongest during the switch from the transient TM into the quasi-steady HM. However, CO_2 is also released from the high latitude surface ocean into the atmosphere during the switch from the quasi-steady HM into the transient TM.

During the mode switch, the shift in high latitude surface $\delta^{13}C$ is about 1.6 per mil, the shift in low latitude surface $\delta^{13}C$ is about 1.1 per mil, the average is about 1.35 per mil. The correlation is consistent with the paleo record in Mid-Cretaceous (Figure 1-2, 1-3): anoxic deep ocean, lower surface productivity and heavier surface $\delta^{13}C$ are associated with the quasi-steady HM; oxygenated deep ocean, higher surface productivity and lighter surface $\delta^{13}C$ are associated with the transient TM. Comparing to the surface variations, the deep ocean concentration of C_d^{12} , C_d^{13}, $\delta^{13}C_d$, P_d and AIK_d do not change much with the mode switch, owing to the huge deep ocean reservoir.

To understand those correlations, we assume that the system is in quasi-steady state for most of the time, except the short period of mode switch. The numerical results are indeed consistent with this assumption. For example, the total tendency of C_d^{12} and C_h^{12}, i.e. $\frac{dC_d^{12}}{dt'}$ (Figure 4-13(a)) and $\frac{dC_h^{12}}{dt'}$ (Figure 4-13(b)) are almost zero in the quasi-steady HM and transient TM, except the extreme short interval of mode switch. Thus, assuming the deep ocean is in quasi-steady state, we get four balanced equations:

$$\frac{dP_d}{dt'} \approx 0 \rightarrow advection + diffusion + 2\overline{B} \approx 0 \tag{4.29}$$

$$\frac{dO_d}{dt'} \approx 0 \rightarrow advection + diffusion + R_{op} \cdot 2\overline{B} \approx 0 \tag{4.30}$$

$$\frac{dC_d^{12}}{dt'} \approx 0 \rightarrow advection + diffusion + R_{cp} \cdot 2\overline{B} \approx 0 \tag{4.31}$$

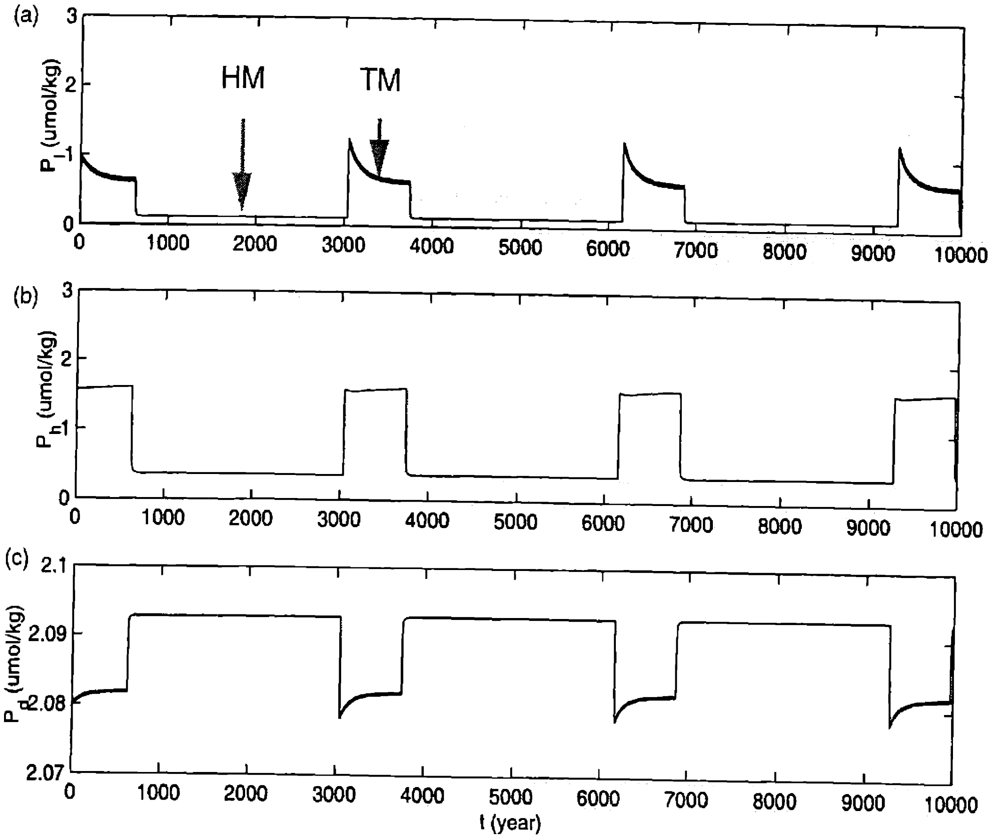

Figure 4-5: Time series of phosphorous ($\mu mol/kg$) with modern P_0. (a) low latitude surface, (b) high latitude surface, (c) deep ocean.

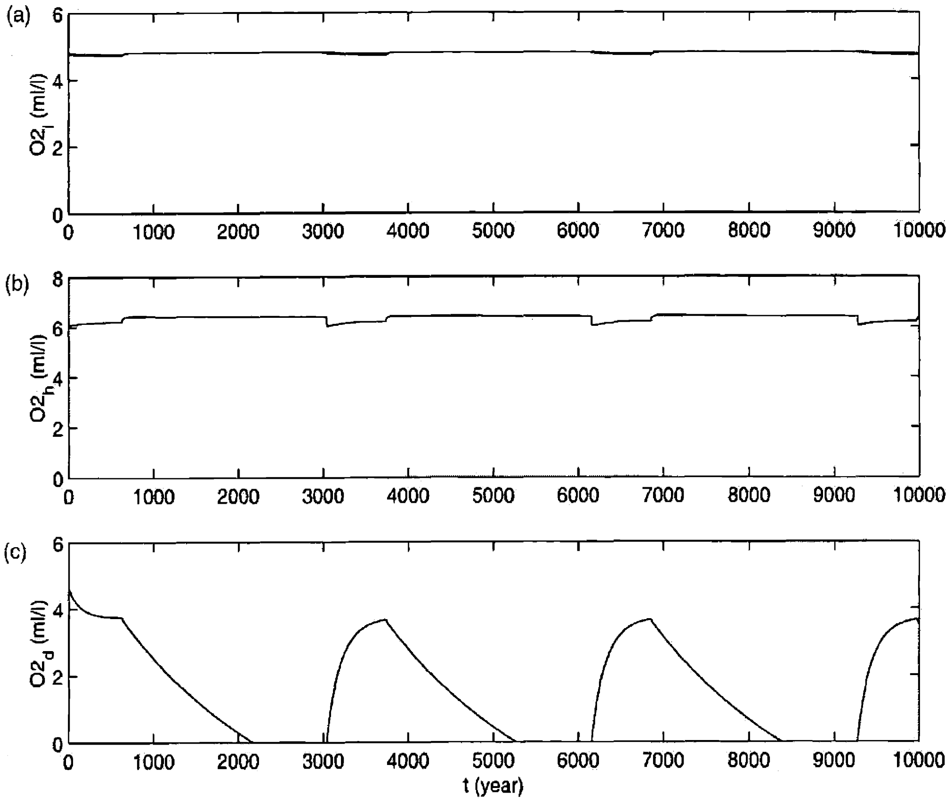

Figure 4-6: Time series of oxygen (ml/l) with modern P_0. (a) low latitude surface, (b) high latitude surface, (c) deep ocean.

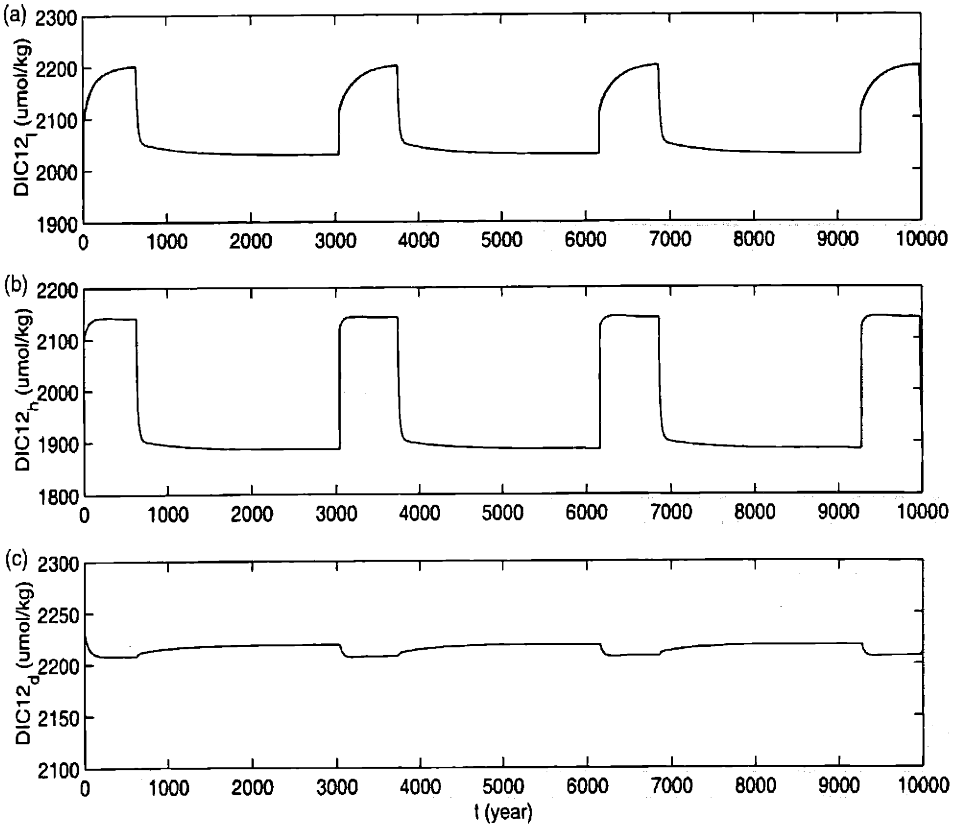

Figure 4-7: Time series of DIC^{12} ($\mu mol/kg$) with modern P_0. (a) low latitude surface, (b) high latitude surface, (c) deep ocean.

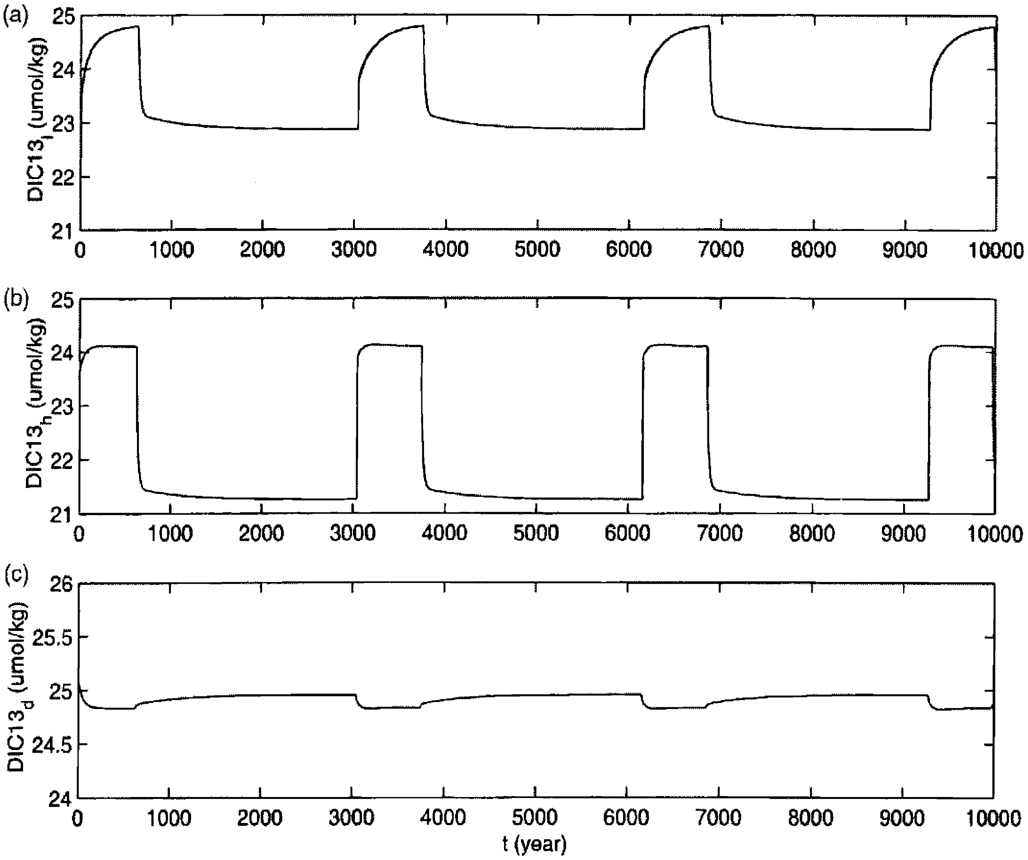

Figure 4-8: Time series of DIC^{13} ($\mu mol/kg$) with modern P_0. (a) low latitude surface, (b) high latitude surface, (c) deep ocean.

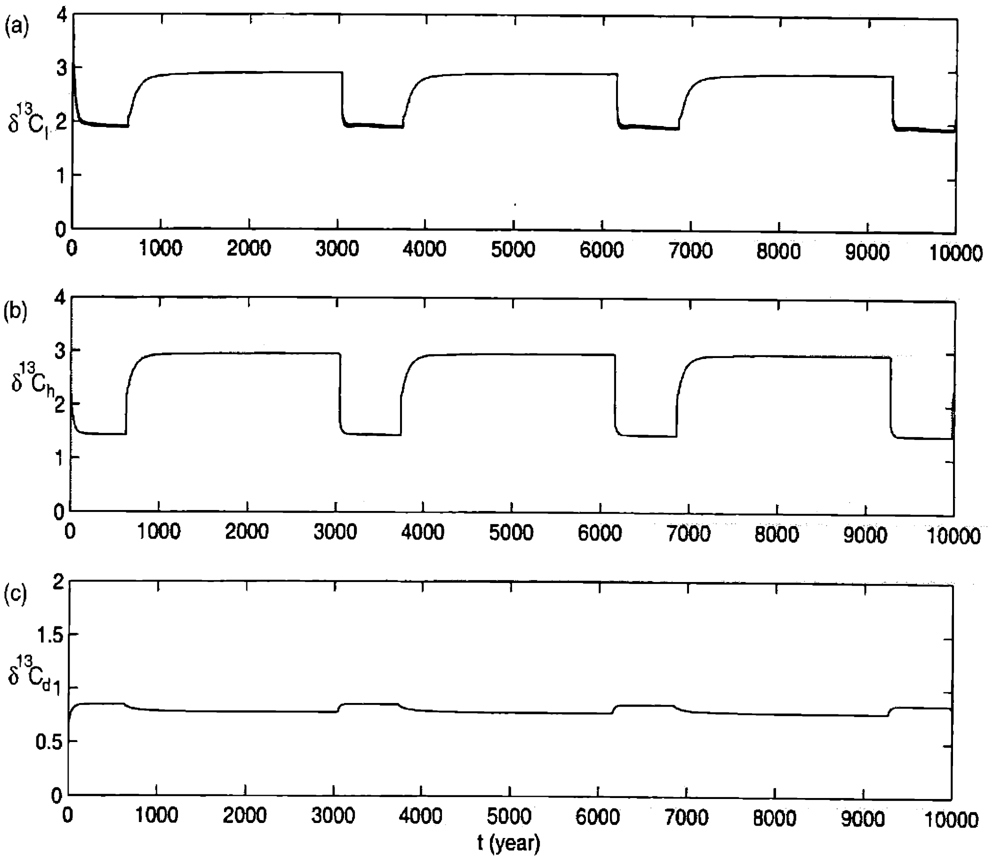

Figure 4-9: Time series of $\delta^{13}C$ (per mil) in low latitude surface (a), high latitude surface (b), deep ocean (c), with modern P_0.

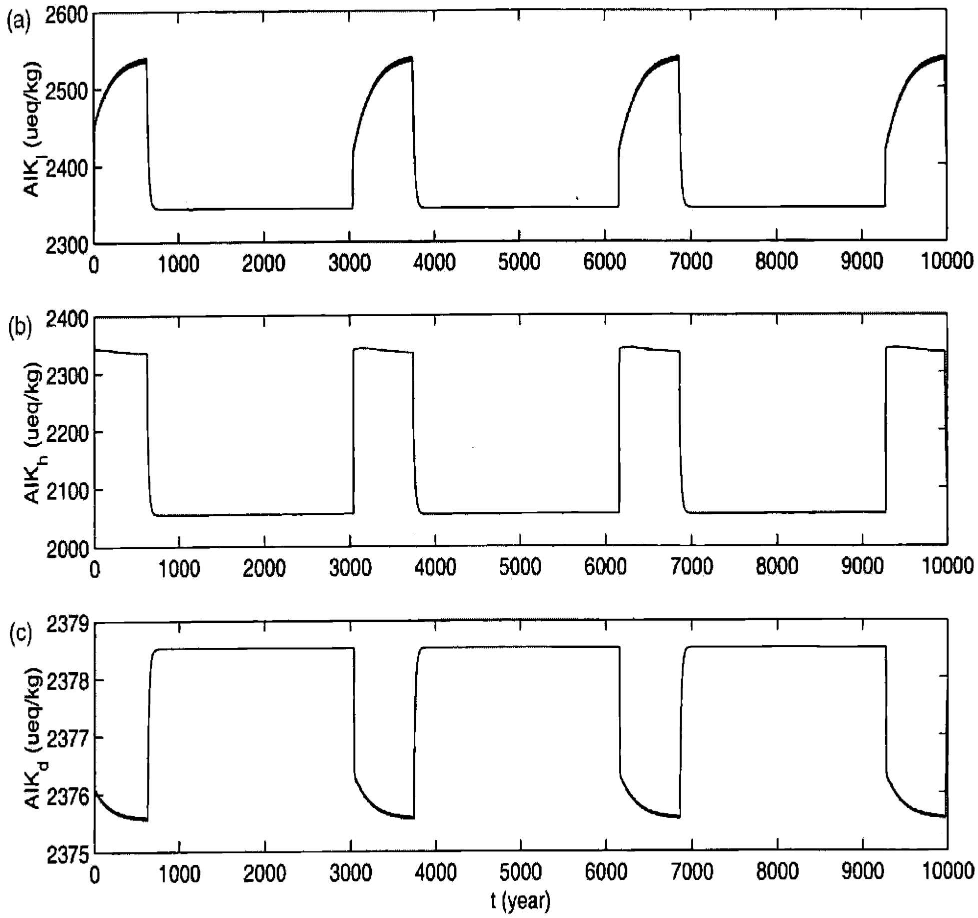

Figure 4-10: Time series of alkalinity in low latitude surface (a), high latitude surface (b), deep ocean (c), with modern P_0.

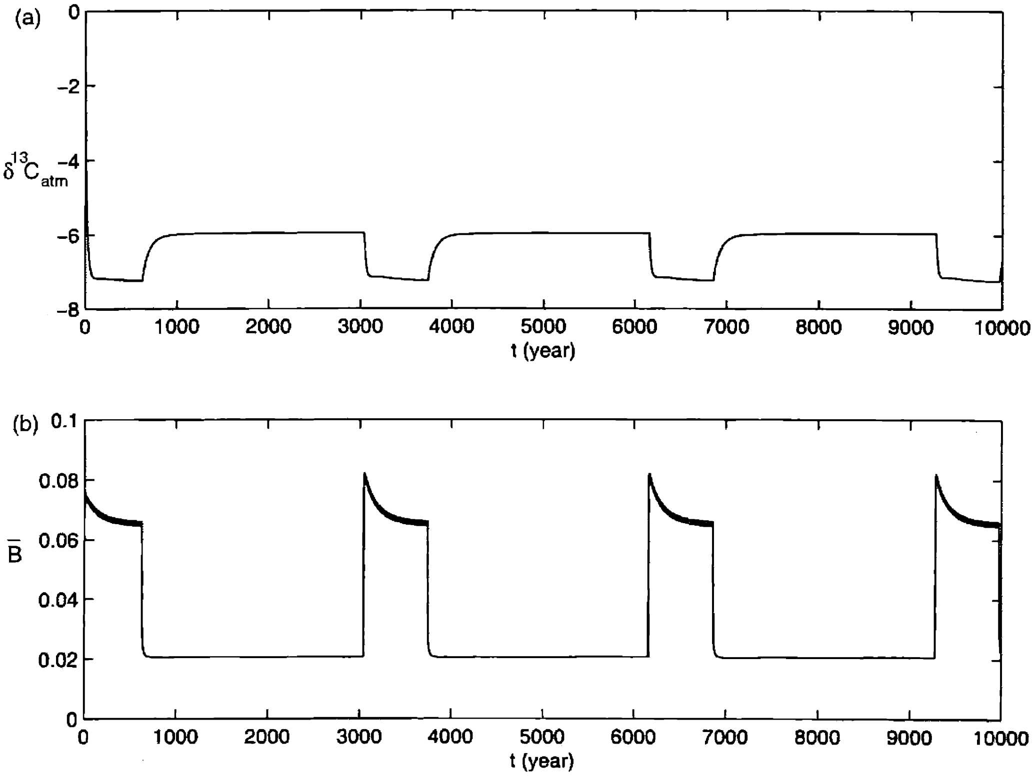

Figure 4-11: Time series of (a) atmospheric $\delta^{13}C, (b)$ mean surface productivity, with modern P_0.

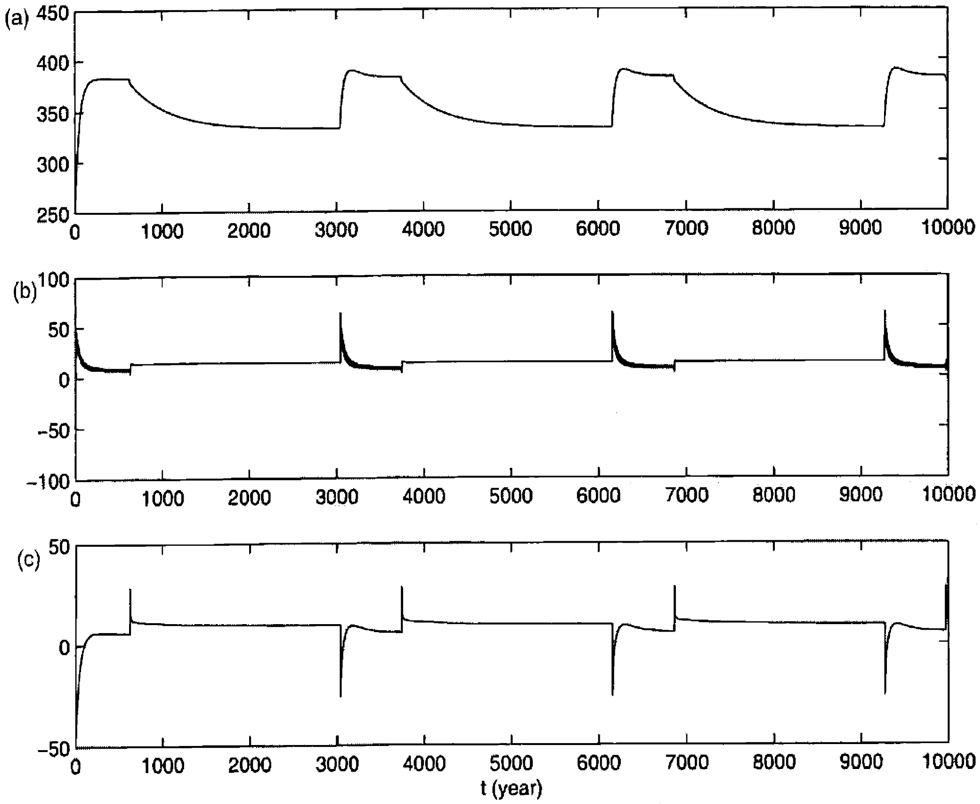

Figure 4-12: Time series of (a) P_{CO_2} (*ppm*), (b) outgassing from low latitude (*ppm*), (c) ingassing from high latitude (*ppm*), with modern P_0.

$$\frac{dC_d^{13}}{dt'} \approx 0 \rightarrow advection + diffusion + \alpha_{org}\,\gamma_{DIC_S} R_{cp} \cdot 2\overline{B} \approx 0 \tag{4.32}$$

Here we assume $\gamma_{DIC_S} \approx \gamma_{DIC_l} \approx \gamma_{DIC_h}$, i.e. $\delta^{13}C_S \approx \delta^{13}C_l \approx \delta^{13}C_h$. Solving the above equations and assuming that in the transient TM, the vertical mixing term at low latitude is very weak compared to that at high latitude; in the quasi-steady HM, the vertical mixing term at low and high latitude are same, we get the approximate solutions:

$$\overline{B} \approx \left\{ \begin{array}{l} \frac{1}{2}(\frac{|q|}{\lambda V} + \frac{\widehat{M}_{sc}}{\frac{H+h}{2}\lambda\, h})(P_0 - P_h), \text{ TM} \\ \\ \frac{1}{2}(\frac{|q|}{\lambda V} + \frac{2\widehat{M}_{bg}}{\frac{H+h}{2}\lambda\, h})(P_0 - P_l), \text{ HM} \end{array} \right\} \tag{4.33}$$

$$O_d \approx \left\{ \begin{array}{l} O_h^* + R_{op}(P_0 - P_h), \text{ TM} \\ \\ O_l^* + R_{op}(P_0 - P_l), \text{ HM} \end{array} \right\} \tag{4.34}$$

$$\gamma_{DIC_S} \approx \left\{ \begin{array}{l} \gamma_{DIC_d}\ (1 + \frac{R_{cp}}{C_d^{12}}(1 - \alpha_{org})(P_0 - P_h)), \text{ TM} \\ \\ \gamma_{DIC_d}\ (1 + \frac{R_{cp}}{C_d^{12}}(1 - \alpha_{org})(P_0 - P_l)), \text{ HM} \end{array} \right\} \tag{4.35}$$

$$\delta^{13}C_S \approx \left\{ \begin{array}{l} \delta^{13}C_d + 1000\frac{R_{cp}}{C_d^{12}}(1 - \alpha_{org})(P_0 - P_h), \text{ TM} \\ \\ \delta^{13}C_d + 1000\frac{R_{cp}}{C_d^{12}}(1 - \alpha_{org})(P_0 - P_l), \text{ HM} \end{array} \right\} \tag{4.36}$$

Here $\delta^{13}C_d$, C_d^{12} are taken to be constant for the first order approximation. P_0 is the mean ocean phosphorous concentration, $P_0 \approx P_d$. The solutions for the TM are always related to $P_0 - P_h$, i.e. the nutrient difference between deep ocean and high latitude surface ocean; the solutions for the HM are always related to $P_0 - P_l$, i.e. the nutrient difference between deep ocean and low latitude surface ocean. For example,

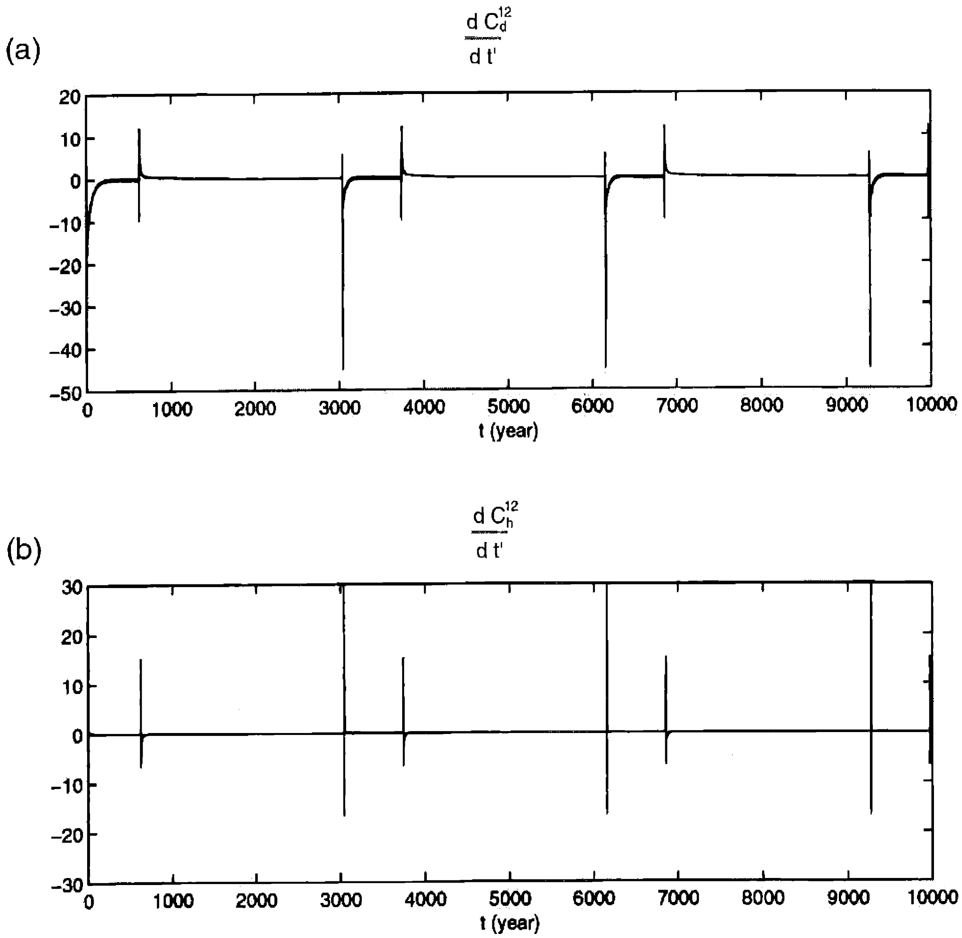

Figure 4-13: Time series of (a) $\frac{dC_d^{12}}{dt'}$ and (b) $\frac{dC_h^{12}}{dt'}$.

the difference in deep and surface ocean oxygen, $O_d - O_i^*$, is linearly proportional to the nutrient difference $P_0 - P_i$ (i=h for TM; i= l for HM) in deep water formation region with the negative redfield ratio of $O : P$. The difference in deep and surface ocean $\delta^{13}C$, $\delta^{13}C_d - \delta^{13}C_S$, is linearly proportional to the nutrient difference $P_0 - P_i, (i = h\ , l)$ in deep water formation region with a negative coefficient, $-1000\frac{R_{cp}}{C_d^{12}}(1-\alpha_{org})$, which is the effective ratio of $\delta^{13}C : P$.

The nutrient difference $P_0 - P_i$ (i=h, l) is determined by ocean overturning circulation strength and vertical mixing. In the transient TM, by solving $\frac{dP_d}{dt'} \approx 0$ and $\frac{dP_l}{dt'} \approx 0$, assuming $\frac{P_l}{1+P_l/P_{cl}} \approx P_l$ (i.e. $P_l \ll P_{cl}$) and $\frac{P_h}{1+P_h/P_{ch}} \approx \frac{P_h}{2}$ (i.e. $P_h \sim P_{ch}$), neglecting the surface horizontal diffusion term and the vertical mixing term at low latitude, finally plug in the TM circulation fields, we have

$$P_l \approx \frac{\frac{|q|}{V}}{\frac{|q|}{V} + \lambda_P} P_0 \approx 0.265 P_0 \tag{4.37}$$

$$P_0 - P_h \approx \frac{\frac{\lambda_P}{2}(3\frac{|q|}{V} + \lambda_P)}{(\frac{|q|}{V} + \frac{\widehat{M}_{sc}}{\frac{H+h}{2}h} + \frac{\lambda_P}{2})(\frac{|q|}{V} + \lambda_P)} P_0 \approx 0.267 P_0 \tag{4.38}$$

Since the high latitude vertical mixing $\widehat{M}_{sc}$ is very strong in the transient TM, it results in lower nutrient difference.

In the quasi-steady HM, by solving $\frac{dP_d}{dt'} \approx 0$ and $\frac{dP_h}{dt'} \approx 0$, assuming $\frac{P_l}{1+P_l/P_{cl}} \approx P_l$ (i.e. $P_l \ll P_{cl}$) and $\frac{P_h}{1+P_h/P_{ch}} \approx P_h$ (i.e. $P_h \ll P_{ch}$), neglecting the surface horizontal diffusion term and assuming the vertical mixing term at low and high latitude are same, finally plug in the HM circulation fields, we have

$$P_h \approx \frac{\frac{|q|}{V} + \frac{\widehat{M}_{bg}}{\frac{H+h}{2}h}}{\frac{|q|}{V} + \frac{\widehat{M}_{bg}}{\frac{H+h}{2}h} + \lambda_P} P_0 \approx 0.16 P_0 \tag{4.39}$$

$$P_0 - P_l \approx \frac{\lambda_P(2\frac{|q|}{V} + 2\frac{\widehat{M}_{bg}}{\frac{H+h}{2}h} + \lambda_P)}{(\frac{|q|}{V} + \frac{\widehat{M}_{bg}}{\frac{H+h}{2}h} + \lambda_P)(\frac{|q|}{V} + 2\frac{\widehat{M}_{bg}}{\frac{H+h}{2}h} + \lambda_P)} P_0 \approx 0.95 P_0 \tag{4.40}$$

Since both the low and high latitude vertical mixing $\widehat{M}_{bg}$ are very weak in the quasi-steady HM, they result in much higher nutrient difference.

With the above results and approximate solutions (Eq. (4.33)-(4.36)), we can understand those correlations of the biogeochemical cycle. For example, in the quasi-steady state O_d is linearly proportional to $P_0 - P_i$ (i=l for HM, i=h for TM) with a negative slope. In the quasi-steady HM, the deep ocean eventually reaches anoxic condition, because the higher nutrient difference, $P_0 - P_l$ (Eq. (4.40)), owing to weak vertical mixing, gives much lower O_d. Conversely, in the transient TM, the deep ocean is replenished with oxygen, because the lower nutrient difference, $P_0 - P_h$ (Eq. (4.38)), owing to strong vertical mixing, gives much higher O_d.

Similarly, in the quasi-steady state $\delta^{13}C_S$ is linearly proportional to $P_0 - P_i$ (i=l for HM, i=h for TM) with a positive slope. In the quasi-steady HM, higher nutrient difference, $P_0 - P_l$ (Eq. (4.40)), owing to weak vertical mixing, gives much heavier $\delta^{13}C_S$; in the transient TM, lower nutrient difference, $P_0 - P_h$ (Eq. (4.38)),owing to strong vertical mixing, gives much lighter $\delta^{13}C_S$. Plug in equation (4.36) the constants $\delta^{13}C_d \approx 0.8$ per mil, $R_{cp} = 106$, $C_d^{12} \approx 2215\ \mu mol/kg$, $\alpha_{org} = 0.977$, $P_0 = 2.07\ \mu mol/kg$ and substitute equations (4.38, 4.40) there, we get:

$$\delta^{13}C_S \approx \left\{ \begin{array}{c} 1.408 \text{ per mil, TM} \\ \\ 2.964 \text{ per mil, HM} \end{array} \right\} \tag{4.41}$$

$$\Delta\delta^{13}C_S \approx 1000\frac{R_{cp}}{C_d^{12}}(1-\alpha_{org})\cdot(0.95-0.267)P_0 \approx 1.56 \text{ per mil} \tag{4.42}$$

The estimated shift in $\delta^{13}C_S$, i.e. $\Delta\delta^{13}C_S$, during mode switch is very close to numerical results (Figure 4-9), especially close to $\delta^{13}C_S$ shift at high latitude (1.6 per mil). Notice here $\Delta\delta^{13}C_S$ is proportional to mean ocean nutrient level, P_0. If we double P_0, we will have $\Delta\delta^{13}C_S \approx 3.12$ per mil. If we reduce P_0 to half, we will have $\Delta\delta^{13}C_S \approx 0.78$ per mil.

The mean surface productivity, $\overline{B}$, is not linearly proportional to the nutrient difference, in equation (4.33) the sensitivity to the ocean circulation fields is dominant. Strong circulation and vertical mixing in the transient TM gives higher surface productivity; weak circulation and vertical mixing in the quasi-steady HM gives lower surface productivity.

4.2.3 Sensitivity experiments on mean ocean nutrient level

To compare with the above theory, we carried the numerical sensitivity experiments on mean ocean nutrient level, P_0. Figure (4-14 to 4-16) shows the results of doubling P_0, i.e. $P_0 = 4.14\ \mu mol/kg$ with other conditions remaining same. The mean surface productivity $\overline{B}$ increases in both modes (Figure 4-14(a)), the deep ocean becomes anoxic faster during the quasi-steady HM, the recover value of deep ocean oxygen is lower in the transient TM (Figure 4-14(b)). The $\delta^{13}C$ shift during the mode switch at high latitude surface increases to ~ 2.8 per mil (Figure 4-14(c)), which is lower than the theoretical prediction for mean surface $\delta^{13}C$ shift ($\Delta\delta^{13}C_S = 3.12$ per mil), but they are not far from each other when corrected with some reasonable adjustment, such as the shift in $\delta^{13}C_d$ causes -0.2 per mil error in the theory (Figure 4-15(b)).

$P_{CO_2}^{atm}$ decreases significantly for $\sim 150\ ppm$ (Figure 4-16 (a)) during the quasi-steady HM, corresponds to the gradually increase in C_d^{12} (Figure 4-15(a)). At low latitude, CO_2

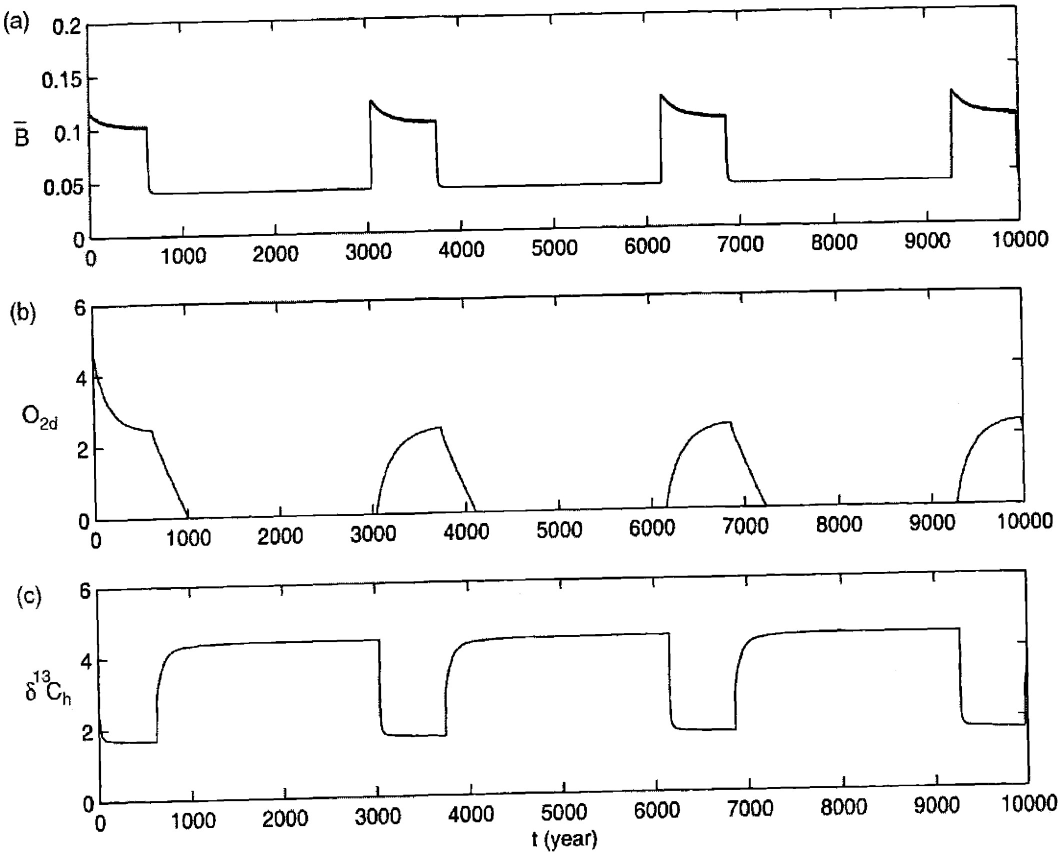

Figure 4-14: Time series of (a) mean surface productivity, (b) deep ocean oxygen, (c) high latitude surface $\delta^{13}C$, with P_0 being doubled of modern value.

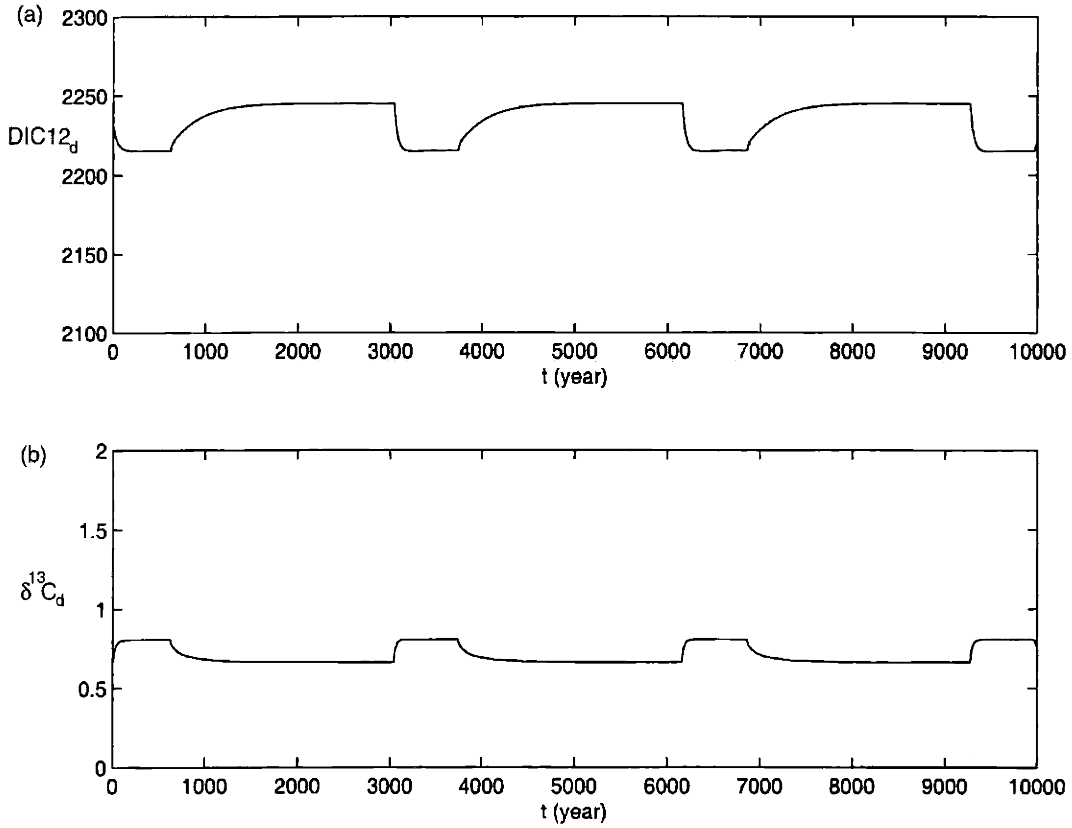

Figure 4-15: Time series of (a) deep ocean DIC^{12}, (b) and deep ocean $\delta^{13}C$, with P_0 being doubled of modern value.

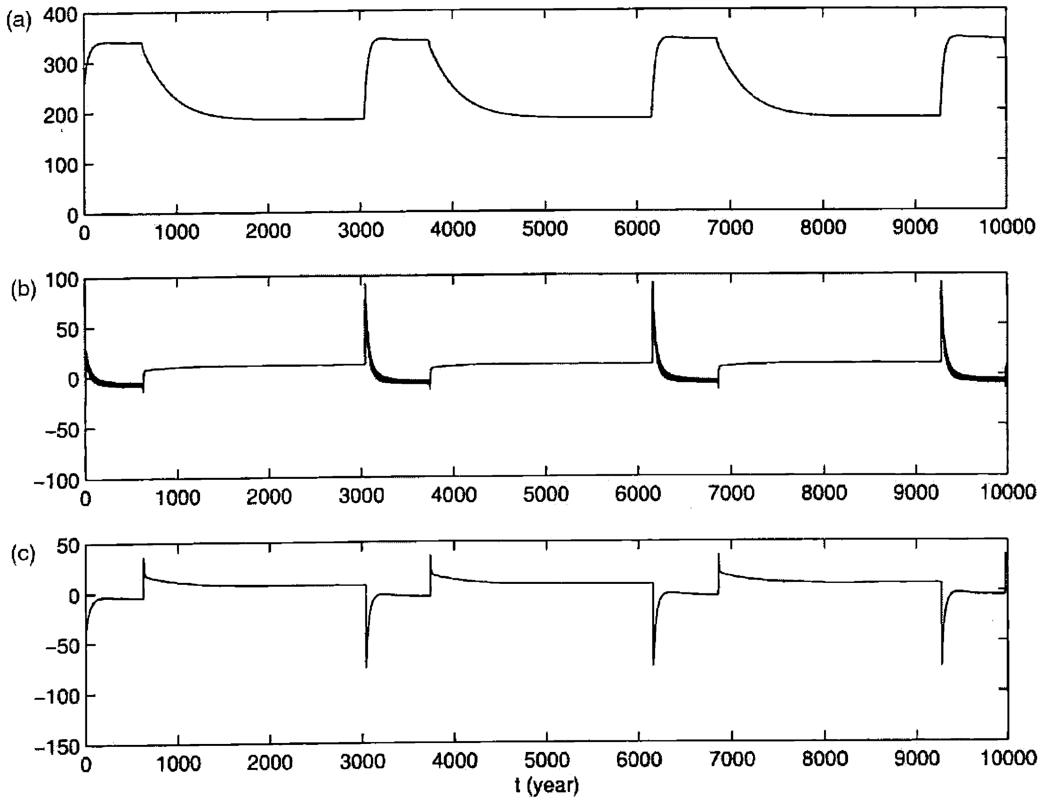

Figure 4-16: Time series of (a) P_{CO_2} (*ppm*), (b) outgassing from low latitude (*ppm*), (c) ingassing from high latitude (*ppm*), with P_0 being doubled of modern value.

is released from surface ocean into atmosphere during the quasi-steady HM and the outgassing is strongest during the switch from the quasi-steady HM to the transient TM. However, there is slightly ingassing in the late stage of the transient TM (Figure 4-16(b)). At high latitude, ingassing of CO_2 occurs during the quasi-steady HM and it is much stronger during the switch from the transient TM to the quasi-steady HM. However, there is strong outgassing during the switch from the quasi-steady HM to the transient TM and slightly outgassing during the late stage of the transient TM (Figure 4-16(c)).

Figure (4-17 to 4-19) shows the results of reducing P_0 to half, i.e. $P_0 = 1.035\ \mu mol/kg$ with other conditions remaining same. The mean surface productivity $\overline{B}$ decreases in both modes (Figure 4-17(a)), the deep ocean becomes anoxic much slower during the quasi-steady HM, the recover value of deep ocean oxygen is much higher in the transient TM (Figure 4-17(b)). The $\delta^{13}C$ shift during mode switch at high latitude surface decreases to ~ 0.9 per mil (Figure 4-17(c)), which is lower than the theoretical prediction for mean surface $\delta^{13}C$ shift ($\Delta\delta^{13}C_S = 0.78$ per mil), but not much different from it. $\delta^{13}C_d$ is almost invariant during mode switch (Figure 4-18(b)).

$P^{atm}_{CO_2}$ increases slightly for $\sim 30\ ppm$ (Figure 4-19(a)) during the quasi-steady HM, corresponds to the slightly decrease in C^{12}_d (Figure 4-18(a)). At low latitude, CO_2 is always released from surface ocean into atmosphere and the outgassing is strongest during the switch from the quasi-steady HM to the transient TM (Figure 4-19(b)). At high latitude, ingassing of CO_2 occurs all the time and it is much stronger during the mode switch (Figure 4-19(c)).

The variations of surface productivity, deep ocean oxygen and $\delta^{13}C_S$ are all sensitive to mean ocean nutrient level P_0, and consistent with the theoretical prediction. The variation in $P^{atm}_{CO_2}$ associated with the variation in C^{12}_d is also very sensitive to P_0, since this is a second order effect, the first order approximate solutions can not explain it.

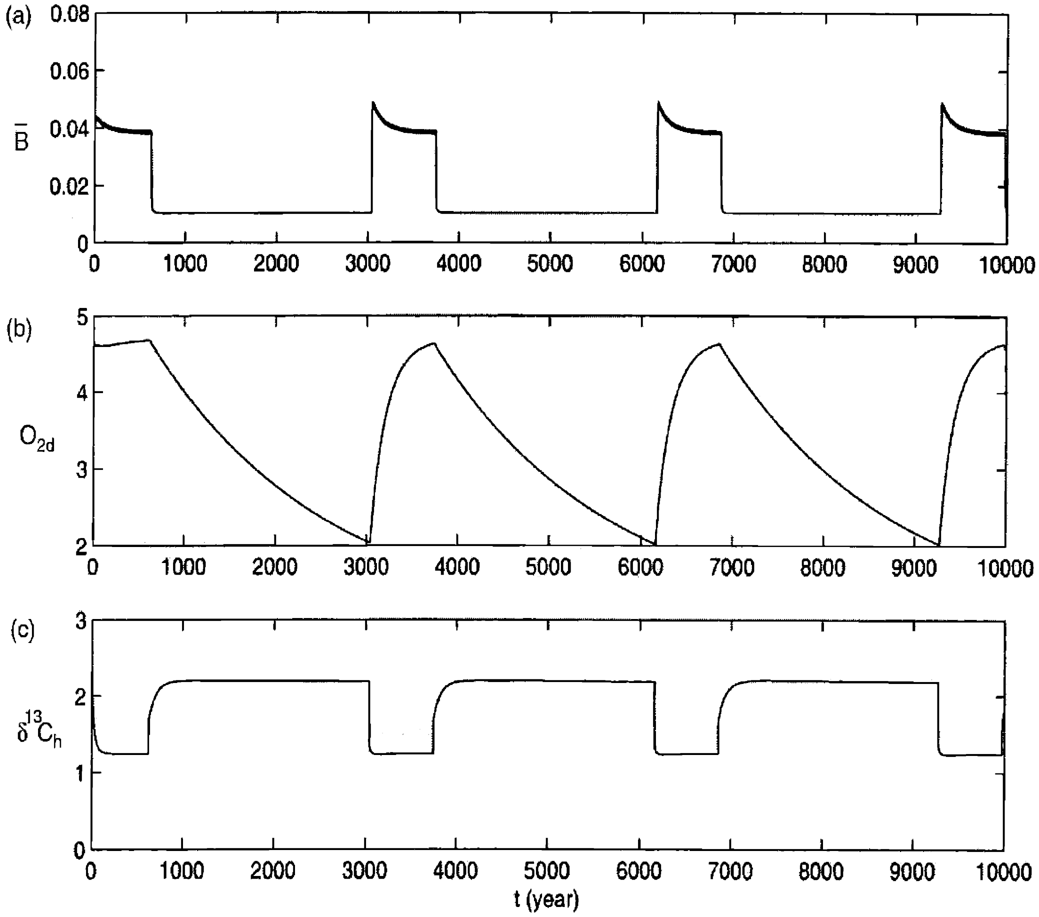

Figure 4-17: Time series of (a) mean surface productivity, (b) deep ocean oxygen, (c) high latitude surface $\delta^{13}C$, with P_0 being reduced to half of modern value.

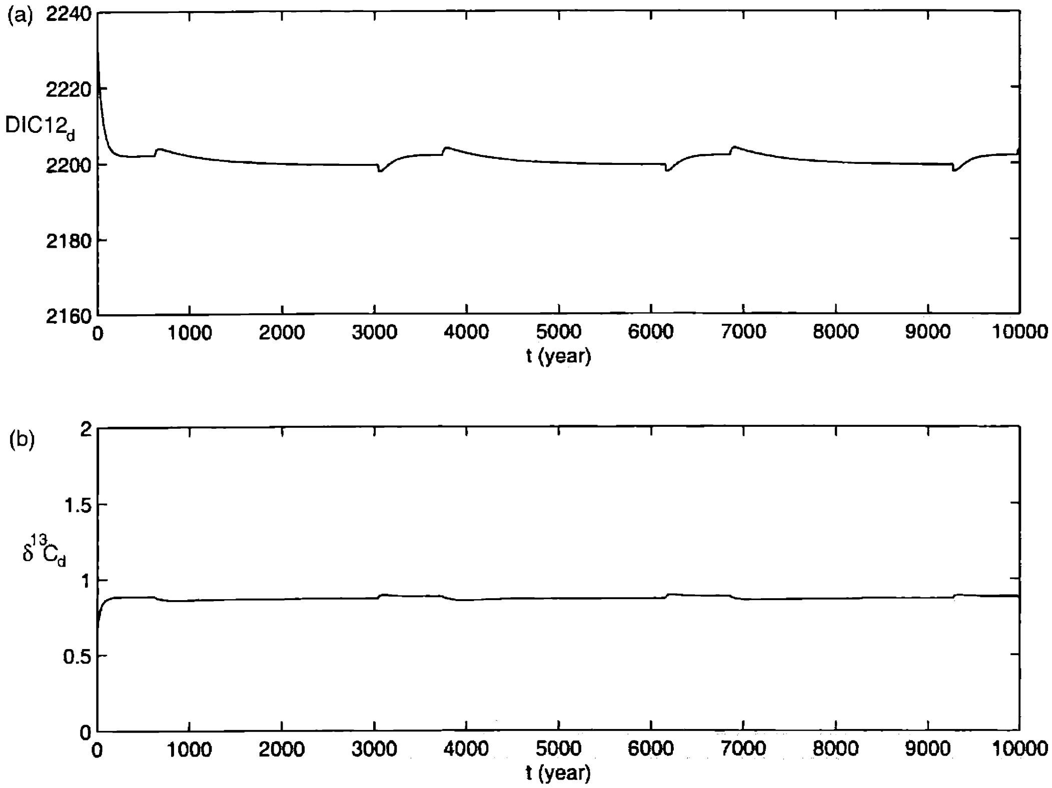

Figure 4-18: Time series of (a) deep ocean DIC^{12}, (b) deep ocean $\delta^{13}C$, with P_0 being reduced to half of modern value.

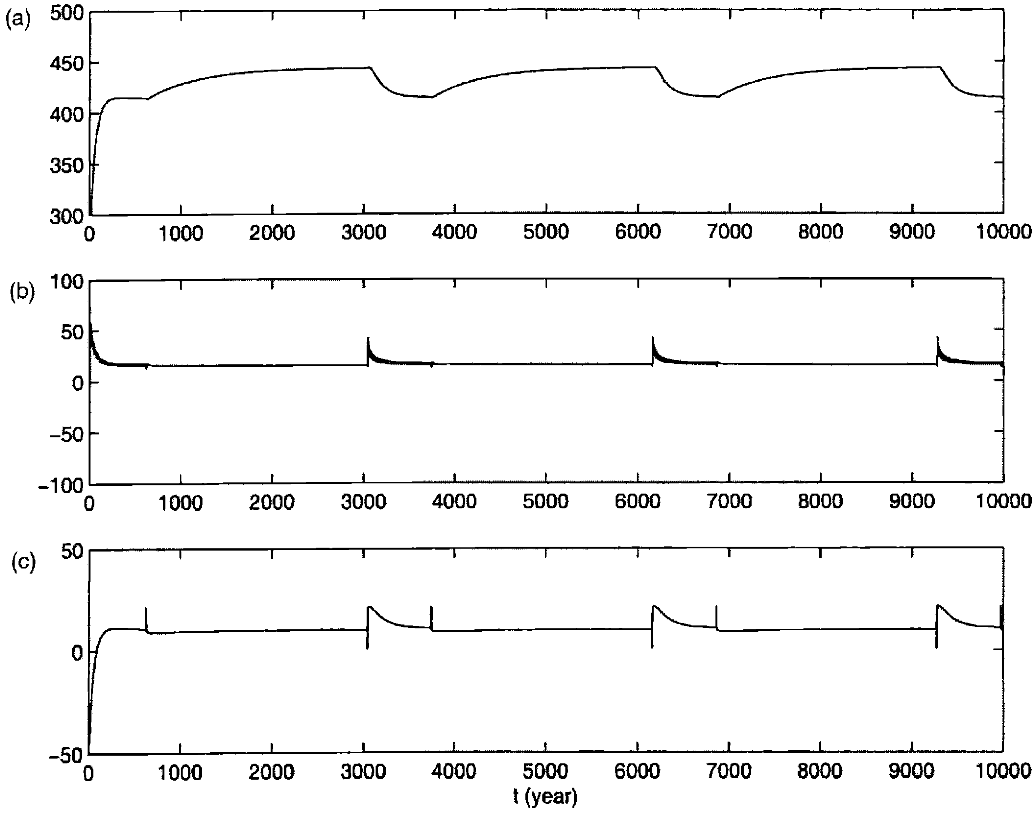

Figure 4-19: Time series of (a) P_{CO_2} (*ppm*), (b) outgassing from low latitude (*ppm*), (c) ingassing from high latitude (*ppm*), with P_0 being reduced to half of modern value.

4.3 Summary

The simple steady state box model of phosphorous and oxygen distribution provides basic guidance to the development of a more complicated 3-d offline biogeochemical model we will discuss in chapter 5. With new parameterization of light limitation of organic matter export, we find different result from what had been published previously (Sarmiento et al., 1988) in which strong overturning circulation resulting in anoxic deep ocean. We show that the deep-sea anoxia can only be achieved with very weak thermohaline circulation and vertical mixing rate.

The time dependent box model for biogeochemical cycle adds not only phosphorous and oxygen, but also carbon cycle and $\delta^{13}C$ into the model driven by oscillatory thermohaline circulation. Significant variations of biogeochemical cycle during circulation mode switch are studied numerically. The HM is characterized with low surface biological productivity, depleted deep ocean oxygen and heavier surface $\delta^{13}C$, owing to very weak vertical mixing; the TM is characterized with high surface biological productivity, replenished deep ocean oxygen and lighter surface $\delta^{13}C$, owing to strong vertical mixing in polar convection. Those correlations are consistent with the paleo record such as the rhythmic sediments in Mid-Cretaceous (Figure 1-2, 1-3), confirming that the cycles in paleo stratification might indeed reflect mode switch in paleo ocean circulation pattern. With the quasi-steady state approximation, we obtain theoretical solutions for surface nutrient distribution, mean surface biological productivity, deep ocean oxygen and surface $\delta^{13}C$. We find that the deep ocean oxygen and surface $\delta^{13}C$ are both linearly proportional to the vertical nutrient difference $P_0 - P_i$ (i=h for TM; i=l for HM). These first order approximate solutions provide better understanding to those correlations and point out how the overturning circulation and vertical mixing rate control the biogeochemical cycle. We show that $\Delta\delta^{13}C_S$ during mode switch is proportional to the mean ocean nutrient level P_0. Numerical sensitivity experiments on P_0 gives consistent results as predicted by the theory. The variation in $P_{CO_2}^{atm}$ associated with the variation in C_d^{12} is very sensitive to P_0, it could have opposing variation trends when P_0 changes from very high to very low level.

Chapter 5

Biogeochemical cycle studied with the offline 3-d biogeochemical model

5.1 Model description

Inferences from the box model are now used to guide, and are tested by, a 3-d ocean circulation and biogeochemical model which also yields insights into the processes that control the detailed vertical and horizontal distribution of oxygen. The 3-d biogeochemical model is based on the same parameterizations of nutrient and oxygen cycling as the box model, but with ocean circulation fields u, v, w, T, S and convective index, used to drive the biogeochemical model taken from an OGCM developed by Marshall et al. (1997a, b) in a domain of irregular geometry to represent the complexities of the ocean basins, the physical model details are discussed previously in chapter 2.

The equation for phosphorous concentration P in every grid cell is :

$$\frac{\partial P}{\partial t} + \nabla \cdot (\overrightarrow{U} P) = \nabla \cdot (\kappa \nabla P) + M + B \tag{5.1}$$

Here M represents convective mixing, $\overrightarrow{U}$ are monthly averaged Eulerian mean velocity fields (u, v, w), $\nabla \cdot (\kappa \nabla P)$ is the parameterized subgridscale tracer mixing and B is the net organic matter export flux from the base of each grid cell given by Eq. (4.3, 4.4) within the euphotic zone. Below the euphotic zone we have

$$B = -\frac{\partial F(z)}{\partial z},\ z < -h_e \tag{5.2}$$

where

$$F(z) = F(-h_e)\exp((h_e + z)/z^*) \tag{5.3}$$

with

$$F(-h_e) = -\int_{-h_e}^{0} \frac{\Phi\epsilon}{h_e} \frac{P}{(P + P_c)} dz \tag{5.4}$$

The sinking particle flux is modeled by a specified profile which decays exponentially (Najjar et al., 1992) with depth. h_e is the depth of the euphotic zone, taken to be the top two layers (120 m) in the model. Z^* is the scale height for remineralization and is chosen to be 400 m, broadly consistent with the sediment trap observations of Lohrenz et al. (1992) in the Sargasso Sea. $P_c = \frac{\Phi\varepsilon_o}{h_e\lambda_p}$ is just as defined in the 3-Box model, (Eq. (4.4)), ε_o is the average 'light utilization efficiency' with a value of 3.5×10^{-5} $\mu mol\ P$ per Joule of incident short wave solar radiation (Parsons,1988), Φ is the net flux of incident short wave solar radiation as a function of latitude, season (Paltridge and Platt, 1976) and depth (Parsons,1988), specifying an albedo which varies with latitude and season (North et al. 1981). λ_p is a global export coefficient, as defined in the 3-Box model; we find a value of $\lambda_p = \frac{1}{30\ months}$ gives reasonable P distribution and it is an appropriate export timescale over much of the (high nutrient, low chlorophyll) ocean. Below the euphotic zone, sinking organic matter from the base of the upper layer is assumed to be remineralized instantly, while within the euphotic zone no remineralization is allowed. Sedimentary processes and river runoff are not represented and so the ocean burden of phosphorous is conserved.

The prognostic equation for oxygen concentration O_2 in each grid cell has the following form:

$$\frac{\partial O_2}{\partial t} + \nabla \cdot (\vec{U} O_2) = \nabla \cdot (\kappa \nabla O_2) + M + R\,B + \frac{V_{po}(O_2^* - O_2)}{\Delta z(k=1)} \delta(K=1) \qquad (5.5)$$

The air-sea flux of oxygen , F_{O_2}, is parameterized employing a piston velocity, V_{po} (Wanninkof, 1992), thus : $F_{O_2} = -V_{po}(O_2 - O_2^*)$, where O_2^* is the surface equilibrium dissolved oxygen concentration . $\delta(K = 1)$ is a delta function, and K labels vertical layers, so the term $V_{po}(O_2^* - O_2)$ is only active in the surface layer of the model.

5.2 Model results with modern ocean circulation

The resulting three dimensional biogeochemical model is spun up from a uniform distribution of phosphorous (2.07 $\mu mol/kg$) (unless otherwise stated) and oxygen ($6.7ml/l$), until an equilibrium state is reached. Pleasingly, when driven (offline) by the simulated modern ocean circulation pattern, the biogeochemical model yields distributions of oxygen and phosphorous that are broadly consistent with observations (Levitus 94) of the modern ocean (Figure 5-1, 5-2). Figure 5-1 shows the surface phosphorous distribution compared with modern observation (Levitus 94), the surface nutrient is higher near eastern tropical region in the north Pacific due to high upwelling rate there; in most other area, the nutrient concentration is higher at polar region than at lower latitude due to light limitation.

Figure 5-2 shows the signature of reduced oxygen (high nutrient) concentrations in Antarctic Intermediate Water of the Atlantic. High productivity in the tropics induces consumption of oxygen below, forming a local subsurface minimum of oxygen. Sinking of North Atlantic Deep Water in the North Atlantic oxygenates the deep ocean, a signature clearly visible into the Southern Hemisphere. The older waters of the deep Pacific are relatively depleted in oxygen, due to cumulative remineralization of sinking organic matter. Productivity in North Pacific surface waters results in the development of anoxia at

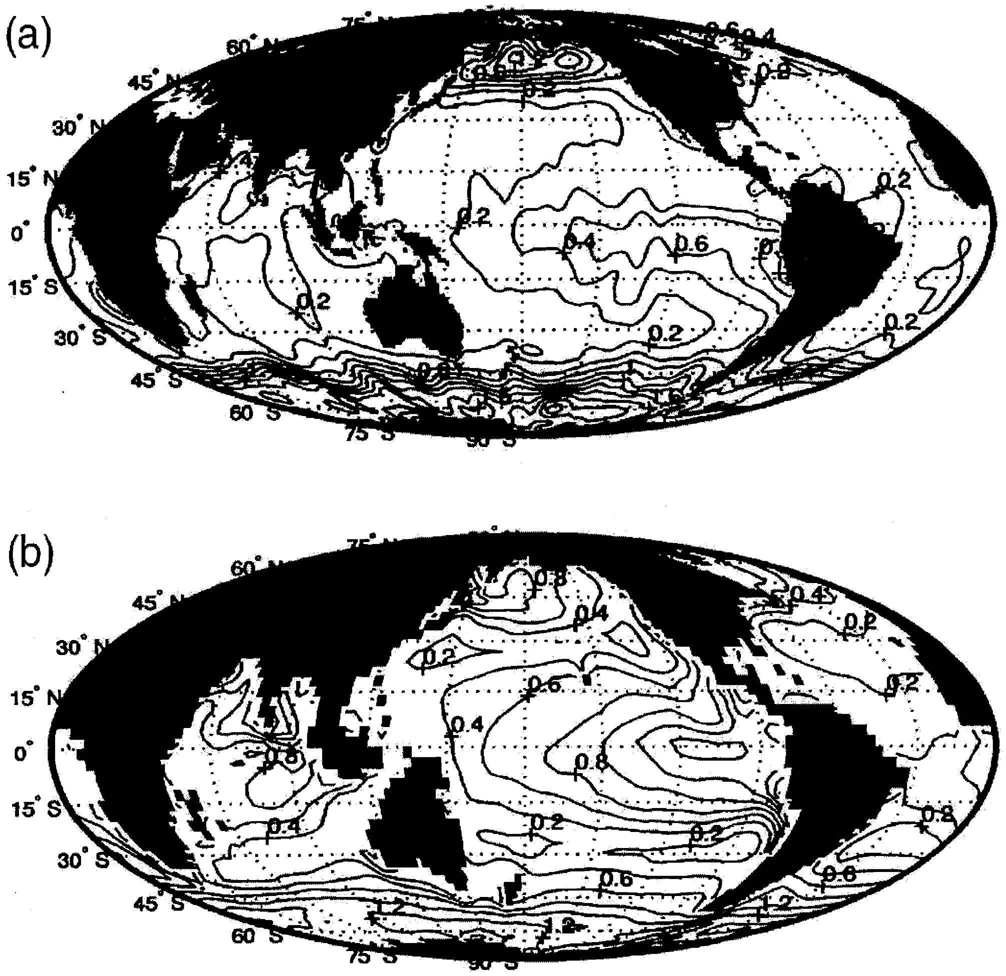

Figure 5-1: Surface nutrient concentration of modern ocean. (a) Surface phosphorous concentration of the modern ocean (μmol/kg) according to the Levitus94 observational data. (b) Surface phosphorous concentration obtained from the 3-d biogeochemical model driven by an ocean circulation model.

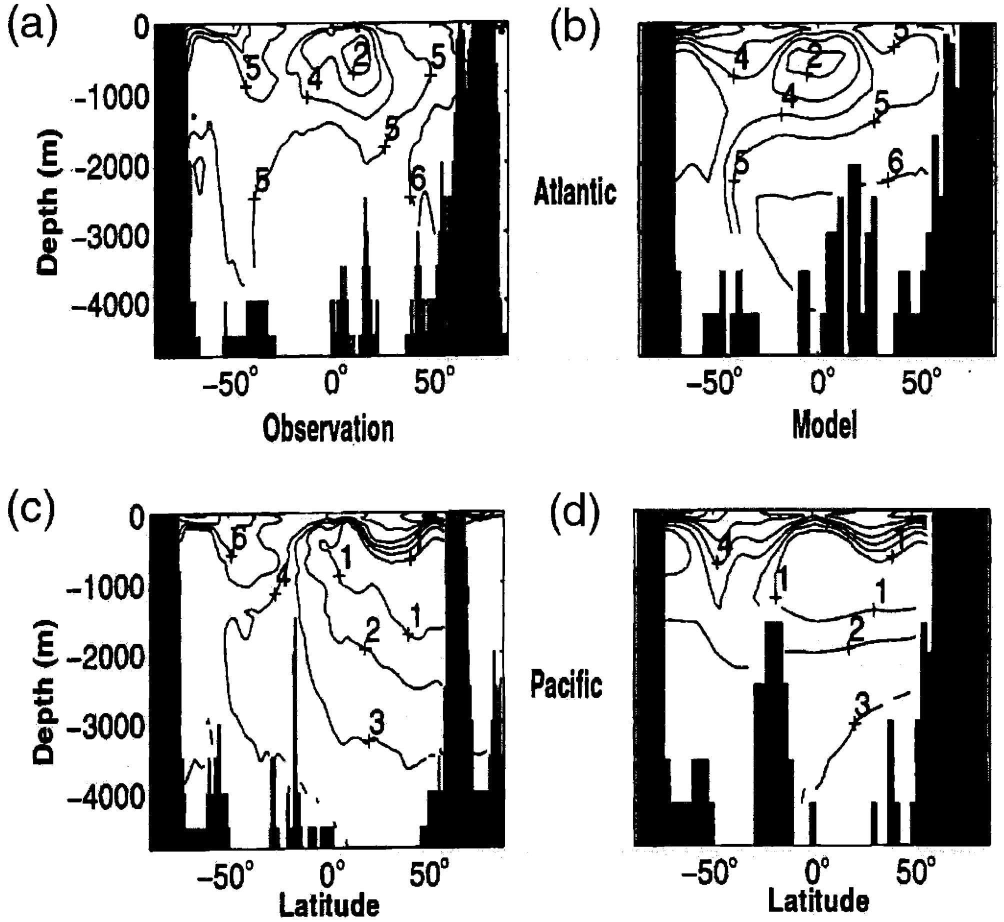

Figure 5-2: Vertical sections of oxygen through the modern ocean (ml/l) according to the Levitus94 observational data (left), compared with those obtained from the 3-d biogeochemical model (right), driven by an ocean circulation model. (a), (b), Atlantic (along 22.5°W) (c), (d), Pacific (along 143.5°W)

intermediate levels, the only example of widespread anoxia in the modern ocean. However the abyss of the modern ocean is rich in oxygen ($\sim 4ml/l$) because, consistent with our box model, there is active polar sinking and convective mixing.

Since the biogeochemical model does not directly depend on modern observations but can successfully reproduce them, we now use the same model to guide speculations about cycles in the late Permian ocean. The possible pattern of ocean circulation in the late Permian is discussed in chapter 2, which depends on the prevailing meteorology, vertical mixing rate and the distribution of land and sea in the late Permian.

5.3 Model results with late Permian ocean circulation

5.3.1 Biogeochemical cycle with thermal mode ocean circulation

To explore the dissolved oxygen distribution implied by the late Permian TM circulation, we used it to drive our 3-dimensional biogeochemical model to equilibrium. We started from the same uniform distribution of phosphorous and oxygen and a surface oxygen concentration of $P_{O_2} \sim 0.21$ bar, as in the modern case. Although at intermediate levels anoxic regions exist (Figure 5-3(a)) , the oxygen concentration in the deep ocean is everywhere high, $\sim 4.7ml/l$, especially below the deep water forming region in the southern high latitudes, where the deep ocean oxygen concentration is about $5ml/l$ (Figure 5-3(b)).

Doubling the mean ocean phosphorous concentration P_0 in the three dimensional model lowers oxygen concentrations, consistent with intuition gained from the box model, but we still find the minimum deep ocean oxygen concentration of about $3.6ml/l$. The 3-d model is less sensitive to P_0 than the box model, due to its higher vertical resolution; the intermediate level where the oxygen concentration is often very low is not explicitly

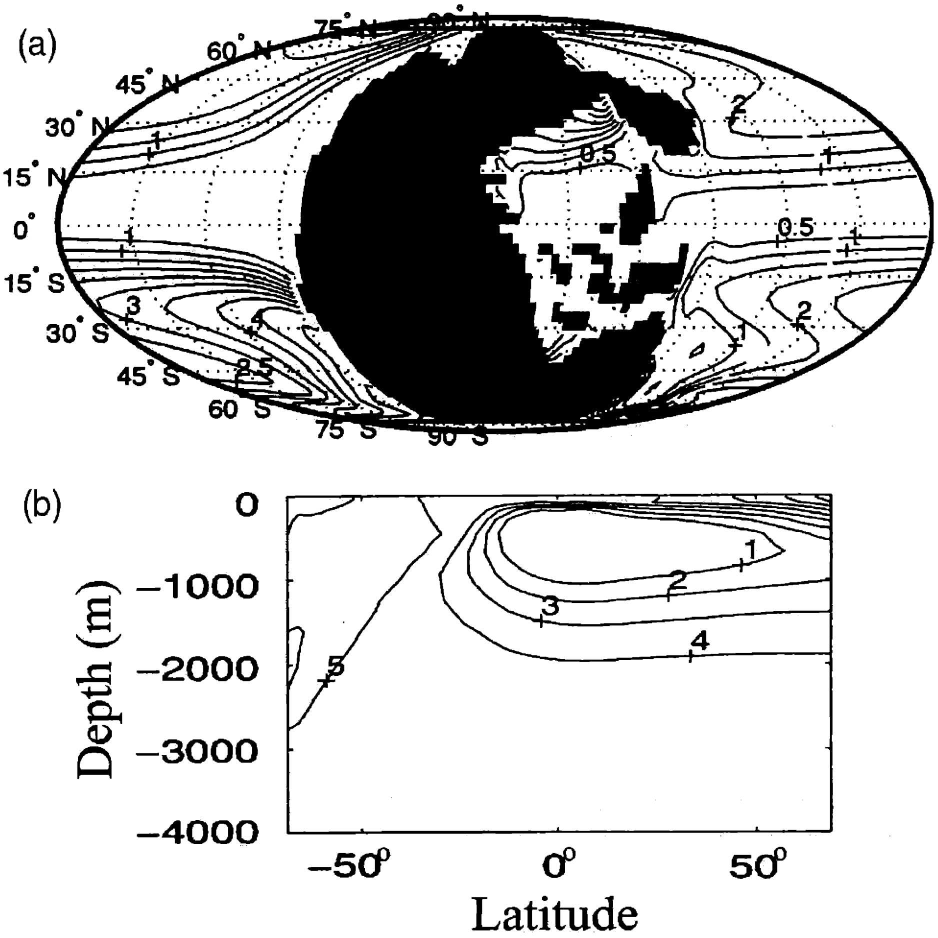

Figure 5-3: Possible oxygen distribution with the late Permian TM ocean circulation. (a) Oxygen distribution (ml/l) at horizontal section at depth z=500 m. (b) Oxygen distribution (ml/l) at vertical section along 130°E.

represented in the 3-box model. In the GCM, increasing P_0 will make the intermediate low oxygen region expand because most organic matter is remineralized there, but the deepwater oxygen is not very sensitive to this aspect. In the box model, the deep box gives the average oxygen concentration from intermediate level to deep ocean, and is more sensitive to P_0.

If the surface equilibrium oxygen concentration is reduced to $P_{O_2} \sim 0.14$ bar, perhaps more typical of the late Permian (Berner and Canfield, 1989), the minimum deep ocean oxygen concentration is lowered to about $2.7ml/l$. Even when a power law profile of sinking organic matter flux is used (Martin et al., 1987), in which more organic matter sinks into the deep ocean consuming oxygen, the minimum deep ocean oxygen concentration is about $3.2ml/l$. As expected from our simple box model, it is very difficult to obtain deep-sea anoxia with the vigorous overturning circulation typical of the presumed late Permian TM.

5.3.2 Biogeochemical cycle with haline mode ocean circulation

We then drive our offline biogeochemical model with the late Permian HM circulation assuming modern atmospheric P_{O_2}. Figure 5-4 shows the contrast of surface ocean phosphorous distribution in the TM and HM circulation respectively. The surface ocean phosphorous distribution is generally higher in the TM than in the HM, except at the northeast corner of the superocean where the surface ocean phosphorous concentration is much higher in the HM (Figure 5-4(b)), due to strong upwelling there. Figure 5-5 shows the vertical section of phosphorous concentration near the eastern boundary of superocean (130°E) for the TM and HM experiments respectively. The phosphorous distribution in the TM (Figure 5-5(a)) has similar pattern as the oxygen distribution (Figure 5-3(b)), but they are inversely proportional to each other, minimum in oxygen concentration corresponds to maximum in phosphorous concentration. The phosphorous distribution at depth in the HM is higher than that in the TM (Figure 5-5(b)), owing to weak vertical mixing. The mean oxygen concentration in the deep ocean is much lower

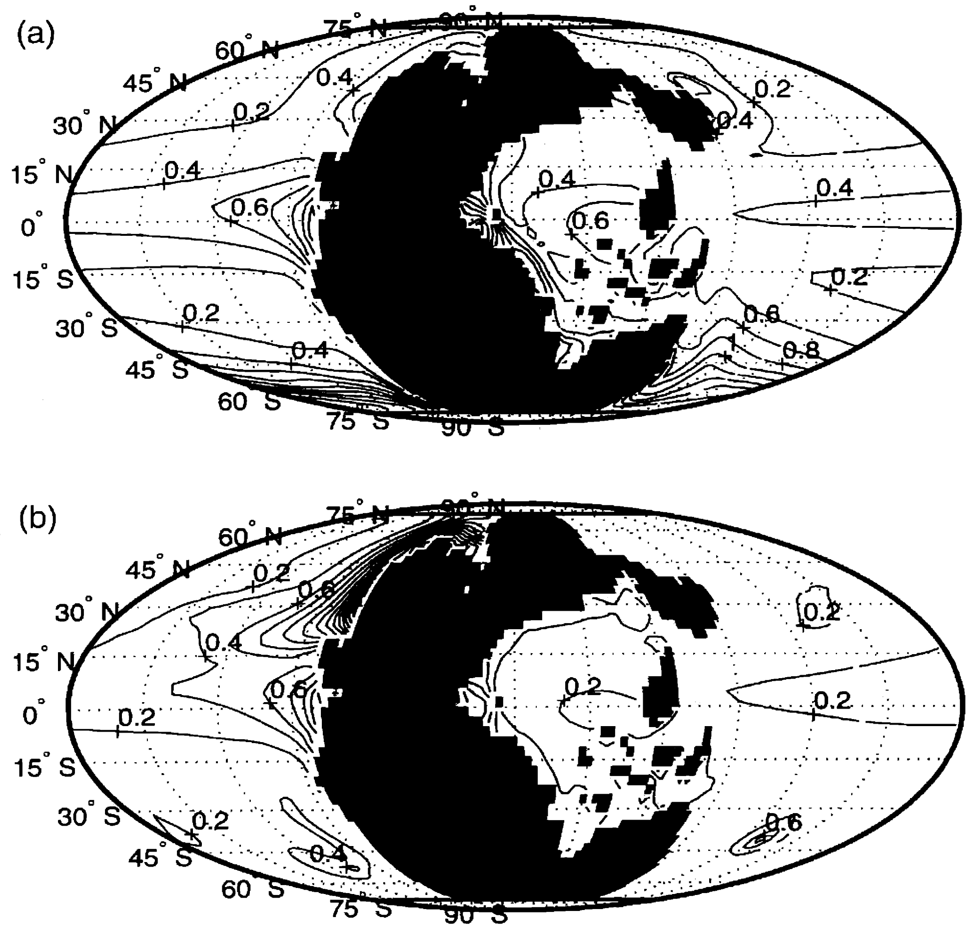

Figure 5-4: Surface phosphorous concentration ($\mu mol/kg$) for the late Permian (a) TM and (b) HM experiments respectively.

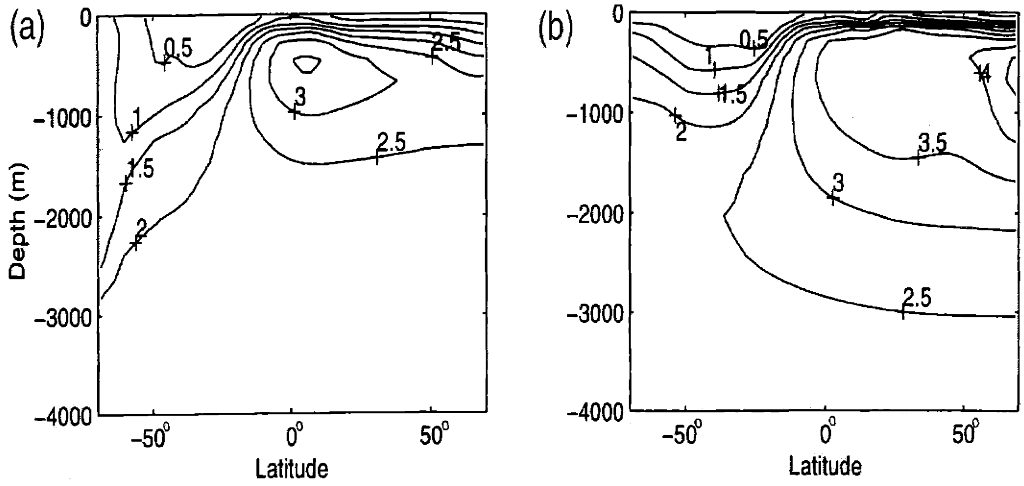

Figure 5-5: Vertical section of phosphorous concentration ($\mu mol/kg$) near the eastern boundary of late Permian ocean (130°E) for (a) TM and (b) HM experiments respectively.

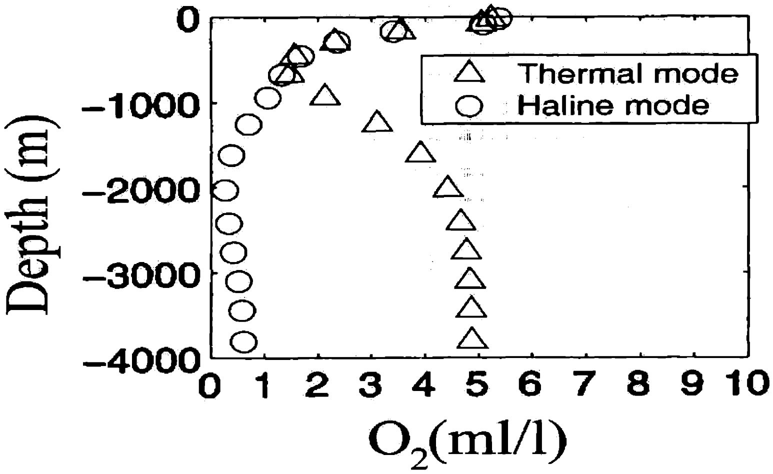

Figure 5-6: Vertical distribution of the horizontally averaged oxygen concentration (ml/l) for the late Permian TM and HM experiments respectively, with modern ocean phosphorous burden and atmospheric P_{O_2}. The deep ocean of the HM experiment exhibits widespread, low oxygen concentrations.

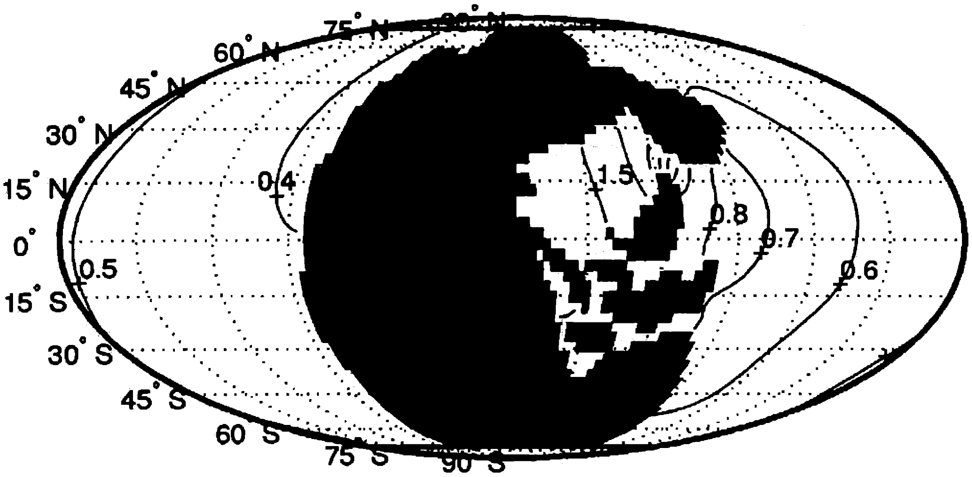

Figure 5-7: Possible oxygen distribution (ml/l) at bottom of the ocean with the late Permian HM ocean circulation.

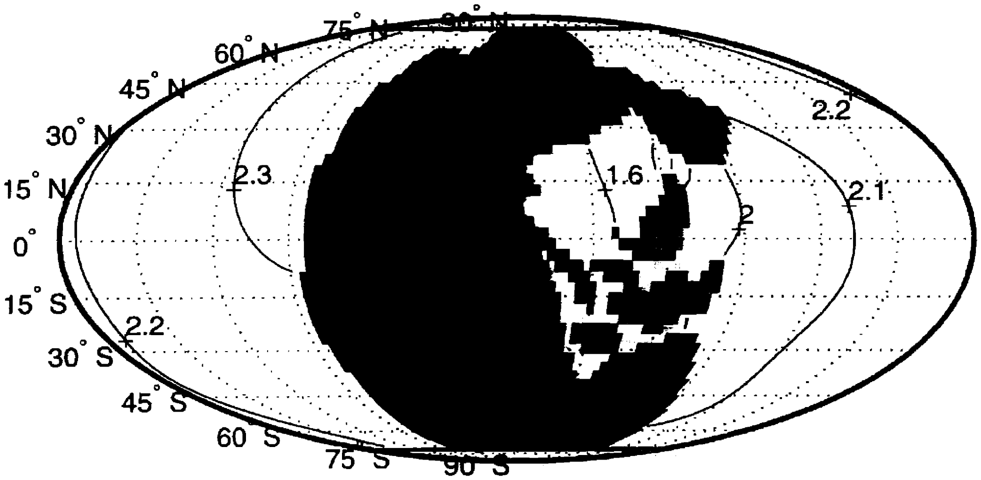

Figure 5-8: Possible phosphorous distribution ($\mu mol/kg$) at bottom of the ocean with the late Permian HM ocean circulation.

than that accompanies the TM (Figure 5-6), and vast areas of the eastern Panthalassic deep ocean become very depleted in oxygen (Figure 5-7). Correspondingly, the deep ocean phosphorous concentration is much higher, especially along the northeast boundary of the superocean (Figure 5-8). This result is obtained after many thousand of years of integration, spun up from the equilibrium oxygen distribution we obtained with the TM circulation. Again this is broadly consistent with the predictions of our box model.

In this model experiment, the quasi-steady HM is sustained for about 2830 years between transient TM 'flushing' events. The offline biogeochemical model driven by the HM circulation exhibits highly depleted deep ocean oxygen as it approaches steady state, but the time scale to achieve this may be many thousands of years in part due to the extremely sluggish ocean circulation. For a super-anoxia event to persist in the geologic record, the time scale for oxygen depletion must be considerably shorter than the repeat time of the transient TM flushing events. We note here that the oxygen depletion time scale is very sensitive to the form of the particle remineralization profile. Using an exponential flux profile (Najjar et al., 1992) we find a much longer oxygen depletion time (more than 10,000 years) than with a power law flux profile (Martin et al., 1987) (within 1,000 years) though the final state is similar in both cases. The mechanism and nature of particle remineralization is currently very poorly understood. In the event that the deoxygenation time scale is shorter than the repeat time of transient TM flushing events, sustained periods of deep-sea anoxic conditions are possible.

5.4 Summary

The purpose of this study with offline 3-d biogeochemical model, driven by late Permian ocean circulation fields we obtained from the OGCM, is to provide possible mechanism for the deep-sea anoxic events that might have happened in paleo oceans. For focus, here we address only the issue of deep-sea anoxia, but in so doing we also provide some physical and biogeochemical context for the proposed mass extinction hypotheses. Although many aspects of the sedimentary, paleontological, and geochemical record are consistent with late Permian ocean anoxia at shallower depths (Erwin, 1994; Wignall and Twitchett, 1996), our goal here is to evaluate claims (Isozaki, 1997; Kajiwara et al., 1994) that the deep ocean (depths > 3000 m) could have become anoxic, and sustained this condition more-or-less continuously for tens of millions of years. This is important given that the records of late Permian deep sea anoxia are retained within obducted accretionary complexes (Isozaki, 1997; Kajiwara et al., 1994), and that such rocks are not necessarily representative of the sea bottom formed in the open ocean (Saleeby, 1992; Ishiwatari, 1991). Instead, subduction complexes and obducted blocks of oceanic crust could be interpreted to represent closure of back-arc basins rather than open ocean basins. Thus, it is possible that the geochemical records are from a restricted part of the late Permian ocean, similar to the modern Cariaco basin (Zhang and Millero, 1993), rather than indicative of the great expanse of the Panthalassic deep ocean. At this time only two data points in Japan and western Canada are available supporting late Permian deep-ocean anoxia. Until new data become available the only means to further test the notion of Panthalassic deep-ocean anoxia is through theoretical and numerical simulation of ocean circulation and biogeochemical patterns. In this manner, physically implausible scenarios can be eliminated, providing a clearer image of what processes would have been required to induce an anoxic state which could have persisted or recurred for millions of years.

With the 3-d offline biogeochemical modeling of the late Permian ocean, we shows that the strong TM leads to well oxygenated deep ocean, the weak HM leads to highly depletion of deep ocean oxygen in the event that the deoxygenation time scale is shorter than the repeat time of transient TM flushing events. As the HM is unstable, a deep-sea anoxia persisting for millions of years is not clearly supported by this study. The conclusions are also consistent with the simple biogeochemical box model results discussed in chapter 4, that only weak ocean circulation and vertical mixing rate could lead to highly depletion of deep ocean oxygen.

Our results here seem difficult to reconcile with a persistent (20 million year), ocean wide, deepwater anoxic event across the P/T boundary (Isozaki, 1997). However, most geological records for the late Permian do not resolve the timescales (a few thousand years) of the thermohaline oscillations discussed in this paper. It is possible that the properties of long periods of HM circulation could dominate the cycle and the 'time-averaged' sediment samples, leading to the appearance of a sustained anoxia.

The sulfur isotope record (Kajiwara et al., 1994) suggests that the extended period of anoxia is punctuated by a temporary, massive mixing across the P/T boundary. The deep ocean is interpreted to have been oxic during this mixing episode despite the presence of black shales in the sediments (Kajiwara et al., 1994). This study suggests that such evidence could be consistent with long-term (many thousands of years) changes between HM and TM ocean states. On these longer timescales such changes might be forced by variations in external forcing and the inherent instability of the HM.

In summary, while these model results are not easily reconciled with the notion of truly persistent, deep ocean anoxia induced by changes in ocean circulation, they illustrate possible mechanisms of ocean circulation and biogeochemistry which may be consistent with the sedimentary record.

Chapter 6

Summary and future work

6.1 Summary

In summary, the thesis is focused on the ocean circulation pattern in paleo oceans which could have been very different from modern ocean. In warm equable paleoclimates, possible circulation patterns include multiple steady state ocean circulation modes and the self-sustained thermohaline oscillations associated with the unstable HM. The implication of different circulation modes for the biogeochemical cycle are also studied and compared with the paleo records, such as the rhythmic stratification from Mid-Cretaceous sediments. The study of the interaction between ocean circulation and biogeochemical cycle provides better interpretation of paleo records related to the paleo ocean circulation pattern.

OGCM results for the paleo ocean such as late Permian show that different modes of ocean circulation might exist in warm climate: a strong TM induced by cooling at high latitudes and a weak HM induced by evaporation at subtropics. In the TM, sinking in high-latitudes drives a vigorous overturning circulation with deep-reaching convection - it is inherently stable. In the HM, with warm salty intermediate water formed in the subtropics over a deep stratified ocean, the overturning circulation is much weaker and shallow. This HM, which can be induced by an enhanced hydrological cycle and / or weak diapycnal mixing in the ocean, is inherently unstable, flushed by thermally-driven polar convection every few thousand years.

Using an idealized box model, we have mimicked, and elucidated the underlying mechanisms of, haline - thermal mode switch which is a property of ocean circulation models in certain parameter regimes. Using steady solutions, and time-dependent integrations of the box model, we are able to fully explore the circulation and stability properties of the system over a wide range of parameter space. The simple model illustrates the inherent instability of the HM and the importance of polar thermal convection in the flip mechanism. Motivated by our OGCM results, the localized nature of polar convection is parameterized in the box model through a threshold criterion, ε, so that polar convection can occur even though the large-scale, mean vertical density structure is statically stable. Oscillatory solutions are found even with a linear equation of state.

On the bifurcation diagram of overturning strength and freshwater forcing, there exists a window in which the steady HM is unstable, and thermohaline oscillations are possible. When the freshwater forcing exceeds an upper limit, only stable HMs exist. For freshwater forcing below a lower limit, only stable TMs exist. But within a broad window of freshwater forcing the HM oscillates, and the oscillation period exhibits a minimum. On the bifurcation diagram of overturning strength and vertical diffusivity, there is a window where the thermohaline oscillation is possible. Here, the oscillation period decreases monotonically as the vertical diffusivity increases.

Our knowledge of actual past ocean circulation regimes emerges largely from the sedimentary record, through the preservation of isotopic signatures or organic material. To connect these models more closely to the data record, and in order to understand the implications of these significant global climate changes for the biogeochemical system, we are implementing biogeochemical cycles into these models.

The two circulation modes (TM and HM) have very different biogeochemical implications. A steady state 3-box model and an offline 3-dim biogeochemical model are developed to study the deep sea anoxia in late Permian ocean. The strong TM leads to well oxygenate deep ocean. It is very difficult for us to conceive of wide-spread, persistent deep-sea anoxia in the presence of such a circulation pattern, although there could have been anoxic regions at intermediate levels beneath upwelling areas, as in the Pacific and Arabian Sea today. The weak HM leads to highly depletion of deep ocean oxygen when the depletion time scale is shorter than the flushing period.

The thermohaline oscillations also have important implication on ocean biogeochemical cycles. Time dependent solutions of biogeochemical cycle are studied, driven by the oscillatory thermohaline circulation obtained in the 3-box model. During the sustained HM (between flushing events), the overturning circulation is weak and shallow, and deep ocean transport is dominated by weak, small scale mixing processes. In this situation deep ocean oxygen can gradually become significantly depleted, this also associates with lower surface biological productivity and heavier surface $\delta^{13}C$, owing to the very weak vertical mixing. During the transient TM, strong deep convection occurs in the polar region and deep ocean oxygen is replenished, this also associates with higher surface biological productivity and lighter surface $\delta^{13}C$, owing to strong vertical mixing. Hence, oscillatory overturning circulation could lead to cycles of biogeochemical variables with period ranging between a few hundred and a few thousand years. The correlations of deep ocean oxygen, surface biological productivity and $\delta^{13}C$ during the cycle are consistent with paleo records (Figure 1-2, 1-3). The $\delta^{13}C$ shift during mode switch is proportional to mean ocean nutrient level P_0. The P_{CO_2} variation during mode switch is also sensitive to P_0. Such internal thermohaline oscillations are more likely to happen in warm equable paleoclimates, such as the Mid-Cretaceous, and late Permian, since, as discussed above, the amplitude of freshwater forcing beyond which no stable steady TM exist is smaller when the meridional temperature gradient is weak. Although in the time dependent box model, those variations in biogeochemical cycle are driven by an internal self-sustained thermohaline oscillation, the variation trends will also persist when driven by the thermohaline oscillation forced externally such as the Milankovitch cycle.

Since the haline-thermal mode switching has significant impacts on the biogeochemical cycle as we found in this thesis, the events might have been imprinted in the paleo records if they have really occurred before. For example, the haline-thermal mode switching might have occurred during the warm equable paleoclimates, such as that in Mid-Cretaceous. One could search in the deep-sea sedimentation from that period for rhythmic layers, looking for variations in the organic-carbon concentrations, correlated with changes in surface primary productivity and shifts in surface $\delta^{13}C$ as discussed in chapter 4. The surface primary productivity might be reflected by the biogenic carbonate and silica concentration in the sediments. During the haline-thermal mode switching, the ocean temperature and salinity distribution would also change significantly, this could result in the variations in $\delta^{18}O$ in the sediments. If we can find the above correlated variations in the biogeochemical cycle and shifts in the isotopes from high resolution deep sedimentation, they will be important evidence to support the haline-thermal mode switching hypothesis.

However, the resolution of most geological records for such warm paleoclimates cannot resolve centuries-millennial timescales, and the long periods of HM circulation might dominate the oscillations. It would be very hard to observe such short periods directly in those records even if they occurred. What we observed in the sediments may be the time averaged results of the thermohaline oscillations which looks like a continuous HM mode circulation. If the paleo records are undersampled in time interval, the thermohaline oscillation frequency will be aliased to lower frequency as showed in chapter 3. Thus we can look into the power spectrum of the time series of the rhythmic stratification to search for significant peaks at lower frequencies which cannot be explained by other processes such as the Milankovitch orbit cycle, those evidence would be consistent with the haline-thermal mode switching hypothesis.

Localized deep polar convection in a (generally) stably stratified ocean, which is a key component of these oscillations, is consistent with modern observations of the convective process (Marshall and Schott, 1999). In today's ocean, deep polar convection only happens in confined regions. Here, in a 3-d OGCM, we showed that the formation of warm, salty large scale eddies in the polar surface region which act as 'pre-conditioning' centres for deep convective activity. This process is clearly related to rotating fluid dynamics, it is parameterized simply in the box model which does not explicitly account for rotational effects. Localized convective activity can also be found in 2-d OGCMs (Marotzke, 1989; Winton and Sarachik, 1993) when the polar density distribution is not homogeneous for a particular freshwater forcing profile.

During glacial periods, the meridional temperature gradient is stronger and the critical amplitude of freshwater forcing beyond which no steady TM exists would be larger. On the other hand, the freshwater forcing can be increased by ice melting in polar region and a similar oscillation might be a possibility.

6.2 Future work

Several important issues of details remain for investigation in the future. In this thesis, the 3-box model for thermohaline circulation is very simple, such as the assumption of one deep ocean box and the linear relation between overturning strength and surface density gradient. A 4-box model with two deep ocean boxes and more realistic assumption relating overturning strength to surface density, deep ocean density gradient should give better results. Also it is worth to couple the 3-box model with the atmosphere on top, since the atmosphere provides negative feedback to the air-sea heatflux, we expect that the oscillation solutions would still exist in the coupled box model.

Beyond, several other questions need to be answered in the future study. For example, why is the TM solution of the late Permian ocean highly asymmetric and how sensitive is the thermohaline circulation to the land-sea distribution of late Permian? The question can be answered with sensitivity experiments adding small perturbations to the idealized land-sea distribution. Why the deep convection during the TM always occurs along the eastern boundary of the ocean, not the western boundary? How sensitive is the conditions of obtaining the HM to the ocean depth? What is the physical mechanism of formation of large scale eddies at polar surface during the quasi-steady HM?

Finally, is a hydrologic cycle double the intensity of today's a plausible scenario during the late Permian? What determines the upper limit of the intensity of the hydrological cycle in a warm equable climate? We know that the specific humidity at saturation, q^*, depends on the temperature of the atmosphere according to the Clausius-Clapeyron relationship:

$$q^* \approx \frac{0.621e_o}{P} \exp\{\frac{L}{R_v}(\frac{1}{273} - \frac{1}{T})\}. \tag{6.1}$$

Here L is the latent heat of vaporization, R_v is the gas constant for water vapor, e_o is the saturated water vapor pressure at $T = 273K$, P is the atmosphere pressure, T is the air temperature. Let $T = \overline{T} + T'$, thus we have

$$\frac{1}{T} \approx \frac{1}{\overline{T}}(1 - \frac{T'}{\overline{T}}). \tag{6.2}$$

Assuming $\overline{T} = 278K$ at polar region, then the above two equations give us

$$q^* \approx \overline{q^*} \exp(0.07T'). \tag{6.3}$$

$\overline{q^*}$ is the saturated specific humidity at the mean polar air temperature $\overline{T}$. If we plug $T' \approx 10K$ in the above equation, here T' is the increase of polar air temperature, similar to that indicated by paleo records in the warm equable paleoclimates, we will have $q^* \approx 2\overline{q^*}$, i.e. q^* is doubled. Meanwhile because the relative humidity is nearly unchanged with temperature, the specific humidity q and precipitation at polar region will also be doubled. Since the global hydrological cycle is a closed system; that is, the total quantity of water on earth is essentially constant, the total evaporation at subtropics will also be doubled to compensate the enhanced polar precipitation. In reality, the precipitation and evaporation may cancel each other at the same region and their distribution pattern might have been very different in the warm paleoclimates, so this estimation can serve as the upper limit of the intensity of the hydrological cycle for the given increased polar air temperature.

Another physical constrain for the intensity of hydrological cycle is based on the fact that any enhanced downward longwave radiation is mainly damped through surface latent heat flux. In the warm equable climate with higher greenhouse gas (CO_2) concentration in the atmosphere, the downward longwave radiation flux increases, thus the surface evaporation has to increase to maintain heat balance. Besides, the increased water vapor in the warmer atmosphere, which is another greenhouse gas, will also enhance the downward longwave radiation flux and thus the surface evaporation. The net increase in subtropical surface evaporation might be small, but if the compensated increase in precipitation mainly occurs at polar region, then the net increase in the freshwater flux E-P at subtropics will be significant, and the subtropical peak of positive E-P will shift to higher latitude.

Manabe and Stouffer (1994) showed that in a CO_2 quadrupling experiment, the intensity of the net freshwater flux, E-P, increased to about 1.5 of the present level. In the late Permian, the P_{CO_2} level could have been very much higher than that of today (Budyko and Ronov, 1979). More over, increased dust and sulphate aerosols due to stronger volcanic activity during the late Permian could also induce stronger freshwater flux (Kozur, 1998). It is also notable that, in a warm, equable climate, the smaller the polar-equator surface temperature gradient is, the weaker is the critical intensity of E-P required to induce the HM. It would be much easier to switch into the oscillatory HM during warm equable climates. To study this problem, we need an atmosphere circulation model which can provide reasonable physical processes in the warm equable climates quite different from today's. Although, in this thesis, we focus on the ocean circulation in warm equable paleoclimates, it is also interesting to apply the methods to study the thermohaline oscillations driven by enhanced freshwater forcing induced by iceberg discharge into the ocean during the glacial period.

Appendix A

Linear analysis for stability

The stability of the multiple steady state thermohaline circulation obtained from the 3-box model in chapter 3 can be studied with linear analysis.

Let the vector $\mathbf{y} = [\mathbf{y}] + \mathbf{y}\prime$ represents the non-dimensional dynamic state of the 5-dim system near the steady state, here $[\mathbf{y}]$, $\mathbf{y}\prime$ represents the steady state and the small perturbations around it respectively, i.e.

$$\mathbf{y} = \begin{pmatrix} \Delta T \\ \overline{T} \\ T_d \\ \Delta S \\ \overline{S} \end{pmatrix}, \; [\mathbf{y}] = \begin{pmatrix} [\Delta T] \\ [\overline{T}] \\ [T_d] \\ [\Delta S] \\ [\overline{S}] \end{pmatrix}, \; \mathbf{y}' = \begin{pmatrix} \Delta T' \\ \overline{T}' \\ T_d' \\ \Delta S' \\ \overline{S}' \end{pmatrix}. \tag{A.1}$$

Here $\Delta T, \overline{T}, T_d, \Delta S$, and $\overline{S}$ are the non-dimensional dynamic variables of the system defined in chapter 3. Owing to the conservation of total salinity of the system, $S_d = (1+\delta)(1-\overline{S}) + \overline{S}$, so there are only five independent dynamic variables. The non-dimensional dynamic equations of the system in chapter 3 can be written as:

$$\frac{d\mathbf{y}_i}{dt'} = \mathbf{G}_i(\mathbf{y}), \; i = 1, 2, 3, 4, 5 \tag{A.2}$$

To see whether the small perturbations grow or decay, i.e. whether the steady state is stable or not, we can derive the linearized non-dimensional dynamic equations of the perturbations near the steady states. For the perturbations near the strong and weak steady TM, and those near the steady HM satisfies $\Delta\rho_{hd} < \varepsilon$, i.e. the steady HM which will never reach the threshold for polar convection (such as that in region IV on the f-c bifurcation diagram (Figure 3-2)), the linearized non-dimensional dynamic equations can be written as:

$$\frac{d\mathbf{y}'}{dt'} = \mathbf{A}\mathbf{y}'. \tag{A.3}$$

Here $\mathbf{A}$ is the 5×5 Jacobian matrix at the steady state,

$$\mathbf{A}_{ij} = \frac{\partial \mathbf{G}_i}{\partial \mathbf{y}_j}\Big|_{\mathbf{y}=[\mathbf{y}]},\ i,j = 1,2,3,4,5 \tag{A.4}$$

Based on the equations in chapter 3, we can get all the elements of $\mathbf{A}$:

$$\mathbf{A} = \begin{pmatrix} \mathbf{A}_{11} & \mathbf{A}_{12} & -\mathbf{A}_{12} & \mathbf{A}_{14} & 0 \\ \mathbf{A}_{21} & \mathbf{A}_{22} & -1-\mathbf{A}_{22} & \mathbf{A}_{24} & 0 \\ -\delta\mathbf{A}_{21} & -\delta(1+\mathbf{A}_{22}) & \delta(1+\mathbf{A}_{22}) & -\delta\mathbf{A}_{24} & 0 \\ \mathbf{A}_{41} & 0 & 0 & \mathbf{A}_{44} & \gamma(1+\delta)\mathbf{A}_{12} \\ \mathbf{A}_{51} & 0 & 0 & \mathbf{A}_{54} & (1+\delta)(1+\mathbf{A}_{22}) \end{pmatrix} \tag{A.5}$$

For the TM,

$$\mathbf{A}_{11} = -1 - K - \frac{M_l + M_h}{2} - 3\mu_f\gamma[\Delta T] + \frac{3}{2}\mu_f\gamma R[\Delta S] + \mu_f([T_d] - [\overline{T}])$$

$$\mathbf{A}_{12} = \frac{M_l + M_h}{\gamma} - \mu_f([\Delta T] - R[\Delta S])$$

$$\mathbf{A}_{14} = -\mu_f R([T_d] - \left[\overline{T}\right]) + \frac{3}{2}\mu_f \gamma R\left[\Delta T\right]$$

$$\mathbf{A}_{21} = \frac{\gamma(M_h - M_l)}{4} - \frac{\gamma^2}{4}\mu_f R\left[\Delta S\right] + \frac{\gamma^2}{2}\mu_f\left[\Delta T\right] + \frac{\gamma}{2}\mu_f([T_d] - \left[\overline{T}\right])$$

$$\mathbf{A}_{22} = -1 - \frac{M_l + M_h}{2} - \frac{\gamma}{2}\mu_f(\left[\Delta T\right] - R\left[\Delta S\right])$$

$$\mathbf{A}_{24} = -\frac{\gamma}{2}\mu_f R([T_d] - \left[\overline{T}\right] + \frac{\gamma}{2}\left[\Delta T\right])$$

$$\mathbf{A}_{41} = \mu_f \gamma((1+\delta)(1 - \left[\overline{S}\right]) - \frac{3}{2}\left[\Delta S\right])$$

$$\mathbf{A}_{44} = -K - \frac{M_l + M_h}{2} - \mu_f \gamma R((1+\delta)(1 - \left[\overline{S}\right]) - \frac{3}{2}\mu_f \gamma\left[\Delta T\right] + 3\mu_f \gamma R\left[\Delta S\right]$$

$$\mathbf{A}_{51} = \frac{\gamma}{2}\mu_f((1+\delta)(1 - \left[\overline{S}\right]) + \frac{\left[\Delta S\right]}{2})$$

$$\mathbf{A}_{54} = -\frac{M_l + M_h}{4} - \frac{\gamma}{2}\mu_f R(1+\delta)(1 - \left[\overline{S}\right]) - \frac{\gamma}{2}\mu_f R\left[\Delta S\right] + \frac{\gamma}{4}\mu_f\left[\Delta T\right]$$

For the HM,

$$\mathbf{A}_{11} = -1 - K - \frac{M_l + M_h}{2} + 3\mu_f \gamma\left[\Delta T\right] - \frac{3}{2}\mu_f \gamma R\left[\Delta S\right] + \mu_f([T_d] - \left[\overline{T}\right])$$

$$\mathbf{A}_{12} = \frac{M_l + M_h}{\gamma} - \mu_f([\Delta T] - R\,[\Delta S])$$

$$\mathbf{A}_{14} = -\mu_f R([T_d] - \left[\overline{T}\right]) - \frac{3}{2}\mu_f \gamma R\,[\Delta T]$$

$$\mathbf{A}_{21} = \frac{\gamma(M_h - M_l)}{4} - \frac{\gamma^2}{4}\mu_f R\,[\Delta S] + \frac{\gamma^2}{2}\mu_f\,[\Delta T] - \frac{\gamma}{2}\mu_f([T_d] - \left[\overline{T}\right])$$

$$\mathbf{A}_{22} = -1 - \frac{M_l + M_h}{2} + \frac{\gamma}{2}\mu_f([\Delta T] - R\,[\Delta S])$$

$$\mathbf{A}_{24} = -\frac{\gamma}{2}\mu_f R(-([T_d] - \left[\overline{T}\right]) + \frac{\gamma}{2}\,[\Delta T])$$

$$\mathbf{A}_{41} = \mu_f \gamma((1+\delta)(1 - \left[\overline{S}\right]) + \frac{3}{2}\,[\Delta S])$$

$$\mathbf{A}_{44} = -K - \frac{M_l + M_h}{2} - \mu_f \gamma R((1+\delta)(1 - \left[\overline{S}\right]) + \frac{3}{2}\mu_f \gamma\,[\Delta T] - 3\mu_f \gamma R\,[\Delta S]$$

$$\mathbf{A}_{51} = \frac{\gamma}{2}\mu_f(-(1+\delta)(1 - \left[\overline{S}\right]) + \frac{[\Delta S]}{2})$$

$$\mathbf{A}_{54} = -\frac{M_l + M_h}{4} + \frac{\gamma}{2}\mu_f R(1+\delta)(1 - \left[\overline{S}\right]) - \frac{\gamma}{2}\mu_f R\,[\Delta S] + \frac{\gamma}{4}\mu_f\,[\Delta T]$$

The elements of **A** can be calculated with the steady state [**y**] obtained numerically for fixed parameters. By solving the eigenvalues of the Jacobian matrix **A**, we can study the stability of the steady state: if the real part of the eigenvalues are all negative, the steady state is stable; if at least one eigenvalue has positive real part, the steady state is unstable, the small perturbation will grow exponentially. For example, with all other parameters fixed as in Figure 3-2, Figure A-1 shows the real parts of all eigenvalues of **A** at the strong steady TM (as shown in Figure 3-2) vs. the non-dimensional freshwater flux c on the semilog plot. They are all negative, and we know from the calculation that the imaginary parts of all eigenvalues are zero, so the strong steady TM is a stable node, the perturbation decays exponentially. Figure A-2 shows the real parts of all eigenvalues of **A** at the weak steady TM (as shown in Figure 3-2) vs. the non-dimensional freshwater flux c. There is one eigenvalue has positive real part, and the imaginary parts of all eigenvalues are zero, so the weak steady TM is a saddle, it is unstable to small perturbations. Figure A-3 shows the real parts of all eigenvalues of **A** at the steady HM (as shown in Figure 3-2) vs. the non-dimensional freshwater flux c on the semilog plot, all eigenvalues have negative real parts, and zero imaginary parts, so the steady HM which satisfies $\Delta\rho_{hd} < \varepsilon$ (such as that in region IV on the f-c bifurcation diagram) is a stable node.

Similarly, the real parts of all eigenvalues of **A** at the steady TM (as shown in Figure 3-3) vs. the non-dimensional background vertical diffusivity M are shown in Figure A-4 (strong steady TM, semilog plot), A-5 (weak steady TM), with all other parameters fixed as in Figure 3-3. Again we can see that the strong steady TM is a stable node; the weak steady TM is a saddle, thus unstable.

For the steady HM satisfying $\Delta\rho_{hd} \geq \varepsilon$, such as that in region III on the f-c (Figure 3-2) and f-M (Figure 3-3) bifurcation diagrams, no matter how small the perturbation is, the system can reach the condition for polar convection, thus the polar vertical diffusivity switches immediately from $M_h = M$ (no convection) to $M_h = M_{sw}$ (strong convection) and the dynamic equations for the perturbations change with it. However, since the steady HM [**y**] is solved with $M_h = M$, there will be a constant vector **B** on the RHS of the linearized dynamic equations of the perturbations, owing to the huge difference between M and M_{sw}, i.e.

$$\frac{d\mathbf{y}'}{dt'} = \mathbf{A}\mathbf{y}' + \mathbf{B}. \tag{A.6}$$

Here the elements of $\mathbf{A}$ is same as those calculated above for the steady HM satisfying $\Delta\rho_{hd} < \varepsilon$, $\mathbf{B}$ is the difference of the polar vertical diffusion term induced by the switch of M_h :

$$\mathbf{B} = \begin{pmatrix} -\frac{1}{\gamma}(M_{sw} - M)([T_d] - \left[\overline{T}\right] + \frac{\gamma[\Delta T]}{2}) \\ \frac{1}{2}(M_{sw} - M)([T_d] - \left[\overline{T}\right] + \frac{\gamma[\Delta T]}{2}) \\ -\frac{\delta}{2}(M_{sw} - M)([T_d] - \left[\overline{T}\right] + \frac{\gamma[\Delta T]}{2}) \\ -(M_{sw} - M)((1+\delta)(1 - \left[\overline{S}\right]) + \frac{[\Delta S]}{2}) \\ \frac{1}{2}(M_{sw} - M)((1+\delta)(1 - \left[\overline{S}\right]) + \frac{[\Delta S]}{2}) \end{pmatrix} \tag{A.7}$$

The solution for equation (A.6), $\mathbf{y}'$, will grow towards the vector $\mathbf{A}^{-1}\mathbf{B}$, so the steady HM satisfying $\Delta\rho_{hd} \geq \varepsilon$ is unstable to small perturbations, although all the eigenvalues of $\mathbf{A}$ at the steady HM satisfying $\Delta\rho_{hd} \geq \varepsilon$ give negative real parts (Figure A-3, A-6). The linearized equation (A.6) will breakdown when $\|\mathbf{y}'\|$ becomes large enough.

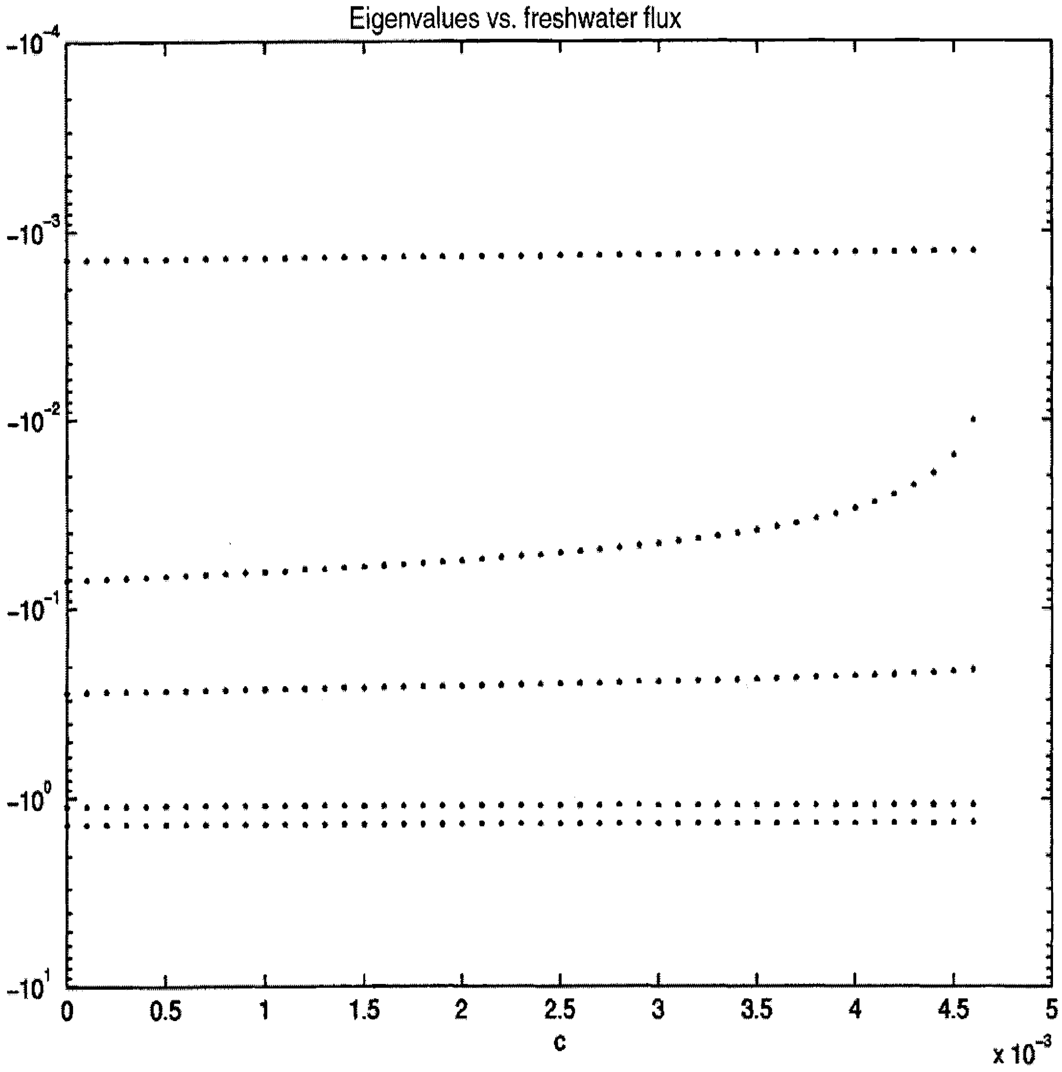

Figure A-1: Eigenvalues of the Jacobian matrix at the strong steady TM vs. freshwater flux.

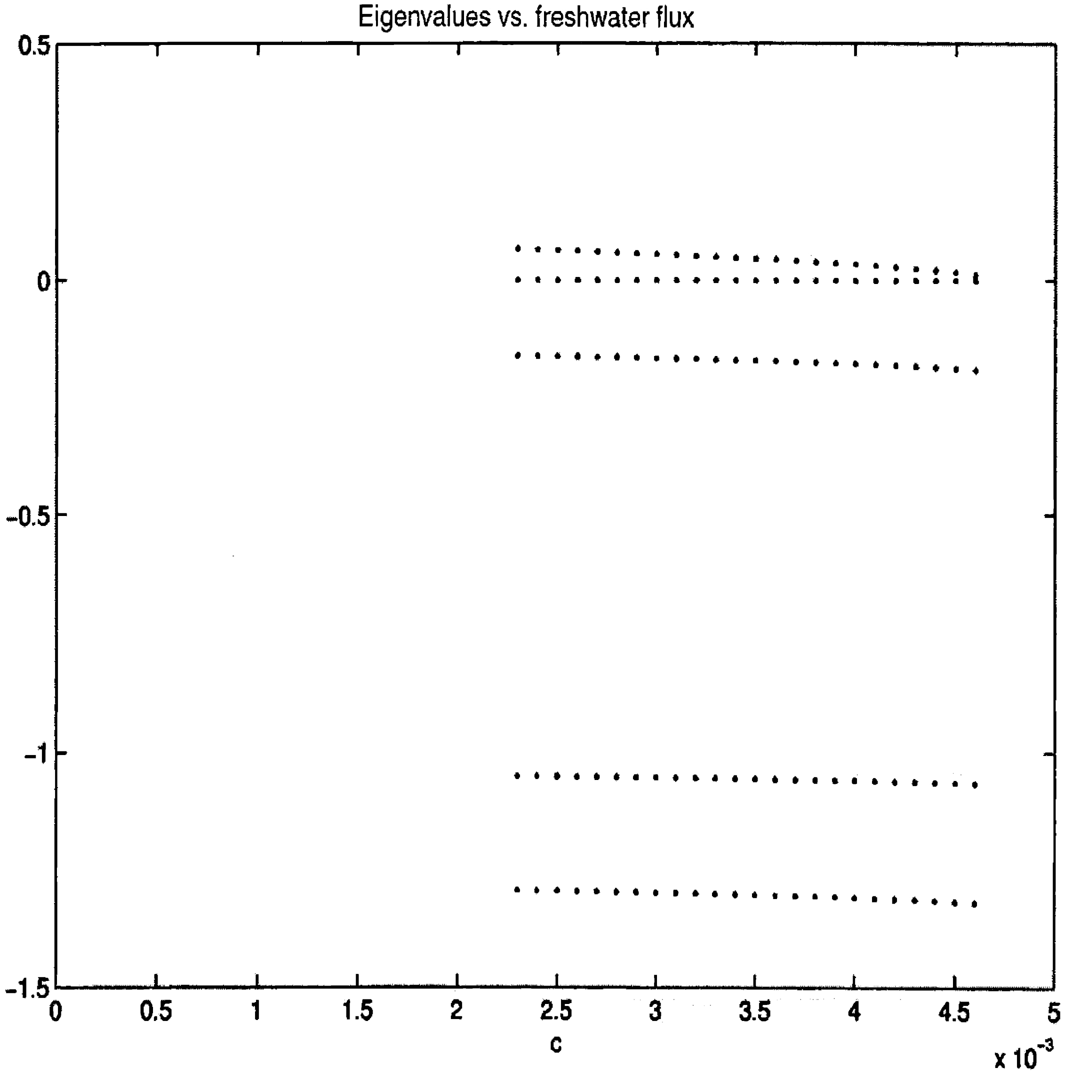

Figure A-2: Eigenvalues of the Jacobian matrix at the weak steady TM vs. freshwater flux.

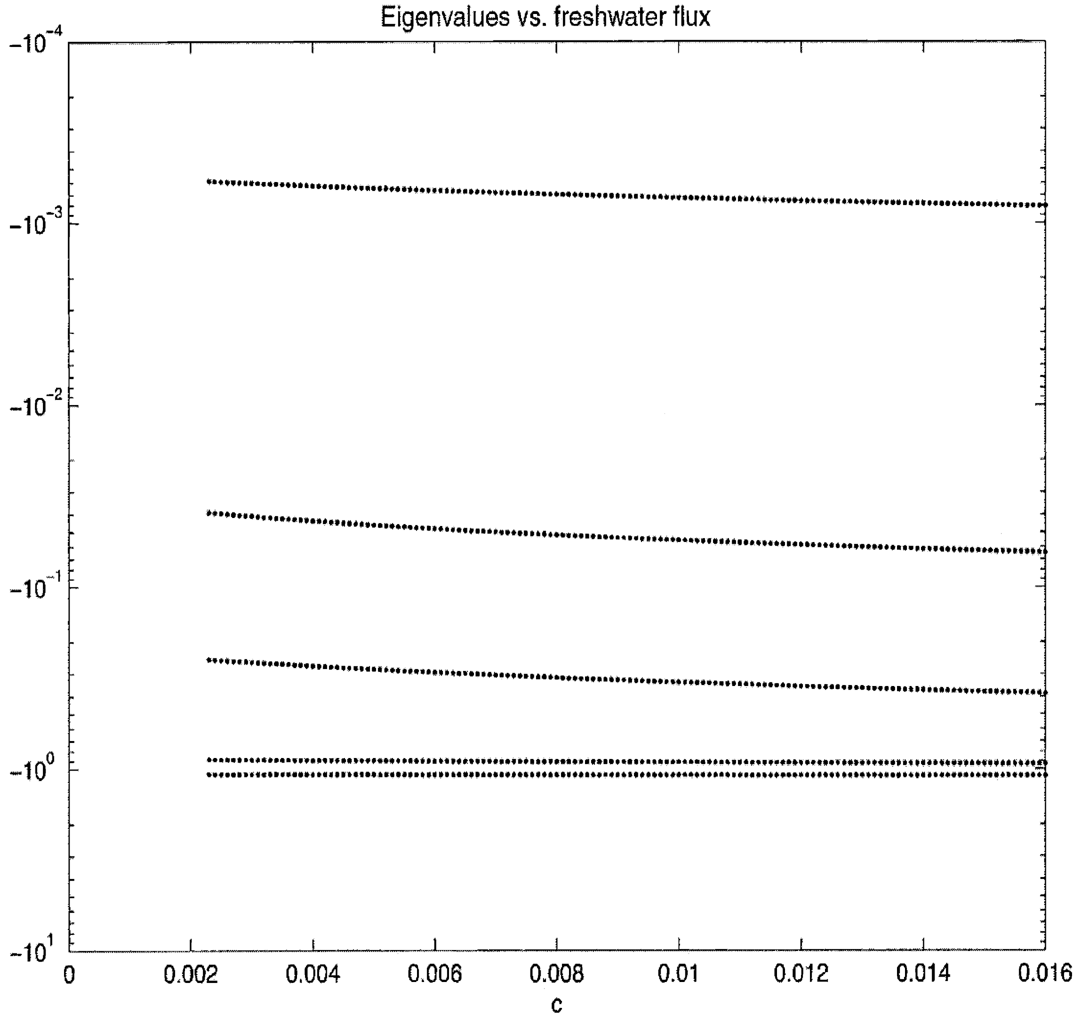

Figure A-3: Eigenvalues of the Jacobian matrix at the steady HM vs. freshwater flux.

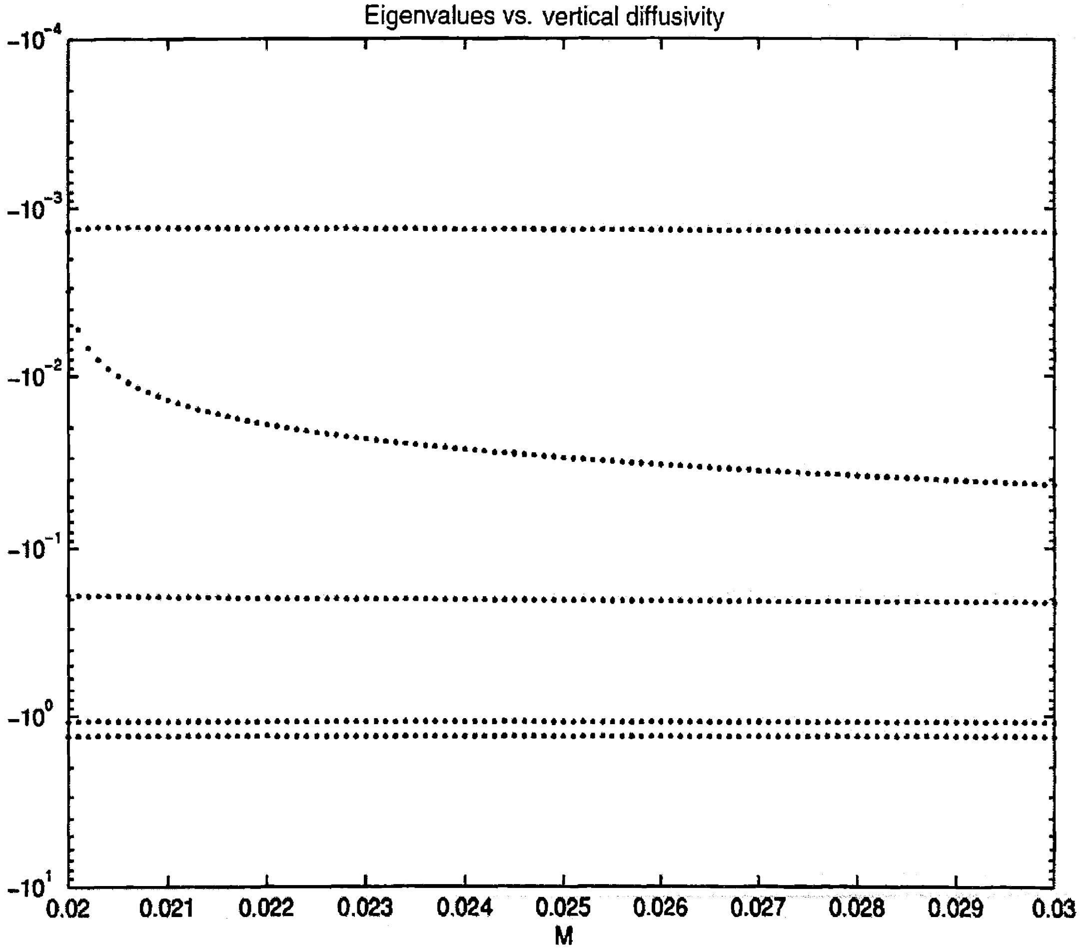

Figure A-4: Eigenvalues of the Jacobian matrix at the strong steady TM vs. background vertical diffusivity.

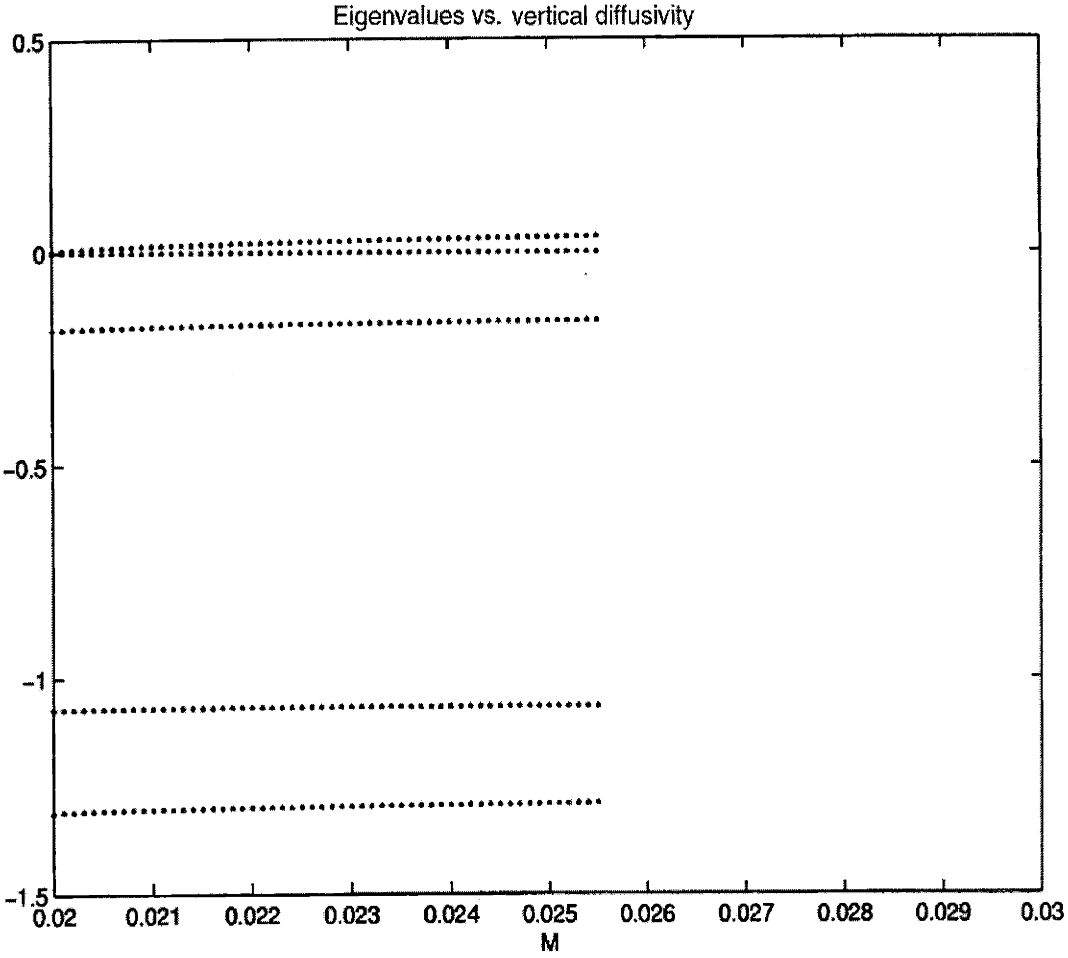

Figure A-5: Eigenvalues of the Jacobian matrix at the weak steady TM vs. background vertical diffusivity.

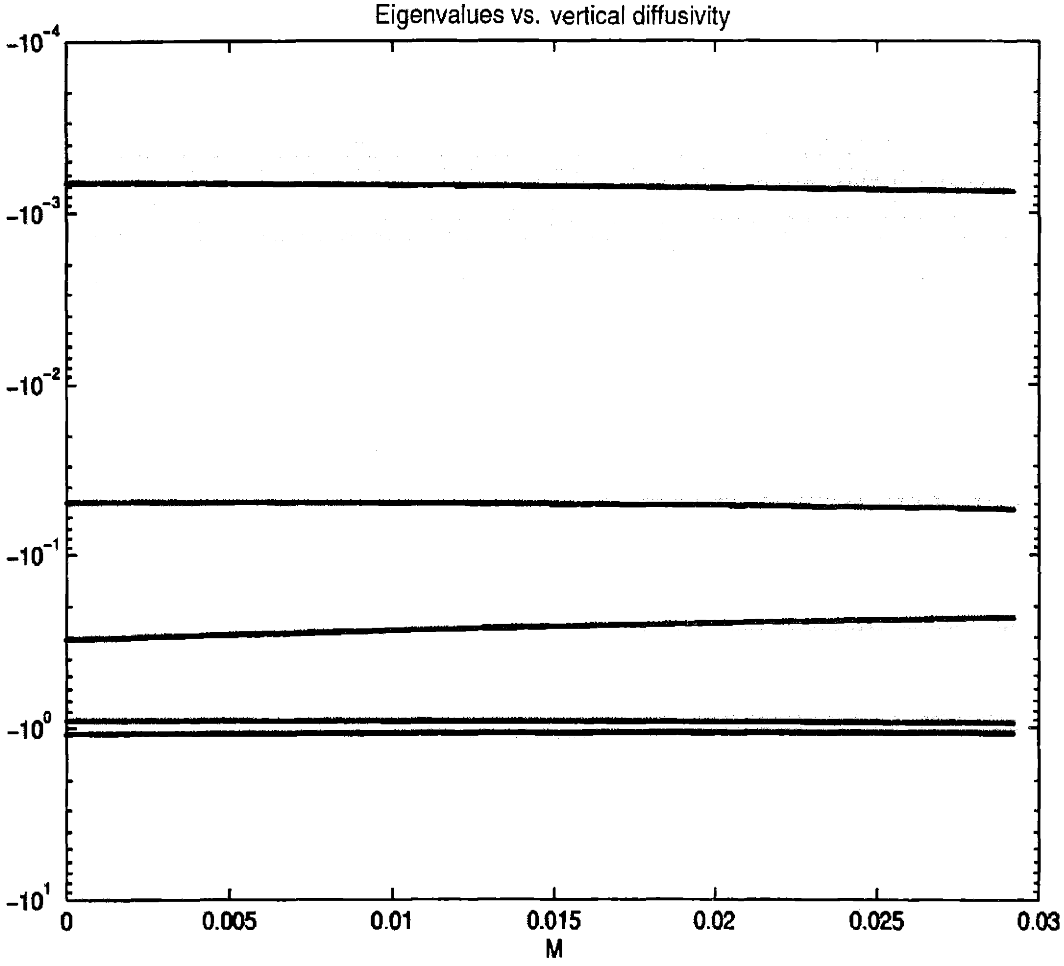

Figure A-6: Eigenvalues of the Jacobian matrix at the steady HM vs. background vertical diffusivity.

References

Anderson, L. A. and J. L. Sarmiento, Redfield ratios of remineralization determined by nutrient data analysis, *Global Biogeochem. Cycles*, **8**, 65-80, 1994.

Arthur, M. A., North Atlantic Cretaceous black shales: the record at Site 398 and a brief comparison with other occurrences, *Initial Reports of the Deep Sea Drilling Project*, **47**, 719-751, 1979.

Arthur, M. A. and S. O. Schlanger, Cretaceous "oceanic anoxic events" as causal factors in development of reef-reservoired giant oil fields, *The American Association of Petroleum Geologists Bullitin*, **63**, 870-885, 1979.

Arthur, M. A. and W. E. Dean, A holistic geochemical approach to cyclomania: Examples from Cretaceous pelagic limestone sequences, in *Cycles and Events in Stratigraphy*, edited by G. Einsele, W. Ricken, and A. Seilacher, Springer-Verlag, Berlin, pp. 133, 1991.

Berner, R. A. and D. E. Canfield, A new model for atmospheric oxygen over Phanerozoic time, *Am. J. Sci.,* **289**, 333-361 , 1989.

Bond, G. C. and R. Lotti, Iceberg discharges into the North Atlantic on millennial time scales during the last glaciation, *Science*, **267**, 1005-1010, 1995.

Bralower, T. J. and H. R. Thierstein, Low productivity and slow deep-water circulation in mid-Cretaceous oceans, *Geology*, **12**, 614-618, 1984.

Brass, G. W., J. R. Southam and W. H. Peterson, Warm saline bottom water in the ancient ocean, *Nature*, **296**, 620-623, 1982.

Broecker, W. S. and G. H. Denton, The role of ocean-atmosphere reorganizations in glacial cycles. *Geochimica Cosmochimica Acta,* **53**, 2465-2501, 1989.

Broecker, W. S. and T. H. Peng, *Tracers in the Sea*, Eldigio Press, Lamont-Dohery Geological Observatory, Palisades, N. Y., 1982.

Broecker, W. S. and T. H. Peng, *Greenhouse Puzzles*, Eldigio Press, Lamont-Dohery Geological Observatory, Palisades, N. Y., 1993.

Bryan, F., High-latitude salinity effects and interhemispheric thermohaline circulation, *Nature,* **323**, 301-304 , 1986.

Budyko, M. I., and A. B. Ronov, Atmospheric evolution in the Phanerozoic, *Geochem. Int.*, **16**, 1-9, 1979.

Dickson, A. G. and F. J. Millero, A comparison of the equilibrium constants for the dissociation of carbonic acid in seawater media. *Deep-Sea Res.*, **34**, 1733-1743, 1987.

Erwin, D. H., The Permo-Triassic extinction, *Nature,* **367**, 231-235 , 1994.

Follows, M., J., R. G. Williams, and J. Marshall, The solubility pump of carbon in the subtropical gyre of the North Atlantic. *JMR*, **54**, 605-630, 1996.

Gent, P. R. and J. C. McWilliams, Isopycnal mixing in ocean circulation models, *JPO,* **20**, 150-155 , 1990.

Haney, R. L., Surface thermal boundary condition for ocean circulation models. *JPO,* **1** , 241-248, 1971.

Herbert, T. D. and A. G. Fischer, Milankovitch climatic origin of Mid-Cretaceous black shale rhythms in central Italy, *Nature*, **321**, 739-743, 1986.

Huang, R. X., Luyten, J., and Stommel, H. M., Multiple equilibrium states in combined thermal and saline circulation. *JPO*, **22**, 231-246, 1992.

Huang, R. X., Thermohaline circulation: Energetics and variability in a single-hemisphere basin model, *J. Geophys. Res.,* **99**, 12471-12485, 1994.

Ishiwatari, A., Time-space distribution and petrologic diversity of Japanese ophiolites, in *Ophiolite Genesis and Evolution of the Oceanic Lithosphere,* edited by T. Peters, A. Nicolas, and R. G. Coleman, pp. 723-743, Kluwer Academic Publishers, Boston, 1991.

Isozaki, Y., Permo-Triassic Boundary Superanoxia and Stratified Superocean : Records from Lost Deep Sea, *Science,* **276**, 235-238, 1997.

Johnson, S. J., H. B. Clausen, W. Dansgaard, K. Fuhrer., N. Gundestrup, C. U. Hammer, P. Iverson, J. Jouzel, B. Stauffer, and J. P. Steffensen, Irregular glacial interstadials recorded in a new Greenland ice core, *Nature*, **359**, 311-313, 1992.

Kajiwara, Y., S. Yamakita, K. Ishida, H. Ishiga, and A. Imai, Development of a largely anoxic stratified ocean and its temporary massive mixing at the Permian / Triassic boundary supported by the sulfur isotopic record, *Palaeogeography, Palaeoclimatology, Palaeoecology,* **111**, 367-379, 1994.

Knoll, A. H., R. K. Bambach, D. E. Canfield, and J. P. Grotzinger, Comparative Earth History and Late Permian Mass Extinction, *Science,* **273**, 452-457, 1996.

Kozur, H. W., Some aspects of the Permian-Triassic boundary (PTB) and of the possible causes for the biotic crisis around this boundary. *Palaeogeography, Palaeoclimatology, Palaeoecology,* **143**, 227-272, 1998.

Kutzbach, J. E. and R. G. Gallimore, Pangaean climates: Megamonsoons of the megacontinent, *J. Geophys. Res.,* **94**, 3341-3358, 1989.

Kutzbach, J. E., P. J. Guetter, and W. M. Washington, Simulated circulation of an idealized ocean for Pangaean time, *Paleoceanography,* **5**, 299-317, 1990.

Ledwell, J. R., A. J. Watson, and C. S. Law, Evidence for slow mixing across the pycnocline from an open-ocean tracer-release experiment, *Nature,* **364**, 701-703, 1993.

Lohrenz, S. E., G. A. Knauer, V. L. Asper, M. Tuel, and A. H. Knap, Seanonal variability in primary production and particle flux in the northwestern Sargasso Sea: U.S. JGOFS Bermuda Atlantic Time-series Study, *Deep-Sea Res.,* **39**, 1373-1391, 1992.

Manabe, S and R. J. Stouffer, Two stable equilibria of a coupled ocean-atmosphere model, *Journal of Climate,* **1**, 841-866, 1988.

Manabe, S and R. J. Stouffer, Multiple-Century response of a coupled ocean-atmosphere model to an increase of atmospheric carbon dioxide. *Journal of Climate, 7,* 5-23, 1994.

Marotzke, J., Instabilities and multiple steady states of the thermohaline circulation, in *Oceanic Circulation Models: Combining Data and Dynamics,* edited by D. L. T. Anderson and J. Willebrand, Kluwer Academic Publishers, Boston, pp. 501-511, 1989.

Marotzke, J. and J. Willebrand, Multiple Equilibria of the Global Thermohaline Circulation, *JPO,* **21**, 1372-1385 , 1991.

Marotzke, J., Boundary mixing and the dynamics of three-dimensional thermohaline circulations. *JPO,* **27,** 1713-1728, 1997.

Marshall, J., C. Hill, L. Perelman, and A. Adcroft, Hydrostatic, quasi-hydrostatic, and nonhydrostatic ocean modeling, *J. Geophys. Res.,* **102**, 5733-5752, 1997a.

Marshall, J., A. Adcroft, C. Hill, L. Perelman, and C. Heisey, A finite-volume, incompressible Navier Stokes model for studies of the ocean on parallel computers, *J. Geophysical Res.,* **102**, 5753-5766, 1997b.

Marshall, J. and F. Schott, Open ocean deep convection: observations, models and theory, *Rev. of Geophysics,* **37**, 1-64, 1999.

Martin, J. H., G. A. Knauer, D. M. Karl, and W. W. Broenkow, VERTEX: Carbon cycling in the northeast Pacific, *Deep-Sea Res.,* **34**, 267-285, 1987.

Mook, W. G., ^{13}C in atmosphere CO_2, *Netherlands Journal of sea Research*, **20**, 211-223, 1986.

Munk, M. and C. Wunsch, Abyssal recipes II: energetics of tidal and wind mixing, *Deep-Sea Res.,* **45**, 1977-2010, 1998.

Najjar, R. G., J. L. Sarmiento, and J. R. Toggweiler, Downward transport and fate of organic matter in the ocean: simulations with a general circulation model, *Global Biogeochem. Cycles,* **6**, 45-76 , 1992.

North, G. R., R. F. Cahalan, and J. A. Coakley, Jr., Energy Balance Climate Models, *Reviews of Geophysics and Space Physics,* **19**, 91-121, 1981.

Paltridge, G. W. and C. M. R. Platt, *Radiative Processes in Meterology and Climatology*, Elsevier, Amsterdam, 1976.

Parsons, T. R., M. Takahashi, and B. Hargrave. *Biological oceanographic processes.* New York : Pergamon Press, 1988.

Pedersen T. F. and S. E. Calvert, Anoxia vs. productivity: what controls the formation of organic-carbin-rich sediments and sedimentary rocks? *The American Association of Petroleum Geologists Bulletin*, **74**, 454-466, 1990.

Pierce, D. W., Barnett, T. P., and Mikolajewicz, U., Competing roles of heat and freshwater flux in forcing thermohaline oscillations. *JPO*, **25**, 2046-2064, 1995.

Railsback, L. B., S. C. Ackerly, T. F. Anderson, and J. L. Cisne, Palaeontological and isotope evidence for warm saline deep waters in Ordovician oceans, *Nature,* **343**, 156-159, 1990.

Rooth, C., Hydrology and ocean circulation. *Progress in Oceanography*, **11**, Pergamon, 131-149, 1982.

Ruddick, B. and L. Q. Zhang, Qualitative behavior and nonoscillation of Stommel's thermohaline box model. *JOC*, **9**, 2768-2777, 1996.

Saleeby, J. B., Petrotectonic and paleogeographic settings of U.S. cordilleran ophiolites, in *The Cordilleran Orogen: Contemtinous U.S.,* edited by B. C. Burchfiel, P. W. Lipman, M. L. Zoback, pp. 653-682, Geological Society of America, The Geology of North America, G-3, Boulder, Colorado, 1992.

Sarmiento, J. L., T. D. Herbert, and J. R. Toggweiler, Causes of anoxia in the world ocean, *Global Biogeochemical cycles,* **2**, 115-128, 1988.

Stommel, H., Thermohaline convection with two stable regimes of flow, *Tellus,* **13**, 224-230, 1961.

Stumm, W. and J. J. Morgan, *Aquatic Chemistry.* Third Edition. John Wiley and Sons., N.Y., pp. 1022, 1996.

Takahashi, T., W.S. Broecker, and S. Langer, Redfield ratio based on chemical data from isopycnal surfaces. *Journal of Geophysical Research*, **90**, 6907-6924, 1985.

Takahashi, T., R. T. Williams, and D. L. Bos., Carbonate Chemistry; in GEOSECS Atlantic Expedition. Vol. 1. Hydrographic Data 1972-1973, National Science Foundation, Washington D.C., 1981.

Taylor, E. L., Taylor, T. N., and N. R. Cuneo, The present is not the key to the past : A polar forest from the Permian of Antarctica. *Science*, **257,** 1657-1677, 1992.

Toggweiler J. R. and J. L. Sarmiento, Glacial to interglacial changes in atmospheric carbon dioxide: The critical role of ocean surface water in high latitudes, in *The Carbon Cycle and Atmospheric* CO_2 *: Natural Variations, Archean to Present*, Geophysical Monography 32, American Geophysical Union, Washington, D.C., pp. 163-184, 1985.

Toole, J. M., K. L. Polzin, and R. Schmitt, Estimates of diapycnal mixing in the abyssal ocean, *Science,* **264**, 1120-1123 , 1994.

Wanninkhof, R., Relationship between wind speed and gas exchange over the ocean. *Journal of Geophysical Research,* **97**, 7373-7382, 1992.

Weaver, A. J. and E. S. Sarachik, The role of mixed boundary conditions in numerical models of the ocean's climate. *JPO*, **21**, 1470-1493, 1991a.

Weaver, A. J. and E. S. Sarachik, Evidence for decadal variability in an ocean general circulation model: An advective mechanism. *Atmos.-Ocean*, **29**, 197-231, 1991b.

Weaver, A. J., Marotzke, J., Cummins, P. F. and E. S. Sarachik, Stability and variability of the thermohaline circulation. *JPO*, **23**, 39-60, 1993.

Welander, P., A simple heat-salt oscillator. *Dyn. Atmos. Oceans*, **6**, 233-242, 1982.

Weiss, R. F., The solubility of nitrogen, oxygen and argon in water and seawater, *Deep-Sea Res.,* **17**, 721-735, 1970.

Weiss, R. F., Carbon dioxide in water and seawater: The solubility of a non-ideal gas. *Marine Chem.*, **2**, 203-215, 1974.

Wignall, P. B. and R. J. Twitchett, Oceanic Anoxia and the End Permian Mass Extinction, *Science,* **272**, 1155-1158, 1996.

Winton, M. and E. S. Sarachik, Thermohaline oscillations induced by strong steady salinity forcing of ocean general circulation models. *JPO*, **23**, 1389-1410, 1993.

Winton, M., Deep decoupling oscillations of the oceanic thermohaline circulation. *Ice in the Climate System*, NATO ASI Series, 112, W. R. Peltier, Ed., Springer Verlag, 417-432, 1993.

Wortmann U. G., Hesse, R., and Zacher, W., major-element analysis of cyclic black shales: Paleoceanographic implications for the Early Cretaceous deep western Tethys. *Paleoceanography*, **14**, 525-541, 1999.

Wright, D. G. and T. F. Stocker, A zonally averaged model for the thermohaline circulation. Part I: Model development and flow dynamics. *JPO*, **21**, 1713-1724, 1991.

Zhang, J. B., R. W. Schmitt, and R. X. Huang, The relative influence of diapycnal mixing and hydrologic forcing on the stability of the thermohaline circulation, *JPO,* **29**, 1096-1108 ,1999.

Zhang, J. Z. and F. J. Millero, The chemistry of the anoxic waters in the Cariaco trench, *Deep-Sea Res.,* **40**, 1023-1041, 1993.

Zhang, R, Follows, M. and Marshall J., Could the Late Permian Deep Ocean Have Been Anoxic? Accepted by *Paleoceanography*, 2001.